EQUILIBRIUM AND STABILITY OF MAGNETOHYDRODYNAMIC FLOWS IN ANNULAR CHANNELS

A Thesis Submitted to the
College of Graduate Studies and Research
in Partial Fulfillment of the Requirements
for the degree of Doctor of Philosophy
in the Department of Physics and Engineering Physics
University of Saskatchewan
Saskatoon

By
Ivan V. Khalzov

Permission to Use

In presenting this thesis in partial fulfilment of the requirements for a Postgraduate degree from the University of Saskatchewan, I agree that the Libraries of this University may make it freely available for inspection. I further agree that permission for copying of this thesis in any manner, in whole or in part, for scholarly purposes may be granted by the professor or professors who supervised my thesis work or, in their absence, by the Head of the Department or the Dean of the College in which my thesis work was done. It is understood that any copying or publication or use of this thesis or parts thereof for financial gain shall not be allowed without my written permission. It is also understood that due recognition shall be given to me and to the University of Saskatchewan in any scholarly use which may be made of any material in my thesis.

Requests for permission to copy or to make other use of material in this thesis in whole or part should be addressed to:

Head of the Department of Physics and Engineering Physics
163 Physics Building
116 Science Place
University of Saskatchewan
Saskatoon, Saskatchewan
Canada
S7N 5E2

Abstract

Magnetohydrodynamic (MHD) flows in annular channels are of great current interest due to experimental search for the so-called magnetorotational instability (MRI) which is important for astrophysical applications (accretion disk physics, magnetic dynamo effect). The main point of MRI experiments is to study the stability of liquid metal rotating in an external magnetic field. Two different types of fluid rotation are proposed: Taylor-Couette flow between rotating coaxial cylinders and electrically driven flow in transverse magnetic field. The implementation of MRI experiments and explanation of experimental results requires a theoretical study of the equilibrium and the stability of MHD flow in an annular channel. This is one of the main tasks of present thesis.

For study of equilibrium Taylor-Couette and electrically driven flows, a numerical code is developed which is based on the finite difference scheme with Jacobi iterations. The structure of flows is calculated for different parameters of the experiment. Effect of the inertia on the rotation profiles is investigated in detail. The approximate analytical expressions are obtained for radial profiles of rotation that can be used for optimization of the experimental device for MRI investigation. Equilibrium Taylor-Couette and electrically driven flows are compared from the perspective of experimental studies of MRI.

The spectral stability of electrically driven flow is studied by solving the eigenvalue problem. This study is performed in the frames of both ideal and dissipative MHD models. It is shown that electrically driven flow can be destabilized through the mechanism of MRI if fluid velocity exceeds some instability threshold, which is determined by non-axisymmetric modes (azimuthal number $m \neq 0$). The obtained results are compared with available experimental data.

A general variational method is developed for the stability study of MHD flows of ideal compressible fluids. It is shown that the linearized dynamics of such fluids

has an infinite set of invariants. A necessary and sufficient stability criterion can be obtained after inclusion of one or several such invariants in analysis. An analytical example is presented to confirm the fruitfulness of the developed method.

Acknowledgements

I would like to thank my supervisor Dr. Andrei Smolyakov for his continual guidance and encouragement during my PhD project. At many stages in the course of this research project I benefited from his advice and help; his ideas contributed greatly to the material of the present thesis.

I am sincerely thankful to Dr. Victor Ilgisonis and Dr. Vladimir Lakhin from the Russian Research Center "Kurchatov Institute" for their interest in my work, numerous helpful discussions and support during my visits to Moscow. Also I am grateful to Dr. Evgenii Velikhov, the president of the RRC "Kurchatov Institute", who had initiated the experimental program on magnetorotational instability and posed several theoretical issues addressed in present thesis.

I wish to express my special thanks to Dr. Leonid Benkevich for introducing me into the basics of MATLAB and to Koloman Varady for the help in preparation of the thesis.

I deeply appreciate the warm and friendly atmosphere created by my friends and colleagues: Tatyana Chshyolkova, Elena Krestova, Tatyana Novoselova, Sergei Ivanov, Dmytro and Yulia Sydorenko, and Mykola Dreval.

I would like to acknowledge also the financial support provided by NSERC Discovery Grant (A. Smolyakov), University of Saskatchewan Graduate Scholarships, Herzberg Memorial Scholarship and Rowles Fellowship.

Contents

List of Tables

List of Figures

List of Abbreviations and Terms

MHD	Magnetohydrodynamics
MRI	Magnetorotational instability
$\mathbf{B}$	Magnetic field
$\mathbf{b}$	Non-dimensional magnetic field
B	Characteristic value of magnetic field
$\mathbf{B}_0 = B_0\mathbf{e}_z$	External uniform magnetic field
c	Speed of light in vacuum
cr	Subscript and superscript denoting a marginally stable value of a quantity
c_s	Speed of sound
d	Differential; thickness of boundary layer
$\mathbf{E}$	Electric field
E	Total energy
e	Subscript denoting an equilibrium quantity
$\mathbf{e}_r$, $\mathbf{e}_\varphi$, $\mathbf{e}_z$	Unit vectors of the cylindrical coordinate system
$\mathbf{h} = \mathrm{Ha}/\mathrm{Re}_m(\delta\mathbf{B}/B)$	Normalized perturbation of magnetic field
H	Height of the channel
h	Non-dimensional height of the channel
$h(r,z)$	Normalized poloidal current stream function
$\mathrm{Ha} = LB/\sqrt{4\pi\rho\nu\eta}$	Hartmann number
i	Imaginary unit
I_0	Total electric current flowing through the channel
Im	Imaginary part of a complex number
$\mathbf{J}$	Electric current density
$\mathbf{k} = k_r\mathbf{e}_r + k_\varphi\mathbf{e}_\varphi + k_z\mathbf{e}_z$	Non-dimensional wave-vector
$K_r = \pi(n_r+1)/(R_2-R_1)$	Radial wave-number
$K_z = \pi n_z/H$	Axial wave-number
L	Characteristic value of length
M_0	Characteristic value of angular momentum
m	Azimuthal mode-number
N	Number of grid points in numerical scheme
n_r	Radial mode-number
n_z	Axial mode-number
P	Pressure
p	Non-dimensional total pressure
$\mathrm{Pr}_m = \nu/\eta$	Magnetic Prandtl (or Batchelor) number
$\mathbf{R}$	Radius-vector
$\mathbf{r}$	Non-dimensional radius-vector
R	Radial coordinate in the cylindrical coordinate system
r	Non-dimensional radial coordinate in the cylindrical coordinate system

$R_{1,2}$	Inner and outer radii of the channel
$r_{1,2}$	Non-dimensional inner and outer radii of the channel
Re	Real part of a complex number
$\mathrm{Re} = LV/\nu$	Reynolds number
$\mathrm{Re}_m = LV/\eta$	Magnetic Reynolds number
s	Grid spacing in numerical scheme
t	Time
$\mathbf{u} = \delta V/V$	Non-dimensional perturbation of velocity
U	Lyapunov function(al) candidate
$u(r, z)$	Non-dimensional angular momentum
$u_0(r)$	Radial profile of non-dimensional angular momentum
$\mathbf{V}$	Velocity
$\mathbf{v}$	Non-dimensional velocity
V	Characteristic value of velocity
$V_A = B/\sqrt{4\pi\rho}$	Alfven velocity
W	Potential energy
$w(r, z)$	Non-dimensional poloidal velocity stream function
Z	Axial coordinate in the cylindrical coordinate system
z	Non-dimensional axial coordinate in the cylindrical coordinate system
Γ	Boundary
γ	Adiabatic index; increment of instability
δ	Variation; non-dimensional thickness of boundary layer
η	Electric resistivity
κ	Epicyclic frequency
λ_k	Lagrange multipliers
ν	Kinematic viscosity
$\boldsymbol{\xi}$	Infinitesimal variation; Lagrangian displacement vector
$\Pi = P/\rho + \mathbf{B}^2/8\pi\rho$	Normalized total pressure
ρ	Mass density
σ	Electric conductivity
τ	Non-dimensional time; time step in numerical scheme
φ	Azimuthal coordinate in the cylindrical system of coordinates
$\boldsymbol{\omega} = \nabla \times \mathbf{u}$	Non-dimensional perturbation of vortex
$\Omega(R)$	Angular velocity
ω	Eigen-frequency
$\bar{\omega} = \omega - m\Omega(R)$	Shifted eigen-frequency
$\Omega_{1,2}$	Angular velocity at the inner and outer radii of the channel
$\omega_A = K_z V_A$	Alfven frequency

Chapter 1

Introduction

1.1 Importance of the problem

1.1.1 Magnetohydrodynamic flows in applied and fundamental studies

Study of magnetohydrodynamic flows – flows of conducting fluids (liquid metals, electrolytes, plasmas, etc.) in the presence of magnetic field – is an important part of modern fluid mechanics. These studies were initiated in 1937 by pioneer works of Hartmann and Lazarus [1,2], who performed theoretical and experimental analysis of a laminar flow of mercury in ducts placed in the magnetic field. The subject was further developed by Alfven [3,4], who established the basics of magnetohydrodynamics (MHD) – a new academic discipline incorporating the classical hydrodynamics and electromagnetism. The principles of MHD are described in details in many textbooks of general content, such as [5–7].

MHD flows play a considerable role in many applied and fundamental studies. First of all, MHD flows of fluids in channels are the basis for different industrial technologies. Examples include electromagnetic flow-measurements of conducting fluids [8, 9], electromagnetic pumps used in metallurgy and systems of liquid-metal cooling for nuclear reactors [10], MHD power generators – the devices for direct conversion of thermal energy to electricity [11, 12], and MHD propulsions for propelling seagoing vessels [13].

Due to their importance in engineering applications, MHD flows in channels have been intensively studied theoretically [7,14,15]. The most studied case is represented

by a straight channel of a rectangular cross-section because it forms the basis for majority of MHD technologies. The MHD flows in annular channels are less studied, however they have attracted a lot of attention lately because of experiments on magnetorotational instability (see below). The theoretical analysis of stationary structure and stability of such flows is presented in the thesis.

MHD flows are common phenomena in modern experimental devices for confinement of fusion plasma, such as tokamaks. The plasma flows in tokamaks are developed in the regimes with additional heating, for example, as a result of unbalanced neutral beam injections [16, 17] or ion cyclotron resonance frequency heating [18, 19]. The effect of flows on stability properties of plasma configuration is not completely understood. Numerous experimental observations show that the plasma flows in tokamaks can improve the overall plasma confinement by stabilizing kink and resistive wall modes and suppressing turbulence [20–22].

Stability analysis of MHD configurations with flows constitutes a very challenging mathematical problem. The linear stability analysis of such systems was first carried out in the classic paper of Frieman and Rotenberg [23]. They showed that, unlike the static case, the linear operator of flow dynamics becomes non-Hermitian (non-self-adjoint) and it is not possible anymore to use the well-developed theory of Hermitian linear operators. In addition, eigen-frequencies of normal mode perturbations in a flow may assume, generally, complex values. As a result, the eigen-value stability analysis of MHD systems with flows is methodically difficult and is often restricted to simple geometries.

Contrary to the static case, where the well-known energy principle is used to establish the sufficient and necessary condition for non-linear stability [24], in the case with flow, the energy principle gives only the sufficient condition, which is normally too strong and almost never can be satisfied [25]. Different attempts were made to find a variational approach which generalizes the energy principle for the systems with MHD flows (see review [26]), however, this problem is still far from a complete solution. Such approach based on inclusion of new integrals of motion in linear stability analysis is proposed in present thesis.

1.1.2 The problem of accretion and magnetorotational instability

A number of astrophysical phenomena are associated with MHD flows. One of them is the accretion disk – a differentially rotating gas-dust disk formed around a gravitational center as a result of the gradual fall (accretion) of matter into the center. Accretion disks are ubiquitous objects in the universe, appearing at different scales; they can be formed around protostars (protostellar disks), in double star systems (one of which is usually a massive black hole), and also in active galactic nuclei [27].

For matter to fall into the central object, conservation of angular momentum requires a mechanism that transfers the matter's angular momentum outwards. On one hand, it is clear that viscous stresses are the mechanism which can cause matter to redistribute the angular momentum in the disk and eventually to accrete. On the other hand, the classical (collisional) viscosity itself is not sufficiently large to provide the observed rates of accretion. In order to explain the enhanced angular momentum transport, turbulent viscosity has to be taken into account. The conventional phenomenological model of accretion disk, the so-called α-model, was developed by Shakura and Sunaev in 1973 [28]. Assuming strong turbulence in the thin disk, they gave the following estimate for turbulent viscosity:

$$\nu_t = \alpha c_s H,$$

where c_s is the sound speed, H is the disk height, and α is an adjustable parameter between zero (no accretion) and one.

The α-model satisfactorily explained the observed rates of accretion, however the question about the origin of the disk turbulence remained unanswered. According to the hydrodynamic Rayleigh stability criterion [29], a rotation with the radial profile of angular velocity $\Omega(R)$ is linearly stable, if

$$\frac{\partial(\Omega^2 R^4)}{\partial R} > 0. \tag{1.1}$$

This means that the disk with the Keplerian rotation profile[1]

$$\Omega(R) = \sqrt{\frac{GM}{R^3}}, \tag{1.2}$$

where G is gravitational constant and M is mass of the central object, is stable with respect to infinitesimal perturbations. So, the development of turbulence required for α-model can be caused either by nonlinear hydrodynamic instabilities or by processes of non-hydrodynamic nature.

Nonlinear hydrodynamic instabilities often occur in linearly stable flows at sufficiently large Reynolds numbers (the definition of Reynolds number is given in Section 1.3.2); the most famous example here is Poiseuille pipe flow. Accretion disks are known to have extremely high Reynolds numbers (up to $\mathrm{Re} \sim 10^{12}$). However, the question of whether they can be nonlinear unstable and thereby turbulent is controversial [30]. The numerical simulations of accretion disks [31, 32] demonstrate that they are nonlinearly stable in hydrodynamics. This is also supported by recent laboratory experiments with quasi-Keplerian flows [33].

The effective mechanism for the development of turbulence in an accretion disk was proposed in 1991 by Balbus and Hawley [34]. They showed that the presence of a magnetic field results in the robust linear MHD instability of the accretion disk, which, in turn, excites and supports the turbulence. It should be noted that this instability, known as magnetorotational instability (MRI), was originally predicted by Velikhov in 1959 [35] and then verified by Chandrasekhar [36]. According to this theory, the rotation of a conducting fluid in a transverse magnetic field is stable if the angular velocity of rotation increases with radius as

$$\frac{\partial \Omega^2}{\partial R} > 0, \tag{1.3}$$

otherwise it can be destabilized through the mechanism of MRI. The astrophysical disks with Keplerian flow (1.2) do not meet the condition (1.3) and, therefore, they are prone to magnetorotational instability. The magnetic fields present in astrophys-

[1]The disk is assumed to be non-self-gravitating, so its rotation profile is determined only by mass of the central object.

ical objects (required for the instability to occur) are believed to be generated via dynamo action [37].

1.1.3 MRI experiments

Since 1991, MRI has been widely accepted as a source of turbulence and enhanced transport of orbital angular momentum in accretion disks; different aspects of MRI have been addressed and intensively studied (see comprehensive reviews [38], [39] and references therein). The results of numerical simulations of nonlinear stage of MRI in accretion disks have been reported in numerous papers [40–43]. The potential importance of MRI for astrophysics naturally led to efforts to simulate this instability in a laboratory experiment. Despite numerous attempts, MRI has not been clearly detected in laboratory, thus, any progress in this direction would be a great success.

A number of MRI experiments have been proposed over recent years [44–49]. Primary goals of these experiments are to detect MRI in a conducting fluid (usually a liquid metal) rotating in an external magnetic field, to investigate the stage of nonlinear saturation of MRI (probably turbulent) and to study the possibility of enhanced angular momentum transport in such a system. Another stated goal of MRI experiments is to validate astrophysical MHD codes in a laboratory setting.

Two different mechanisms of fluid rotation have been proposed for MRI experiments so far: mechanical drive by virtue of the viscous drag force acting on the fluid between moving surfaces (a so-called Couette flow) and electrical drive by the Ampere force arising when the electric current is passed through the fluid in a transverse magnetic field (electrically driven flow). In most existing MRI experiments a Couette flow is used either in spherical [44] or cylindrical geometry [45–47]. The first observation of MRI in spherical configuration was reported at the University of Maryland in 2004 [44]. In this experiment a liquid sodium flow between differentially rotating spheres, with an imposed coaxial magnetic field, was used. However, the background flow of liquid sodium was already fully turbulent without any magnetic field, indicating that MRI (if there is one!) is not the only possible instability in such a configuration. Besides, the spherical geometry of this experiment reproduces

the conditions of star or planet dynamo rather than the processes in accretion disk.

The more adequate model of an accretion disk in experiment is the Couette flow of liquid metal between rotating coaxial cylinders (this flow is also called Taylor-Couette flow) placed in an external magnetic field (Fig. 1.1). In the ideal case of infinitely long cylinders, the Taylor-Couette flow has the following radial profile of angular velocity:

$$\Omega(R) = a + b/R^2, \tag{1.4}$$

where the constants a and b are expressed through the angular velocities of cylinders and their radii. The stability analysis of the rotation profile (1.4) was performed in numerous papers [45, 50–57]. Several MRI experiments were designed: the liquid sodium $\alpha\omega$ dynamo experiment at the New Mexico Institute of Mining and Technology (USA) [45], the liquid gallium MRI experiment at Princeton Plasma Physics Laboratory (USA) [46] and the Potsdam-Rossendorf Magnetic Instability Experiment ("PROMISE", Germany) [47]. Despite the relative simplicity of these experiments, most of them have not been realized completely and MRI had not been achieved. The main difficulty here is that the cylinders in real experiment are bounded by the stationary end-caps which affect the entire equilibrium flow, making its radial profile significantly different from the ideal one (1.4), so the conditions for MRI may not be met. Their influence can be reduced either by employing differentially rotating end-caps [46] or by using sufficiently long cylinders. In the latter case, experimental observation of MRI have been reported [47], however, the authors of [58] showed that the cause of this instability is viscous boundary layers, rather than globally unstable magnetorotational modes.

Another way to rotate conducting fluid is to apply a radial electric field in an annular channel placed in an external axial magnetic field. This idea in relation to MRI experiments was first proposed in Los Alamos [48], with the conducting fluid being a low-temperature plasma. A similar setup using the electrically driven flow of liquid sodium instead of plasma, has been developed in the Russian Research Center "Kurchatov Institute" [49] and built in Obninsk (Russia) (Fig. 1.2). In the case of electrical drive the flow forms so-called Hartmann layers near the top and bottom

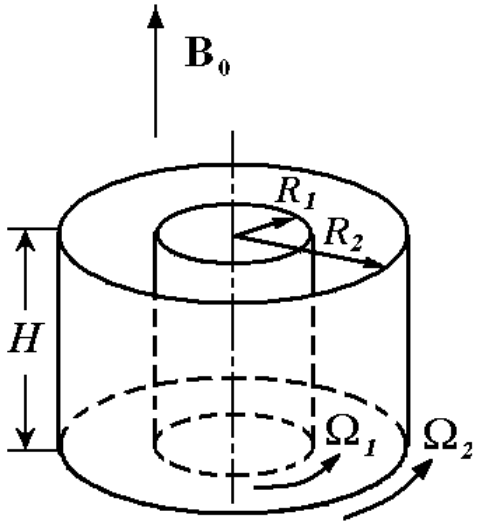

Figure 1.1: Sketch of magnetized Taylor-Couette flow.

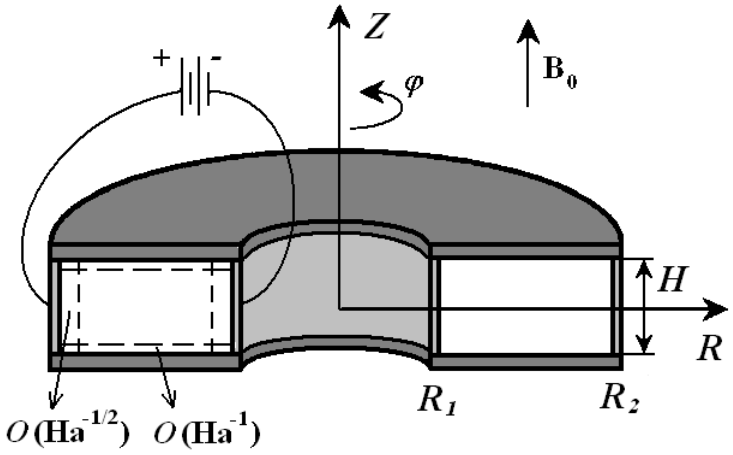

Figure 1.2: Sketch of electrically driven flow.

walls and parallel boundary layers near the side walls of the channel. The widths of these layers scale with the non-dimensional Hartmann number Ha (which is proportional to the magnetic field, see the definition (1.24)) as $O(\mathrm{Ha}^{-1})$ and $O(\mathrm{Ha}^{-1/2})$ respectively, so they become negligible at high values of magnetic field when $\mathrm{Ha} \gg 1$ and do not influence the bulk of the flow [59]. The stationary rotation profile of the flow in this case is

$$\Omega(R) = \frac{C}{R^2} \tag{1.5}$$

almost entirely in the cross section of the channel, where the constant C is determined by the physical properties of the fluid and the total electric current passed through the channel. The rotation profile (1.5) is marginally stable in hydrodynamics according to Rayleigh's criterion (1.1) but it can become unstable in the presence of a magnetic field since the condition (1.3) is not satisfied. For the implementation of an MRI experiment with electrically driven flow and the explanation of its results, it is crucial to perform the detailed theoretical study of the stationary flow in annular channel and the analysis of its stability, in particular, with respect to MRI. The material of the present work is mainly devoted to this goal.

1.2 Goals of the study

The main goal of the present research is the theoretical study of the electrically driven MHD flow of a liquid metal in an annular channel in the configuration related to MRI experiments. This study includes:

- detailed analysis of stationary MHD flow in the channel for different values of applied magnetic field and electric current;
- spectral stability study of the stationary flow in the frame of ideal MHD, investigation of unstable eigen-modes, their increments and dependence of increments on the parameters of the device;
- spectral stability study of stationary flow in the frame of dissipative MHD, finding of the stability threshold for eigen-modes with different azimuthal mode-

numbers.

Another goal of the research is the development of a variational procedure for the study of linear stability of ideal MHD flows, which generalizes the energy principle and allows one to obtain a necessary and sufficient condition for the stability of these flows.

1.3 Theoretical models

The results of the present thesis are obtained in the frame of one-fluid magnetohydrodynamic models. In this section we describe their basic concepts. As mentioned above, MHD studies the coupled dynamics of electrically conducting fluids and magnetic field. MHD is a fluid theory, i.e. it does not take into account the motion of the constituent particles of the substance but describes the system macroscopically by virtue of mean parameters (such as density, mass velocity, pressure, etc.). The fluid description is valid when collective interaction (such as collisions) of particles can isotropize the particles' velocity distribution in some local reference frame, thereby making it close to a Maxwellian one [60]. As a result, MHD models (and fluid theories in general) are often reasonably accurate.

Based on the character of the fluid flows, all MHD models are classified as *compressible* or *incompressible*. The effects of compressibility can be neglected if the characteristic fluid velocity is much less than its speed of sound, i.e. $V \ll c_s$. Incompressibility does not necessarily mean constant density; however, in the following discussion by incompressible fluid we will imply a fluid with constant density ρ. Compressible MHD models are normally used for a description of gaseous conducting substances such as plasmas, although they are suitable for all fluids. Incompressible MHD models properly describe the flow of fluids such as liquid metals and electrolytes.

Another classification of MHD models is based on the dissipative properties of the fluid. If the dissipative effects (viscosity and resistivity) are taken into account then the MHD model is referred to as *dissipative*, otherwise it is *ideal*.

1.3.1 Compressible one-fluid MHD

Compressible one-fluid MHD describes the principal effects of fluid macroscopic dynamics in terms of mean density $\rho(t, \mathbf{R})$, mass velocity $\mathbf{V}(t, \mathbf{R})$, pressure $P(t, \mathbf{R})$ and magnetic field $\mathbf{B}(t, \mathbf{R})$ (see, for example, [5]):

$$\frac{\partial \rho}{\partial t} + \nabla \cdot (\rho \mathbf{V}) = 0, \tag{1.6}$$

$$\rho \frac{\partial \mathbf{V}}{\partial t} + \rho(\mathbf{V} \cdot \nabla)\mathbf{V} = -\nabla P + \frac{1}{4\pi} (\nabla \times \mathbf{B}) \times \mathbf{B} + \rho \nu \nabla^2 \mathbf{V}, \tag{1.7}$$

$$\nabla \cdot \mathbf{B} = 0, \tag{1.8}$$

$$\frac{\partial \mathbf{B}}{\partial t} = \nabla \times (\mathbf{V} \times \mathbf{B}) + \eta \nabla^2 \mathbf{B}. \tag{1.9}$$

Here t is time, $\mathbf{R}$ is radius-vector, ν is the kinematic viscosity and η is the electrical resistivity of the fluid (properly speaking, the magnetic diffusivity). The system (1.6)-(1.9) should be supplemented by the dynamics of the fluid pressure, which is determined by an equation of state and a thermodynamic process. In particular, in an adiabatic process, the pressure of an ideal gas evolves according to the equation

$$\frac{\partial P}{\partial t} + \mathbf{V} \cdot \nabla P + \gamma P \nabla \cdot \mathbf{V} = 0, \tag{1.10}$$

where γ is the adiabatic index of the gas.

The physical meaning of the system (1.6)-(1.10) is quite obvious. Equation (1.6) is the usual hydrodynamic continuity equation; equation (1.7) is the Navier-Stokes equation, including the Ampere force due to the electric current density $\mathbf{J}$ which is expressed from Maxwell's equation

$$\nabla \times \mathbf{B} = \frac{4\pi}{c} \mathbf{J}, \tag{1.11}$$

where c is speed of light and the displacement current is neglected[2]. Equation (1.8) is the divergence-free condition for the magnetic field. Equation (1.9) is Maxwell's equation for the curl of the electric field $\mathbf{E}$ (Faraday's law of induction):

$$\nabla \times \mathbf{E} = -\frac{1}{c} \frac{\partial \mathbf{B}}{\partial t}, \tag{1.12}$$

[2]This is valid when the typical fluid velocity is much less than the speed of light, $V \ll c$.

in which the electric field is expressed from Ohm's law in moving media:

$$\mathbf{J} = \sigma\left(\mathbf{E} + \frac{1}{c}(\mathbf{V} \times \mathbf{B})\right). \tag{1.13}$$

Here σ is electric conductivity of the fluid; it is related to resistivity η:

$$\eta = \frac{c^2}{4\pi\sigma}. \tag{1.14}$$

The system of equations (1.6)-(1.10) constitutes *dissipative compressible* one-fluid MHD. This general form of one-fluid MHD can be further simplified depending on the particular problem at hand.

1.3.2 Incompressible one-fluid MHD

For the analysis of flows of liquid metals in channels, incompressible MHD models are normally used. In this case, the system (1.6)-(1.10) is reduced to *dissipative incompressible* MHD:

$$\nabla \cdot \mathbf{V} = 0, \tag{1.15}$$

$$\frac{\partial \mathbf{V}}{\partial t} + (\mathbf{V} \cdot \nabla)\mathbf{V} = -\nabla\Pi + \frac{1}{4\pi\rho}(\mathbf{B} \cdot \nabla)\mathbf{B} + \nu\nabla^2\mathbf{V}, \tag{1.16}$$

$$\nabla \cdot \mathbf{B} = 0, \tag{1.17}$$

$$\frac{\partial \mathbf{B}}{\partial t} = \nabla \times (\mathbf{V} \times \mathbf{B}) + \eta\nabla^2\mathbf{B}, \tag{1.18}$$

where we have introduced the normalized total pressure:

$$\Pi = \frac{P}{\rho} + \frac{\mathbf{B}^2}{8\pi\rho},$$

and used the vector identity:

$$(\nabla \times \mathbf{B}) \times \mathbf{B} = -\nabla\frac{\mathbf{B}^2}{2} + (\mathbf{B} \cdot \nabla)\mathbf{B}.$$

It should be noted here that the dynamics of the normalized total pressure Π is not specified by any additional equations (like (1.10)); at each instant it can be determined from the spatial distribution of fluid velocity and the magnetic field. Besides, we will assume that the viscosity ν and resistivity η of the fluid are constant, although in real systems they can change in space and time.

It is easy to show that the solution to the system (1.15)-(1.18) depends on three scaling parameters. If the characteristic values of length L, fluid velocity V and magnetic field B are known then the physical quantities can be normalized:

$$t = \frac{L}{V}\tau, \quad \mathbf{R} = L\mathbf{r}, \quad \mathbf{V} = V\mathbf{v}(\tau, \mathbf{r}), \quad \mathbf{B} = B\mathbf{b}(\tau, \mathbf{r}), \quad \Pi = \rho V^2 p(\tau, \mathbf{r}), \tag{1.19}$$

and the system (1.15)-(1.18) becomes

$$\nabla \cdot \mathbf{v} = 0, \tag{1.20}$$

$$\frac{\partial \mathbf{v}}{\partial \tau} + (\mathbf{v} \cdot \nabla)\mathbf{v} = -\nabla p + \frac{\mathrm{Ha}^2}{\mathrm{Re}_m \mathrm{Re}} (\mathbf{b} \cdot \nabla)\mathbf{b} + \frac{1}{\mathrm{Re}} \nabla^2 \mathbf{v}, \tag{1.21}$$

$$\nabla \cdot \mathbf{b} = 0, \tag{1.22}$$

$$\frac{\partial \mathbf{b}}{\partial \tau} = \nabla \times (\mathbf{v} \times \mathbf{b}) + \frac{1}{\mathrm{Re}_m} \nabla^2 \mathbf{b}, \tag{1.23}$$

where the non-dimensional parameters are introduced:

$$\mathrm{Re} = \frac{LV}{\nu}, \quad \mathrm{Re}_m = \frac{LV}{\eta}, \quad \mathrm{Ha} = \frac{LB}{\sqrt{4\pi\rho\nu\eta}} \tag{1.24}$$

– the Reynolds, magnetic Reynolds and Hartmann numbers. These numbers are basic scaling parameters in dissipative incompressible MHD system. Each of them has a specific physical meaning and qualitatively they can be represented as follows:

$$\begin{aligned} \mathrm{Re} &= \frac{\text{Inertial forces}}{\text{Viscous forces}} = \frac{\text{Convection of velocity}}{\text{Diffusion of velocity}}, \\ \mathrm{Re}_m &= \frac{\text{Inertia forces}}{\text{Resistive forces}} = \frac{\text{Convection of magnetic field}}{\text{Diffusion of magnetic field}}, \\ \mathrm{Ha} &= \left(\frac{\text{Electromagnetic forces}}{\text{Viscous forces}}\right)^{1/2}. \end{aligned} \tag{1.25}$$

Using combinations of numbers (1.24), it is possible to obtain other non-dimensional scaling parameters. For example, the magnetic Prandtl number (or Batchelor number), Pr_m, often encountered in literature is defined as the ratio of the magnetic Reynolds number to the Reynolds number (which is exactly the ratio of the fluid viscosity to its resistivity):

$$\mathrm{Pr}_m = \frac{\mathrm{Re}_m}{\mathrm{Re}} = \frac{\nu}{\eta}. \tag{1.26}$$

The magnetic Prandtl number is characteristic of the fluid only and does not depend on the properties of the flow.

In the limit of zero dissipation ($\nu \to 0$ and $\eta \to 0$), equations (1.15)-(1.18) constitute *ideal incompressible* MHD model. In non-dimensional form this model corresponds to the system (1.20)-(1.23) in which the terms with Laplacian ∇^2 are neglected. There is only one scaling parameter in this model – a so-called Alfven number:

$$\mathrm{Al} = \frac{\mathrm{Ha}^2}{\mathrm{Re}_m \mathrm{Re}} = \left(\frac{V_A}{V}\right)^2, \tag{1.27}$$

where V_A is the Alfven velocity

$$V_A = \frac{B}{\sqrt{4\pi\rho}}. \tag{1.28}$$

Formally, ideal incompressible MHD is applicable for describing of liquid metal flows if the Reynolds and the magnetic Reynolds numbers of the flow are large, i.e. $\mathrm{Re} \gg 1$ and $\mathrm{Re}_m \gg 1$.

1.4 Methods of study

1.4.1 Equilibrium of MHD flows in channels

In fluid dynamics, equilibrium is understood as the state in which the spatial distributions of fluid parameters (velocity, density, pressure, magnetic field) are stationary, i.e. their partial derivatives with respect to time are zero, $\partial/\partial t \to 0$. For incompressible MHD flows that means:

$$\nabla \cdot \mathbf{v}_e = 0, \tag{1.29}$$

$$(\mathbf{v}_e \cdot \nabla)\mathbf{v}_e = -\nabla p_e + \frac{\mathrm{Ha}^2}{\mathrm{Re}_m \mathrm{Re}} (\mathbf{b}_e \cdot \nabla)\mathbf{b}_e + \frac{1}{\mathrm{Re}} \nabla^2 \mathbf{v}_e, \tag{1.30}$$

$$\nabla \cdot \mathbf{b}_e = 0, \tag{1.31}$$

$$0 = \nabla \times (\mathbf{v}_e \times \mathbf{b}_e) + \frac{1}{\mathrm{Re}_m} \nabla^2 \mathbf{b}_e, \tag{1.32}$$

where subscript e denotes the equilibrium quantity.

Theoretical analysis of equilibrium MHD flows in channels is performed in numerous papers (see, for example, reviews [7, 14, 15]). As mentioned above, the most

studied case is MHD flow in a straight channel since it is tightly related to different engineering applications. A number of analytical methods have been developed to determine the equilibrium flow structure in straight channels under various conditions; these methods can be also applied for analysis of annular channels. Braginskii [61] developed a galvanic approximation, which is valid at small magnetic Reynolds numbers ($\mathrm{Re}_m \ll 1$); Hunt [62] obtained exact solutions for certain types of flows in straight channels; Hunt and Stewartson [63] developed an asymptotic method to analyze flows in straight channels at high Hartmann numbers ($\mathrm{Ha} \gg 1$), this method was then refined [64] and generalized to the case of annular channels [59].

A quite general approach for the analytical description of MHD flows with small magnetic Prandtl numbers in transverse magnetic field was proposed in [65]. This approach is based on the averaging of the original equation of motion along the magnetic field lines. In the case of annular channel, such method allows the reduction of system (1.29)-(1.32) to one scalar equation for the radial profile of azimuthal velocity. In Chapter 2, this method will be used to find approximately the equilibrium profiles of electrically driven and Taylor-Couette flows in a cylindrical geometry.

Despite the progress in the analytical description of MHD channel flows, a key role in this area is played by numerical methods. For the calculation of stationary MHD flows in rectangular channels, a variety of numerical methods are developed, for example, the finite element method (see [66] and references therein), the finite volume method [67, 68], and the differential quadrature method [69]. In principle, these methods impose no limitations on the parameters of the flow and allow generalization to the unsteady (dynamic) case.

For the calculation of stationary two-dimensional MHD flows of liquid metals in rectangular channels, a new iterative method has been developed recently [70]. The method utilizes a finite difference scheme with Jacobi iterations for solving two-dimensional elliptical equations. This method has advantages inherent in all iterative methods, such as a relatively simple numerical scheme, a smooth solution, and the necessity to store in memory only $O(N^2)$ numbers at each iteration (here, N is the number of grid points in both direction). At the same time, the speed of this method

in the optimal case is $O(N^3)$, which is comparable with the fastest direct methods, where the speed is $O(N^2 \ln N)$ [71]. In Chapter 2, this iterative method is described in detail and used to calculate the properties of the MHD flow in an annular channel. The stability of the method is analyzed in Appendix A.

1.4.2 Stability of systems with MHD flows

The problem of stability is one of the most interesting and important problems in magnetohydrodynamics. Intuitively, the stability of the dynamic system is understood as the "proximity" of that system to the initial equilibrium state at any time after the system was perturbed. Since the different terminology in literature related to stability study is used, we will specify the terms used in the present thesis.

A mathematically correct definition of stability was given by Lyapunov [72]. Consider an autonomous dynamic system

$$\frac{d\mathbf{x}}{dt} = \mathbf{f}(\mathbf{x}), \tag{1.33}$$

where $\mathbf{x}(t)$ denotes the system state vector. Suppose the system has an equilibrium point $\mathbf{x}_e$, i.e.,

$$\mathbf{f}(\mathbf{x}_e) = 0. \tag{1.34}$$

Definition 1.1 (Nonlinear stability) *The equilibrium point $\mathbf{x}_e$ is said to be nonlinearly stable (or Lyapunov stable), if for every $\varepsilon > 0$ there exists a $\delta = \delta(\varepsilon) > 0$, such that, if $\|\mathbf{x}(0) - \mathbf{x}_e\| < \delta$, then $\|\mathbf{x}(t) - \mathbf{x}_e\| < \varepsilon$ for every $t \geq 0$.*

In other words, nonlinear stability of an equilibrium means that the state of the system remains arbitrary close to the equilibrium point (within a distance ε from it) if the initial perturbed state is sufficiently close to it (within a distance δ from it). Note that this must be true for any ε that one may want to choose. This definition presupposes well-defined dynamics and a specified norm $\|\ \|$. Introducing different norms one can obtain, in general, different stability conditions. The following Lyapunov theorem gives a sufficient stability condition.

Theorem 1.2 (Lyapunov) *If there is a scalar function $U(\mathbf{x})$, such that, for every $\mathbf{x}$ from some neighborhood of $\mathbf{x}_e$:*

1) $U(\mathbf{x} \neq \mathbf{x}_e) > U(\mathbf{x}_e)$,

2) $dU(\mathbf{x})/dt = dU(\mathbf{x})/d\mathbf{x} \cdot \mathbf{f}(\mathbf{x}) \leq 0$,

then the equilibrium point $\mathbf{x}_e$ is nonlinearly stable. The function $U(\mathbf{x})$ is called a Lyapunov function.

There is no regular method to construct a Lyapunov function. For conservative systems a natural Lyapunov function candidate is the total energy of the system $E(\mathbf{x})$. Such a function satisfies conditions 2 automatically. In this case, to obtain a stability criterion it is enough to verify the convexity of $E(\mathbf{x})$ at an equilibrium point $\mathbf{x}_e$ (condition 1); this can be done by means of the following simple theorem.

Theorem 1.3 *The function $U(\mathbf{x})$ is convex at the point $\mathbf{x}_e$, i.e., the condition 1 of Theorem 1.2 is satisfied, if*

1) $dU(\mathbf{x}_e) = 0$,

2) $d^2U(\mathbf{x}_e) > 0$.

Since the stability of the system is determined by the dynamics near the equilibrium point, the linearized equations are usually considered in stability analysis. The following concepts of stability are used in literature.

Definition 1.4 (Spectral stability) *The equilibrium point $\mathbf{x}_e$ is said to be spectrally stable if the spectrum of the linearized operator $d\mathbf{f}(\mathbf{x}_e)/d\mathbf{x}$ has no strictly positive real part. Spectral stability guarantees the absence of perturbations with exponential growth in time.*

Definition 1.5 (Linear stability) *The equilibrium point $\mathbf{x}_e$ is said to be linearly stable relative to a norm $\|\boldsymbol{\xi}\|$ of infinitesimal variations $\boldsymbol{\xi}$, if for every $\varepsilon > 0$ there exists a $\delta = \delta(\varepsilon) > 0$, such that, if $\|\boldsymbol{\xi}(0)\| < \delta$, then $\|\boldsymbol{\xi}(t)\| < \varepsilon$ for every $t \geq 0$, where $\boldsymbol{\xi}$ evolves according to linearized equation*

$$\frac{d\boldsymbol{\xi}}{dt} = \frac{d\mathbf{f}(\mathbf{x}_e)}{d\mathbf{x}} \cdot \boldsymbol{\xi}. \tag{1.35}$$

$$\begin{array}{ccc} \textbf{Formal} & \longrightarrow & \textbf{Nonlinear} \\ \Downarrow & & \Downarrow \\ \textbf{Linear} & \Longrightarrow & \textbf{Spectral} \end{array}$$

Figure 1.3: Hierarchy of different concepts of stability. Double arrow means sufficiency for both finite and infinite dimensional systems, single arrow means sufficiency only for finite dimensional systems.

Definition 1.6 (Formal stability) *The equilibrium point* $\mathbf{x}_e$ *is said to be formally stable, if there exists a Lyapunov function* $U(\boldsymbol{\xi})$ *for linearized equation (1.35).*

The hierarchy of different concepts of stability can be represented by the scheme shown in Fig. 1.3. Spectral stability is necessary for both linear and nonlinear stability (since, if the spectrum had a strictly positive real part, there would be an unstable eigen space), but it is not sufficient. For example, the equilibrium solution $(p_e,\ q_e) = (0,\ 0)$ for the dynamics generated by the Hamiltonian[3] $\mathcal{H}(p,\ q) = p^2 + q^4$ is spectrally but not linearly stable. The same example shows that a non-linear stability does not guarantee a linear one. The converse is also true: linear stability is not a sufficient condition for a non-linear stability, such as in the system $dx/dt = x^2$, whose equilibrium $x_e = 0$ is linearly stable.

Formal stability implies linear stability since in this case the Lyapunov function $U(\boldsymbol{\xi})$ provides a norm preserved by linearized equations. The converse is not generally true[4]. In finite dimensions, formal stability also ensures nonlinear stability (a classical result of Lagrange). Infinite dimensional systems (continuous media), which are of concern to us in present thesis, have some differences.

We note that all of the definitions given above are transferred naturally to the

[3]The dynamics generated by Hamiltonian $\mathcal{H}(\mathbf{p},\ \mathbf{q})$ is defined as

$$\begin{aligned} \frac{dp_j}{dt} &= -\frac{\partial \mathcal{H}}{\partial q_j}, \\ \frac{dq_j}{dt} &= \frac{\partial \mathcal{H}}{\partial p_j}. \end{aligned}$$

[4]We did not find the rigorous proof of this statement, but it is accepted in the physical community (see, for example, [26])

case of continuous media by means of the following transformations:

- vector $\mathbf{x}(t) \longmapsto$ vector-function $\mathbf{u}(t, \mathbf{R})$,
- function $U(\mathbf{x}) \longmapsto$ functional $U(\mathbf{u})$,
- derivative $dU(\mathbf{x})/d\mathbf{x} \longmapsto$ variational derivative $\delta U(\mathbf{u})/\delta\mathbf{u}$.

The hierarchy of different definitions of stability is also valid (see Fig. 1.3). However, for continuous media the formal stability does not necessarily mean nonlinear stability; indeed, physically realistic examples from elasticity show that an equilibrium solution can have positive second variation of energy and still have an infinite number of unstable directions [73]. Nevertheless, formal stability is an important step toward the study of nonlinear stability.

The majority of stability studies in MHD are related to the concept of spectral stability (see encyclopedic monographs [74, 75], a detailed review of basic approaches for description of MHD instabilities is given in [76]). The methodological difficulty of correct spectral stability analysis is in the necessity of finding not only the eigen-values of the linearized system but also the corresponding eigen-vectors, which have to satisfy the particular boundary conditions. Besides, in the case of systems with MHD flows the linear operator of dynamics becomes non-Hermitian (non-self-adjoint), therefore its eigen-values are generally complex. In Chapters 3 and 4 we present a detailed spectral stability analysis of electrically driven flow with rotation profile (1.5) in the frames of ideal and dissipative MHD models, respectively.

In order to make a judgement about the stability of the equilibrium state, the knowledge of real dynamics of the system is not necessary; the solution often can be found by means of variational methods, in particular by means of the Lyapunov theorem. The variational approach for the stability study of static (without stationary flow) equilibrium of conservative (ideal) MHD systems – the so-called *energy principle* – was first realized in the work [24], where it was shown that the positive definiteness of second variation of potential energy W at the equilibrium state guaranties its spectral stability:

$$\delta^2 W > 0. \tag{1.36}$$

This condition follows from the Lyapunov theorem if the total energy of the system is chosen as a Lyapunov functional candidate and the minimization over momenta, contributing only to non-negative kinetic energy, is made. Actually, the form of condition (1.36) implies nonlinear stability of an ideal MHD system. However, in fluid dynamics, strict inequalities, such as (1.36), are almost never satisfied due to the presence of so-called neutral perturbations in the system (see Chapter 5). Therefore, one can usually establish only a positive semi-definiteness of the Lyapunov functional candidate, i.e., $\delta^2 U \geq 0$, which is not enough for a nonlinear (or formal) stability but still ensures a spectral one.

Because of its physical clearness, the energy principle is quite popular in the stability analysis of simple MHD systems (see, for example, [76,77]). From a practical point of view it is important that it gives also a necessary condition for the spectral stability of static MHD equilibria [78]; in other words, if there is a perturbation for which $\delta^2 W < 0$ then the equilibrium is unstable.

The first attempt to apply this approach to the study of the stability of ideal systems with stationary MHD flows was performed by Frieman and Rotenberg [23]. However, in this case the stability condition, formally coincident with the energy principle (1.36), is only sufficient for spectral stability, i.e., if it is not valid for some perturbation then nothing can be said about the stability of the equilibrium. It can be shown that this condition is never satisfied, except for a small class of MHD equilibria with special types of flow [23, 79]. Such stiffness of the energy principle (1.36), in the case of MHD flows, comes from the excessive freedom of variables in the variational procedure, which is not predetermined by the real dynamics of the system.

The improved (closer to a necessary) condition for the stability of ideal MHD equilibria with flows can be obtained if the additional constraints among the coordinates and momenta in the energy functional are taken into account. For example, if the dynamics of the system possesses other integrals of motion (conservative quantities) different from energy, the sign definiteness of the second variation of the energy functional has to be established only for the class of perturbations which do not

change the equilibrium values of those integrals. Mathematically, these ideas have been formulated by Arnold [80–82] in the following theorem, which gives a sufficient condition for stability.

Theorem 1.7 (Arnold) *Suppose that a dynamic system (1.33) has a set of first integrals (conservative quantities)* $E(\mathbf{x})$, $I_1(\mathbf{x})$, $\ldots$, $I_k(\mathbf{x})$. *Consider their linear combination:*

$$U(\mathbf{x}) = E(\mathbf{x}) + \lambda_1 I_1(\mathbf{x}) + \ldots + \lambda_k I_k(\mathbf{x}). \tag{1.37}$$

Suppose that there exist Lagrange multipliers λ_1, $\ldots$, λ_k *such that:*

1) the first variation of $U(\mathbf{x})$ *is zero at the equilibrium point* $\mathbf{x}_e$, *i.e.*

$$dU(\mathbf{x}_e) = dE(\mathbf{x}_e) + \lambda_1 dI_1(\mathbf{x}_e) + \ldots + \lambda_k dI_k(\mathbf{x}_e) = 0; \tag{1.38}$$

2) the second variation of $U(\mathbf{x})$ *at* $\mathbf{x}_e$

$$d^2U(\mathbf{x}_e) = d^2E(\mathbf{x}_e) + \lambda_1 d^2I_1(\mathbf{x}_e) + \ldots + \lambda_k d^2I_k(\mathbf{x}_e) \tag{1.39}$$

is sign-definite on a subspace

$$dI_1(\mathbf{x}_e) = 0, \ \ldots, \ dI_k(\mathbf{x}_e) = 0. \tag{1.40}$$

Then $U(\mathbf{x})$ *is a Lyapunov function and the equilibrium point* $\mathbf{x}_e$ *is stable.*

It is obvious that the more invariants that are taken into account, the closer Lyapunov stability criterion will be to a necessary stability condition. Therefore, Arnold's method is reduced to the search of additional invariants inherent in the dynamic system, incorporating them with energy to form a Lyapunov function candidate and analyzing its sign-definiteness.

If the dynamic system has a Hamiltonian formulation then an algorithm for finding new invariants can be produced. It is known that the dynamics of any quantity f in a Hamiltonian system is determined by the Hamiltonian functional $\mathcal{H}(\mathbf{p}, \mathbf{q})$ and Poisson brackets [83]:

$$\frac{df}{dt} = \frac{\partial f}{\partial t} + \{f, \mathcal{H}\}. \tag{1.41}$$

Therefore, if some function f has no explicit dependence on time and commutes with the Hamiltonian, i.e.

$$\{f, \mathcal{H}\} = 0, \tag{1.42}$$

then it is an integral of motion. It was shown in [84] that ideal MHD has a Hamiltonian formulation in terms of *non-canonical* Poisson brackets[5]. Among other properties, these brackets can have the important property of redundancy, which is characterized by the existence of some functional(s) $\mathcal{C}$ commuting with *any* Hamiltonian $\mathcal{H}$:

$$\{\mathcal{C}, \mathcal{H}\} = 0. \tag{1.43}$$

The functional $\mathcal{C}$ is called *Casimir invariant*; by definition it is an integral of motion.

Arnold's theorem and the formulation of ideal MHD in terms of non-canonical Poisson brackets gave rise to a new approach in MHD stability analysis, called the Energy-Casimir stability method (EC-method, see [26, 85–87]). In the EC-method, the Lyapunov functional candidate is built in the form

$$U = \mathcal{H} + \sum_j \mathcal{C}_j, \tag{1.44}$$

where $\mathcal{H}$ is the Hamiltonian of the system and $\mathcal{C}_j$ is the known set of Casimir invariants. However, in the quite extensive literature on the EC-method, the Arnold's method is not realized completely. Namely, when the second variation of the functional U is considered, the constraints imposed by conservation of the Casimir invariants $\mathcal{C}_j$ are not taken into account (condition (1.40) in Theorem 1.7). Without that, the EC-method is reduced to a study of "shifted" Hamiltonian (1.44), which eventually gives the same stability condition as (1.36).

The degeneracy of non-canonical Poisson brackets (and, therefore, the presence of Casimir invariants) is related to the existence of the special symmetry in MHD

[5] In a finite-dimensional case the Poisson brackets have *canonical* form:

$$\{f, g\} = \sum_{j=1}^{n} \left(\frac{\partial f}{\partial q_j} \frac{\partial g}{\partial p_j} - \frac{\partial f}{\partial p_j} \frac{\partial g}{\partial q_j} \right).$$

systems (topological or geometrical); due to this symmetry, stationary flows are possible. Another method to find the integrals of motion, accounting for this symmetry, was used by Ilgisonis and Pastukhov [88], who employed Noether's theorem in the Lagrangian representation of MHD. Following Arnold's method, they used these integrals in stability analysis of the MHD system with nested magnetic surfaces and showed that the stability condition (1.36) can be improved in this case. An analogous stability condition has been obtained by Hameiri [25,89], who used the method of dynamically accessible perturbations to take into account the conservation of Casimir invariants. However, even this (improved) stability condition is very stiff and far from the necessary one.

The problem of finding new invariants is significantly simplified if the linearized MHD system is considered. In this case, the system possesses an infinite set of nontrivial integrals of motion [90], which have no analogues in nonlinear dynamics. The inclusion of one or several such invariants into stability analysis makes it possible to obtain a sufficient condition for the stability of MHD flows. The condition appears to be softer (closer to a necessary one) than the previously known conditions. In Chapter 5, the variational method of stability study based on these new invariants is developed.

1.5 Thesis outline

The material of the thesis is divided into 6 Chapters and 2 Appendices.

In Chapter 2, the stationary axisymmetric flow of incompressible conducting fluid (liquid metal) in an annular channel is studied analytically and numerically in the frame of dissipative MHD. Two cases are considered: electrically driven flow and Taylor-Couette flow. In each case, the dependence of the angular momentum profile on the Hartmann and Reynolds numbers are investigated. It is shown that at large values of the Reynolds number, the inertia effects become important and affects the angular momentum profile significantly. Also, a detailed description of the numerical scheme used for the calculation of the equilibrium velocity and the induced magnetic

field is presented. The scheme is based on a finite-difference method with Jacobi iterations.

In Chapter 3, the spectral stability of an incompressible fluid differentially rotating in a transverse magnetic field is studied numerically by solving the eigenvalue problem with rigid-wall boundary conditions. The study is performed in the frame of ideal MHD, neglecting all dissipative effects (resistivity and viscosity). The equilibrium velocity profile used in calculations corresponds to the electrically driven flow in a circular channel with the rotation law (1.5). Eigen-frequency spectra are calculated for both axisymmetric (with azimuthal mode-number $m = 0$) and non-axisymmetric ($m \neq 0$) modes. The dependence of MRI growth rate on the axial k_z and the azimuthal m mode-numbers is obtained. The analytical expression for stability threshold is found for $m \gg 1$. The energy of the stable oscillatory eigen-modes is calculated and shown to be negative in some cases.

In Chapter 4, the spectral stability analysis of the flow (1.5) is performed numerically in the frame of dissipative MHD. The numerical procedure is based on solving the two-dimensional eigen-value problem for both axisymmetric and non-axisymmetric modes (with azimuthal mode-numbers up to $m = 200$). The dependence of the instability threshold of these modes on the Hartmann and Reynolds numbers is studied. Our results are compared with available experimental data.

In Chapter 5, the variational method for the study of the formal stability of ideal MHD flows is developed. The method is based on establishing sign-definiteness of a Lyapunov functional candidate which incorporates energy with new integrals of motion, inherent in the linearized MHD system. The construction of these integrals is described. The sufficient and necessary condition for stability of ideal MHD flows is formulated in variational form. An analytical example is presented to confirm the fruitfulness of the developed method.

In Chapter 6, the major results of the thesis are summarized.

In Appendix A, the stability of a numerical scheme for calculation of stationary MHD flows in channels is studied. In Appendix B, the proof of Fredholm's theorem for Hermitian operators is presented.

Chapter 2

Equilibrium MHD flows in annular channels

In this chapter the theoretical study of equilibrium MHD flows in annular channels is performed from the perspective of establishing required parameters for liquid metal MRI experiments. Two different types of fluid rotation are considered: electrically driven flow and Taylor-Couette flow between rotating cylinders. We study a structure of these flows within a unified approach as a function of the Hartmann and Reynolds numbers and compare the conditions which have to be satisfied in both cases to realize the rotation profiles appropriate for MRI excitation.

2.1 Statement of the problem

2.1.1 Model and equations

We consider the problem of finding the equilibrium flow of liquid metal in an annular channel with a rectangular cross section. At this point, the mechanism of flow drive is not specified: it can be either Taylor-Couette flow (Fig. 1.1) or electrically driven flow (Fig. 1.2). This mechanism will be specified below by an appropriate choice of boundary conditions.

The channel is an axisymmetric toroid whose axis of symmetry coincides with the z axis of the cylindrical coordinate system $\{r,\ \varphi,\ z\}$. We make the following assumptions:

1) liquid metal is homogeneous: its density ρ, kinematic viscosity ν, and resistivity

η are constant throughout the entire volume;

2) liquid metal completely fills the channel;

3) the channel is placed into an external uniform magnetic field directed along the z axis, $\mathbf{B}_0 = B_0\mathbf{e}_z$.

It is easy to see that these assumptions do not break the axial symmetry related to the channel geometry[1]. This circumstance allows one to simplify the problem substantially and reduce it to the study of two-dimensional (axisymmetric) flow.

The equilibrium flow of liquid metal in a magnetic field is described by equations of the incompressible dissipative MHD model (1.29)-(1.32). In these non-dimensional equations, as a unit of length we use $L = H/2$, where H is the height of the channel; the characteristic value of the magnetic field is taken to be B_0; the characteristic value of velocity V will be specified later on, depending on the type of the flow.

In the case of axial symmetry, it is convenient to represent the equilibrium velocity $\mathbf{V}_e$ and magnetic field $\mathbf{B}_e$ in the form:

$$\mathbf{V}_e = V\mathbf{v}_e = V\left(\frac{1}{r}\nabla w(r,z)\times\mathbf{e}_\varphi + \frac{u(r,z)}{r}\,\mathbf{e}_\varphi\right), \tag{2.1}$$

$$\mathbf{B}_e = B_0\mathbf{b}_e = B_0\mathbf{e}_z + B_0\frac{\mathrm{Re}_m}{\mathrm{Ha}}\left(\frac{1}{r}\nabla g(r,z)\times\mathbf{e}_\varphi + \frac{h(r,z)}{r}\,\mathbf{e}_\varphi\right). \tag{2.2}$$

Here, functions w and g are poloidal stream functions of the velocity and the magnetic field, u and h represent angular momentum of the fluid and "momentum" of the azimuthal magnetic field, respectively. The coefficient $\mathrm{Re}_m/\mathrm{Ha}$ in expression (2.2) characterizes the ratio of induced magnetic field to the external one. As shown in [70], the function h in this case has a magnitude on the order of unity. Expressions for the equilibrium velocity (2.1) and the magnetic field (2.2) automatically satisfy divergence-free conditions (1.29) and (1.31), correspondingly. Other two equations,

[1]Mathematically, axial symmetry means that all physical quantities in the system have no dependence on the azimuthal angle, i.e., $\partial/\partial\varphi = 0$.

(1.30) and (1.32), after some mathematical manipulations give:

$$0 = \Delta^* u + \mathrm{Ha}\frac{\partial h}{\partial z} + \frac{\mathrm{Re}}{r}[u,w] - \frac{\mathrm{Re}_m}{r}[h,g], \tag{2.3}$$

$$0 = \Delta^* h + \mathrm{Ha}\frac{\partial u}{\partial z} + \mathrm{Re}_m r\left(\left[g,\frac{u}{r^2}\right] - \left[w,\frac{h}{r^2}\right]\right), \tag{2.4}$$

$$0 = \Delta^*\Delta^* w + \mathrm{Ha}\frac{\partial}{\partial z}\Delta^* g - \mathrm{Re}\left(r\left[w,\frac{\Delta^* w}{r^2}\right] + \frac{1}{r^2}\frac{\partial u^2}{\partial z}\right) + \\ + \mathrm{Re}_m\left(r\left[g,\frac{\Delta^* g}{r^2}\right] + \frac{1}{r^2}\frac{\partial h^2}{\partial z}\right), \tag{2.5}$$

$$0 = \Delta^* g + \mathrm{Ha}\frac{\partial w}{\partial z} + \frac{\mathrm{Re}_m}{r}[g,w], \tag{2.6}$$

where the following notation is used

$$[f,g] \equiv \frac{\partial f}{\partial r}\frac{\partial g}{\partial z} - \frac{\partial f}{\partial z}\frac{\partial g}{\partial r}, \quad \Delta^* = r\frac{\partial}{\partial r}\frac{1}{r}\frac{\partial}{\partial r} + \frac{\partial^2}{\partial z^2}.$$

We note, that equations (2.3) and (2.4) are the azimuthal components of equations (1.30) and (1.32), respectively, and equations (2.5) and (2.6) are obtained from two other components of equations (1.30) and (1.32).

In principle, the system (2.3)-(2.6) can be solved for any values of Hartmann, Reynolds, and magnetic Reynolds (or magnetic Prandtl) numbers. In the present study we restrict ourselves to the case of small magnetic Prandtl numbers, $\mathrm{Pr}_m \ll 1$, which is valid for most liquid metals (for example, mercury at normal temperature has $\mathrm{Pr}_m = 1.4\cdot 10^{-7}$). In this approximation, all the terms with Re_m can be neglected and the system (2.3)-(2.6) is reduced to simplified form:

$$0 = \Delta^* u + \mathrm{Ha}\frac{\partial h}{\partial z} + \frac{\mathrm{Re}}{r}[u,w], \tag{2.7}$$

$$0 = \Delta^* h + \mathrm{Ha}\frac{\partial u}{\partial z}, \tag{2.8}$$

$$0 = \Delta^*\Delta^* w - \mathrm{Ha}^2\frac{\partial^2 w}{\partial z^2} - \mathrm{Re}\left(r\left[w,\frac{\Delta^* w}{r^2}\right] + \frac{1}{r^2}\frac{\partial u^2}{\partial z}\right). \tag{2.9}$$

This system of equations is the basis for our analysis of equilibrium axisymmetric MHD flow of a liquid metal in an annular channel.

2.1.2 Boundary conditions

In order to solve system (2.7)-(2.9), it is necessary to establish boundary conditions that should be imposed on unknown functions.

According to the standard hydrodynamic condition, the velocity of viscous fluid at a solid wall should be equal to the velocity of this wall $\mathbf{v}^{(w)}$ [91]:

$$\mathbf{v}|_\Gamma = \mathbf{v}^{(w)}|_\Gamma, \tag{2.10}$$

where Γ denotes the boundary between the fluid and the wall. In our case Γ is defined as:

$$\Gamma = \{z = \pm 1 \ \text{ (top and bottom walls)}, \quad r = r_{1,2} = \frac{2R_{1,2}}{H} \ \text{ (side walls)}\}. \tag{2.11}$$

The boundary conditions for the magnetic field can be obtained from the conditions on the electric current density $\mathbf{J}$, which are determined by the conductivity of the walls. From Maxwell's equation (1.12) it follows that, at the interface between two media, the tangential component of the electric field is continuous:

$$E_t|_\Gamma = E_t^{(w)}|_\Gamma. \tag{2.12}$$

This condition should be also satisfied in the reference frame, moving with the wall, i.e.

$$E_t^*|_\Gamma = E_t^{*(w)}|_\Gamma, \tag{2.13}$$

where the electric field $\mathbf{E}^*$ in a moving reference frame is related to the fields $\mathbf{E}$ and $\mathbf{B}$ in the laboratory reference frame by[2]

$$\mathbf{E}^* = \mathbf{E} + \frac{1}{c}(\mathbf{V} \times \mathbf{B}). \tag{2.14}$$

Taking into account (2.14) in Ohm's law (1.13), condition for the electric field (2.13) can be replaced by the condition for the tangential component of the current density:

$$\left.\frac{J_t}{\sigma}\right|_\Gamma = \left.\frac{J_t^{(w)}}{\sigma_w}\right|_\Gamma, \tag{2.15}$$

where σ and σ_w are conductivities of the fluid and the wall, respectively. The requirement $\nabla \cdot \mathbf{J} = 0$, which follows from Maxwell's equation (1.11), gives the continuity of the normal component of the current density at the interface:

$$J_n|_\Gamma = J_n^{(w)}|_\Gamma. \tag{2.16}$$

[2]The relation (2.14) is valid up to terms of order $O(V^2/c^2)$.

In the cases of ideally conducting and insulating walls, conditions (2.15) and (2.16) are simplified. For ideally conducting wall $\sigma_w \to \infty$, therefore, the tangential component of the current density at the interface should be zero, i.e.,

$$J_t = 0 \quad \text{(ideally conducting wall)}. \tag{2.17}$$

Since there is no current inside the insulating wall, the normal component of the fluid current density at the boundary is zero, i.e.,

$$J_n = 0 \quad \text{(insulating wall)}. \tag{2.18}$$

Conditions (2.17) and (2.18) along with equation (1.11) are enough to specify the boundary conditions for function h (the "momentum" of the azimuthal magnetic field).

We note that the geometry of the problem implies symmetry with respect to the plane $z = 0$. Therefore, the unknown functions are either even or odd functions of z. In our study we take u to be even, h and w to be odd functions of z; these requirements do not contradict system (2.7)-(2.9) and satisfy the corresponding boundary conditions.

2.2 Numerical method

In this section, we describe a numerical method developed to solve a system of elliptical equations, such as system (2.7)-(2.9). This method generalizes the well-known iteration Jacobi algorithm and contains all of its specific features. To illustrate them, we consider as an example the solution of the Poisson equation (for more details, see [71]).

For a two-dimensional function $\phi(x, y)$, the Poisson equation is

$$\frac{\partial^2 \phi}{\partial x^2} + \frac{\partial^2 \phi}{\partial y^2} = f(x, y), \tag{2.19}$$

where $f(x, y)$ is a given function. We solve this equation in a square region assuming that the unknown function ϕ is uniquely determined by imposed boundary conditions

(here, we do not concretize them). We introduce a discrete grid of points and assume that the grid spacings in the x and y directions are equal: $\delta x = \delta y = s$. The grid points can be labeled by a pair of integers (i, j), where i and j range from 0 to N. If (x_0, y_0) are the coordinates of the left lower corner of the square, then the coordinates of the point (i, j) are

$$x_i = x_0 + is, \quad y_j = y_0 + js.$$

For this grid, the discretization of equation (2.19) has the form

$$\frac{\phi_{i+1,j} + \phi_{i-1,j} - 2\phi_{i,j}}{s^2} + \frac{\phi_{i,j+1} + \phi_{i,j-1} - 2\phi_{i,j}}{s^2} = f_{i,j}, \tag{2.20}$$

where $\phi_{i,j} = \phi(x_i, y_j)$, $f_{i,j} = f(x_i, y_j)$. This equation can be represented in matrix form so that the problem is reduced to the standard problem of linear algebra – finding a solution of a system of linear equations. In practice, an often encountered situation is when the equation is nonlinear in the unknown function (for example, the right-hand side of the Poisson equation (2.19) has a nonlinear dependence on ϕ: $f(x, y) = F(\phi(x, y), x, y)$). In this case, the use of linear algebra methods is restricted and one has to resort to iterative algorithms.

The exact solution to the discretized problem (2.20) obeys the equation

$$\phi_{i,j} = \frac{1}{4}(\phi_{i+1,j} + \phi_{i-1,j} + \phi_{i,j+1} + \phi_{i,j-1} - s^2 f_{i,j}). \tag{2.21}$$

This equation cannot be solved explicitly for fixed i and j because there are 5 unknowns involved. If there is some initial approximation of the grid function $\phi^0_{i,j}$, then the equation (2.21) can be used to improve this approximation. This results in the Jacobi iteration algorithm

$$\text{Jacobi:} \quad \phi^{n+1}_{i,j} = \frac{1}{4}(\phi^n_{i+1,j} + \phi^n_{i-1,j} + \phi^n_{i,j+1} + \phi^n_{i,j-1} - s^2 f_{i,j}), \tag{2.22}$$

where n is the number of the approximation. It should be noted here, that if the function f in equation (2.19) depends on ϕ, it has to be recalculated at every step. Algorithm (2.22) is stable and converges: the number of iterations to reduce the error in the solution by a factor of 10^{-q} is $\sim qN^2/2$, where N is the number of grid points in the x and y directions. Since each iteration involves updating N^2 values of

ϕ, the calculation time of the algorithm scales as $O(N^4)$, which is very slow for large N.

The Jacobi iterative procedure can be accelerated by a factor of two if the Gauss-Seidel algorithm is used:

$$\text{Gauss-Seidel:} \quad \phi_{i,j}^{n+1} = \frac{1}{4}(\phi_{i+1,j}^{n} + \phi_{i-1,j}^{n+1} + \phi_{i,j+1}^{n} + \phi_{i,j-1}^{n+1} - s^2 f_{i,j}). \tag{2.23}$$

Here the values of the grid function are updated with increasing i and j; therefore, new values of $\phi_{i,j}$ are calculated using updated $\phi_{i-1,j}$ and $\phi_{i,j-1}$.

In order to avoid the directional asymmetry caused by the simple Gauss-Seidel algorithm (2.23), the Gauss-Seidel algorithm with checkerboard updating of the grid function is normally used. Formally, this method corresponds to a Jacobi algorithm (2.22) with two passes. The first pass updates the points with even $i + j$ ("black" points), the second with odd $i + j$ ("white" points). It is clear that updating each black point involves only four neighboring white points that were found in the previous iteration, and vice versa.

The convergence of the iterative algorithms given above can be accelerated by means of the so-called *successive over-relaxation* (SOR). In this case, a new value of the grid function at the point $(i,\ j)$ is determined by a linear combination of the old and the updated values of the function at this point:

$$\text{SOR:} \quad \phi_{i,j}^{n+1} = (1-\mu)\phi_{i,j}^{n} + \frac{\mu}{4}(\phi_{i+1,j}^{n} + \phi_{i-1,j}^{n} + \phi_{i,j+1}^{n} + \phi_{i,j-1}^{n} - s^2 f_{i,j}), \tag{2.24}$$

where μ is the relaxation parameter. The following results are proven about this parameter [71]:

1) the iterations converge only if $0 < \mu < 2$;

2) if $1 < \mu < 2$ the iterations converge faster than for $\mu = 1$ in the straight Jacobi or Gauss-Seidel methods;

3) there is an optimum value of μ for which the convergence is fastest; for a square grid in 2-D

$$\mu_{opt} \simeq \frac{2}{1 + \pi/N};$$

4) if $\mu = \mu_{opt}$ then the convergence time is $O(N^3)$.

The physical meaning of the SOR method is that, instead of direct solving the Poisson equation (2.19), one finds the stationary (relaxed) solution to the dynamical problem:

$$\frac{\partial \phi}{\partial t} = \frac{\partial^2 \phi}{\partial x^2} + \frac{\partial^2 \phi}{\partial y^2} - f(x, y). \tag{2.25}$$

Discretization of this equation for the partly implicit numerical scheme has the form:

$$\frac{\phi_{i,j}^{n+1} - \phi_{i,j}^{n}}{\tau} = \frac{\phi_{i+1,j}^{n} + \phi_{i-1,j}^{n} - 2\phi_{i,j}^{n+1}}{s^2} + \frac{\phi_{i,j+1}^{n} + \phi_{i,j-1}^{n} - 2\phi_{i,j}^{n+1}}{s^2} + g_{i,j}, \tag{2.26}$$

where τ is a time step and n is a number of the time point. Solving this equation for $\phi_{i,j}^{n+1}$, we arrive at the iterative scheme which looks exactly the same as (2.24), with the relaxation parameter being

$$\mu = \left(1 + \frac{s^2}{4\tau}\right)^{-1}. \tag{2.27}$$

It should be noted that the equations (2.22)-(2.24) give the values of the grid function only at the interior grid points, i.e., at $1 \leq i, j \leq N - 1$. The values of the grid function at the boundary points in each iteration are determined from boundary conditions. The iterations are stopped when the norm of the residual is less than some given $\epsilon > 0$:

$$\|\phi_{i,j}^{n+1} - \phi_{i,j}^{n}\| \leq \epsilon. \tag{2.28}$$

The norm of the grid function $\|A_{i,j}\|$ in this expression can be defined, for example, as the sum of the absolute values of the elements $A_{i,j}$ at the grid points.

An iterative scheme analogous to (2.24) can be constructed for any system of elliptical equations, in particular for the system (2.7)-(2.9). For this purpose, we represent it in the dynamical form

$$\frac{\partial \mathbf{y}}{\partial t} = \Delta^* \mathbf{y} + \mathbf{f}(\mathbf{y}, r), \tag{2.29}$$

where $\mathbf{y}$ is unknown vector-function

$$\mathbf{y}(r, z, t) = \begin{pmatrix} u(r, z, t) \\ h(r, z, t) \\ \tilde{w}(r, z, t) \\ w(r, z, t) \end{pmatrix},$$

and $\mathbf{f}$ is a source vector-function:

$$\mathbf{f}(\mathbf{y},r)=\begin{pmatrix} \mathrm{Ha}\dfrac{\partial h}{\partial z}+\dfrac{\mathrm{Re}}{r}\,[u,w] \\ \mathrm{Ha}\dfrac{\partial u}{\partial z} \\ -\mathrm{Ha}^2\dfrac{\partial w}{\partial z^2}-\mathrm{Re}\left(r\left[w,\dfrac{\tilde{w}}{r^2}\right]+\dfrac{1}{r^2}\dfrac{\partial u^2}{\partial z}\right) \\ -\tilde{w} \end{pmatrix}.$$

Discretization of equation (2.29) in a square region with a uniform grid yields:

$$\begin{aligned} \mathbf{y}_{i,j}^{n+1} &= (1-\mu)\mathbf{y}_{i,j}^{n}+ \\ &+ \frac{1}{4}\mu\left[\left(1-\frac{s}{2r_i}\right)\mathbf{y}_{i+1,j}^{n}+\left(1+\frac{s}{2r_i}\right)\mathbf{y}_{i-1,j}^{n}+\mathbf{y}_{i,j+1}^{n}+\mathbf{y}_{i,j-1}^{n}+s^2\mathbf{f}_{i,j}(\mathbf{y}^n,r)\right], \end{aligned} \tag{2.30}$$

where the relaxation parameter μ is defined in (2.27). In general, the relaxation parameter can be different for different equations of the same system.

The presence of several unknown functions in each equation of the system (2.29), i.e., the coupling of the equations of the system, results in conditional stability of the numerical scheme (2.30). In Appendix A, a detailed stability analysis of this scheme for the simplified case is presented. It is shown that the scheme is stable if condition (A.11) is satisfied:

$$\frac{2}{\tau}+\frac{4}{s^2}\geq \mathrm{Ha}^2. \tag{2.31}$$

Based on the finite difference scheme (2.30), a numerical code has been developed for the calculation of the equilibrium structure of axisymmetric MHD flows in an annular channel of rectangular cross-section. This code is implemented in C++ and takes the advantage of a spatial grid with a variable step, which allows us to calculate the flow in the narrow boundary layers. The time step is determined from condition (2.31). Visualization of the results of our calculations has been performed by means of MATLAB.

2.3 Electrically driven flow

In this section, we study a liquid metal flow driven by imposed electric current in the presence of a transverse magnetic field (Fig. 1.2). The study is performed for

the geometry of the Obninsk MRI experiment [49] (Table 2.1). In order to describe the characteristic features of this type of flow we consider the flow at Hartmann and Reynolds numbers different from those expected in the Obninsk experiment. The analytical part of our study is based on the method proposed in [65] which uses the averaging of the force-balance equation along the magnetic field lines.

2.3.1 Boundary conditions

For electrically driven flow the condition (2.10) gives:

$$u|_{z=\pm1} = 0, \qquad u|_{r=(r_1,r_2)} = 0, \tag{2.32}$$

$$\nabla w|_{z=\pm1} = 0, \quad \nabla w|_{r=(r_1,r_2)} = 0. \tag{2.33}$$

From (2.33), it is evident that the poloidal stream function w is determined up to an arbitrary constant w_0, i.e., $w|_\Gamma = w_0$. Since w is an odd function of z, this constant has to be zero and then the conditions (2.33) become

$$w|_{z=\pm1} = 0, \qquad w|_{r=(r_1,r_2)} = 0, \tag{2.34}$$

$$\left.\frac{\partial w}{\partial z}\right|_{z=\pm1} = 0, \quad \left.\frac{\partial w}{\partial r}\right|_{r=(r_1,r_2)} = 0. \tag{2.35}$$

The boundary conditions for the magnetic field are determined by the electrical properties of the channel walls. In the case of electrically driven flow we assume that the top and bottom walls are insulators, the side walls are perfect conductors and the electric current I_0 is passed through the channel (Fig. 2.1). Then, from (2.17) and (2.18), we have conditions for the azimuthal magnetic field

$$\left.\frac{\partial h}{\partial r}\right|_{z=\pm1} = 0, \quad \left.\frac{\partial h}{\partial r}\right|_{r=(r_1,r_2)} = 0. \tag{2.36}$$

The first equation means that the function h is constant at the top and bottom walls of the channel, i.e. $h|_{z=-1} = h_1$ and $h|_{z=1} = h_2$. The constants h_1 and h_2 are related to the total current I_0 flowing through the fluid. In order to find them, we note that the function h is odd in z. This is explained by the following simple physical reason: the magnetic field induced in the current-carrying conductor which has a

Table 2.1: Parameters of the Obninsk MRI experiment

Parameter	Value	Corresponding non-dimensional parameter	Value of non-dimensional parameter
Geometry of the channel			
Inner radius, R_1	3 cm	$r_1 = R_1/L$	$r_1 = 1$
Outer radius, R_2	15 cm	$r_2 = R_2/L$	$r_2 = 5$
Height, $H = 2L$	6 cm	$h = H/L$	$h = 2$
Properties of liquid sodium at melting point (98° C)			
Density, ρ	0.92 g/cm^3	–	–
Kinematic viscosity, ν	$7.1{\cdot}10^{-3}$ cm^2/s	$\mathrm{Pr}_m = \nu/\eta$	$\mathrm{Pr}_m = 8.8 \cdot 10^{-6}$
Resistivity, η	810 cm^2/s		
Parameters of the experiment			
Total current, I_0	$0 - 10^3$ A	$\mathrm{Re} = M_0/\nu = I_0/(\nu c\sqrt{4\pi\rho\mathrm{Pr}_m}) = 1400 \cdot I_0[\mathrm{A}]$	$\mathrm{Re} = 0 - 1.4 \cdot 10^6$
Typical angular momentum of sodium, $M_0 = I_0/(c\sqrt{4\pi\rho\mathrm{Pr}_m})$	$0 - 10^4$ cm^2/s	–	–
Velocity of sodium at R_1, $V_1 = M_0/R_1$	$0 - 3300$ cm/s	–	–
Magnetic field, B_0	0.026 T	$\mathrm{Ha} = HB_0/\sqrt{16\pi\rho\nu\eta} = 600{\cdot}H[\mathrm{cm}]{\cdot}B_0{\cdot}[\mathrm{T}]$	$\mathrm{Ha} = 100$
Alfven velocity, $V_A = B_0/\sqrt{4\pi\rho}$	72 cm/s	–	–

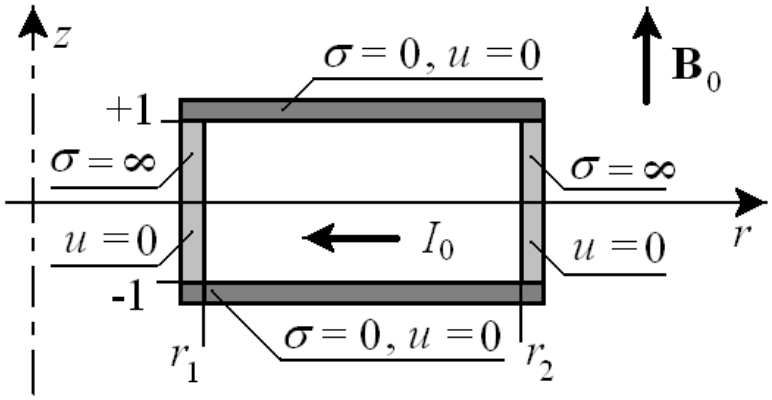

Figure 2.1: Cross section of the channel in the case of electrically driven flow. Top and bottom are insulators (conductivity $\sigma = 0$), side walls are ideal conductors ($\sigma = \infty$). All channel walls are stationary (angular momentum $u = 0$).

plane of symmetry should be antisymmetric with respect to this plane. From (1.11) and (2.2), the current density is

$$\mathbf{J} = \frac{c}{4\pi}\nabla \times \mathbf{B} = \frac{cB_0\mathrm{Re}_m}{4\pi R\mathrm{Ha}}(-\Delta^* g\mathbf{e}_\varphi + \nabla h \times \mathbf{e}_\varphi). \tag{2.37}$$

Hence, the function $h(r, z)$ is a poloidal stream function for the current density, i.e., in the $r - z$ plane, the current flows along the lines $h(r, z) = \text{const}$. The total radial current in an arbitrary section, $R = \text{const}$, of the channel is

$$I_0 = -2\pi R \int_{-L}^{L} J_r dZ = \frac{cHB_0\mathrm{Re}_m}{4\mathrm{Ha}} \int_{-1}^{1} \frac{\partial h}{\partial z} dz = \frac{cHB_0\mathrm{Re}_m}{2\mathrm{Ha}}\, h_2, \tag{2.38}$$

since h is an odd function of z. The positive sign of the total current, $I_0 > 0$, corresponds to a current flowing from the outer to the inner channel wall.

As discussed in [70], it is convenient to choose $h_2 = 1$ (and $h_1 = -1$, respectively), then the value $h(r, z)$ shows the part of the total current flowing between planes $-z$ and z at given radius r. Moreover, from equation (2.38) and definitions (1.24) one obtains the characteristic value of angular momentum of the electrically driven fluid:

$$M_0 \equiv LV = \frac{I_0}{c\sqrt{4\pi\rho\mathrm{Pr}_m}}. \tag{2.39}$$

It should be stressed here that the characteristic value of the angular momentum (2.39) is independent of the magnetic field; this is explained in more detail in [61].

From (1.24), the Reynolds number in electrically driven flow is defined as

$$\mathrm{Re} \equiv \frac{M_0}{\nu} = \frac{I_0}{\nu c\sqrt{4\pi\rho \mathrm{Pr}_m}}.$$

Such definition of Re is very convenient since it is not related to a particular structure of the flow.

Finally, the boundary conditions for the system (2.7)-(2.9), in the case of electrically driven flow, are

$$u|_{z=\pm 1} = 0, \qquad u|_{r=(r_1,r_2)} = 0, \tag{2.40}$$

$$h|_{z=\pm 1} = \pm 1, \qquad \left.\frac{\partial h}{\partial r}\right|_{r=(r_1,r_2)} = 0, \tag{2.41}$$

$$w|_{z=\pm 1} = 0, \qquad w|_{r=(r_1,r_2)} = 0, \tag{2.42}$$

$$\left.\frac{\partial w}{\partial z}\right|_{z=\pm 1} = 0, \qquad \left.\frac{\partial w}{\partial r}\right|_{r=(r_1,r_2)} = 0. \tag{2.43}$$

2.3.2 Hartmann flow

First, we consider electrically driven flow in the central part of the channel far from the side walls. In this case one can neglect the radial dependence of flow parameters ($\partial/\partial r \to 0$) and then the system (2.7)-(2.9) is reduced to equations:

$$0 = \frac{\partial^2 u}{\partial z^2} + \mathrm{Ha}\frac{\partial h}{\partial z}, \tag{2.44}$$

$$0 = \frac{\partial^2 h}{\partial z^2} + \mathrm{Ha}\frac{\partial u}{\partial z}. \tag{2.45}$$

The same system of equations is obtained in analysis of the equilibrium liquid metal flow between two infinite plates in a transverse magnetic field (the so-called *Hartmann flow*, [1, 2]). The difference is only in the physical meaning of the functions u and h: for Hartmann flow they are normalized components of velocity and induced magnetic field, respectively; for annular channel they are normalized angular momentum ($u = rv_\varphi$) of the fluid and "momentum" of azimuthal magnetic field (or poloidal stream function of the current density, $h = rb_\varphi$).

The exact solution of the system (2.44), (2.45) satisfying the boundary conditions

(2.40), (2.41) is

$$u(z) = \frac{\cosh \mathrm{Ha} - \cosh(\mathrm{Ha}\, z)}{\sinh \mathrm{Ha}}, \tag{2.46}$$

$$h(z) = \frac{\sinh(\mathrm{Ha}\, z)}{\sinh \mathrm{Ha}}. \tag{2.47}$$

These dependencies are shown in Fig. 2.2 and 2.3 for different values of Hartmann number. For large Hartmann numbers $\mathrm{Ha} \gg 1$ the normalized angular momentum $u(z)$ is close to 1 almost entirely in the cross-section of the channel and decreases rapidly to zero in the boundary layers of thickness $O(\mathrm{Ha}^{-1})$ – the so-called Hartmann layers. The poloidal stream function of the current density $h(z)$, on the contrary, is zero in the bulk of the flow and its absolute value increases to 1 in the Hartmann layers. This means that almost all the current in the moving fluid is expelled to the walls and flows in the thin Hartmann layers. In these layers, the viscous forces are balanced by the Ampere force. In the core region, the viscous forces and currents are negligible, so the flow is practically force-free.

The Hartmann profile of angular momentum (2.46) is of crucial importance in the study of equilibrium MHD flows in annular channels. As shown below, at large Hartmann numbers, the z-dependence of angular momentum in both electrically driven and Taylor-Couette flows is very well approximated by (2.46).

2.3.3 Radial profile of angular momentum

For large Hartmann numbers ($\mathrm{Ha} \gg 1$), the angular momentum of electrically driven fluid in an annular channel is well approximated by the expression

$$u(r, z) = u_0(r) \frac{\cosh \mathrm{Ha} - \cosh(\mathrm{Ha}\, z)}{\sinh \mathrm{Ha}}, \tag{2.48}$$

which takes into account the presence of the Hartmann layers in the flow and assumes some radial dependence $u_0(r)$ of the angular momentum in the core region. The approximation (2.48) is verified by the following analysis and numerical simulations.

In order to find the equation which governs the radial profile of the angular momentum $u_0(r)$, we apply the method described in [65]. It is based on averaging

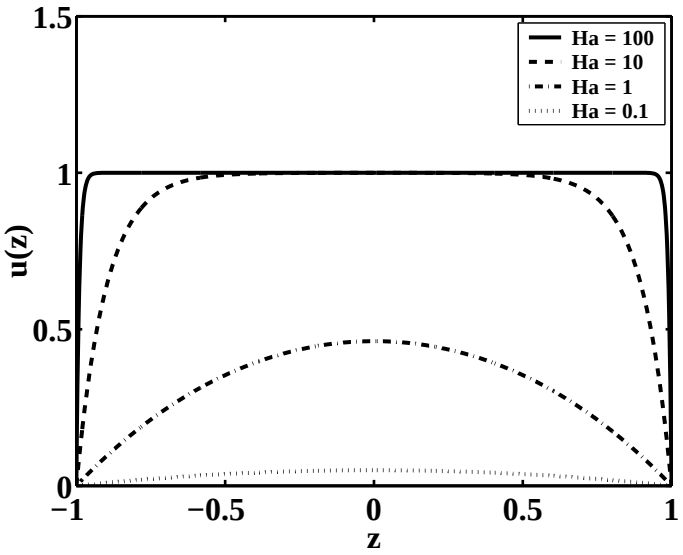

Figure 2.2: Profile of normalized angular momentum (2.46) at different values of the Hartmann number.

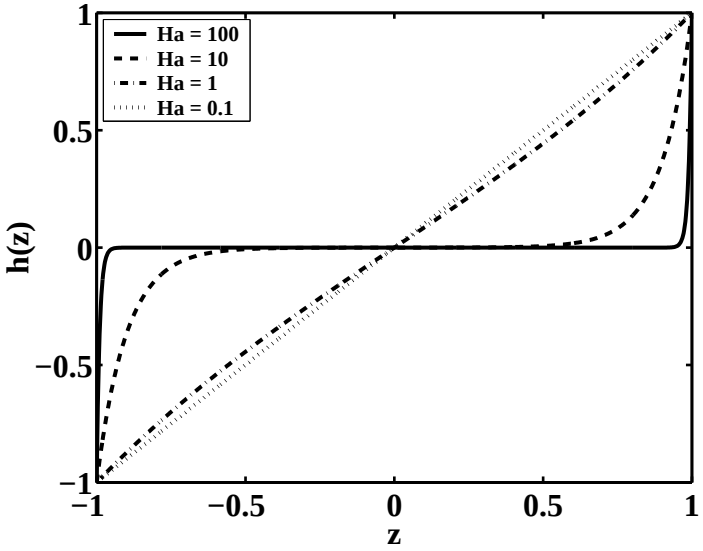

Figure 2.3: Profile of normalized poloidal stream function for the current density (2.47) at different values of the Hartmann number.

the equation (2.7) along the magnetic field lines, that is in the z-direction. Integrating equation (2.7) from $z = -1$ to $z = 1$, we arrive at

$$\frac{\partial^2 u_0}{\partial r^2} - \frac{1}{r}\frac{\partial u_0}{\partial r} - \mathrm{Ha} u_0 + \mathrm{Ha} - \frac{\mathrm{Re}}{2r}\frac{\partial}{\partial r}\int_{-1}^{1} w(r,z)\frac{\partial u(r,z)}{\partial z}dz = 0, \tag{2.49}$$

where we used boundary conditions for the poloidal current function h (2.41) and the fact that

$$\int_{-1}^{1} u(r,z)dz = 2u_0(r) + O\left(\frac{1}{\mathrm{Ha}}\right). \tag{2.50}$$

The integral in the last term of equation (2.49) can be calculated analytically if the explicit expression for the stream functions $w(r,z)$ is known.

The expression for $w(r,z)$ follows from equation (2.9). Prior to solving it, we make several simplifying assumptions. First, we neglect the radial derivatives in operator Δ^*, assuming that the function $w(r,z)$ changes more rapidly in the z-direction due to the presence of the small scales associated with the Hartmann layers. Second, we neglect the terms nonlinear in $w(r,z)$, which is valid if the inertial effects are small, see (2.56). Under these assumptions, equation (2.9) is reduced to

$$0 = \frac{\partial^4 w}{\partial z^4} - \mathrm{Ha}^2\frac{\partial^2 w}{\partial z^2} - \mathrm{Re}\,\frac{1}{r^2}\frac{\partial u^2}{\partial z}. \tag{2.51}$$

Substituting $u(r,z)$ from (2.48), we find the solution to this equation satisfying the boundary conditions (2.42) and (2.43)

$$\begin{aligned} w(r,z) &= \frac{\mathrm{Re}\,u_0^2(r)}{r^2\mathrm{Ha}^2\sinh^2\mathrm{Ha}}\Bigg[z + \sinh\mathrm{Ha}\,\sinh\mathrm{Ha}\,z - z\cosh\mathrm{Ha}\,\cosh\mathrm{Ha}\,z + \\ &+ \frac{\sinh\mathrm{Ha}\,z(\cosh\mathrm{Ha}\,z - \cosh\mathrm{Ha})}{6\mathrm{Ha}} + \frac{5\sinh^2\mathrm{Ha}(\sinh\mathrm{Ha}\,z - z\sinh\mathrm{Ha})}{6(\mathrm{Ha}\cosh\mathrm{Ha} - \sinh\mathrm{Ha})}\Bigg]. \end{aligned} \tag{2.52}$$

In order to give an idea of the magnitude of the poloidal circulation described by the function $w(r,z)$, we calculate the normalized radial velocity at $z = 0$:

$$v_r(r)|_{z=0} = -\frac{1}{r}\frac{\partial w}{\partial z}\bigg|_{z=0} = \frac{5\mathrm{Re}u_0^2(r)}{6r^3\mathrm{Ha}^3} + O\left(\frac{\mathrm{Re}}{\mathrm{Ha}^4}\right). \tag{2.53}$$

The radial flow at the midplane of the channel is always directed outward (from the inner wall to the outer).

We are now able to calculate the integral in equation (2.49). From (2.48) and (2.52), it follows that

$$\int_{-1}^{1} w(r,z)\frac{\partial u(r,z)}{\partial z}dz = \frac{7u_0^3(r)\mathrm{Re}}{18r^2\mathrm{Ha}^3} + O\left(\frac{\mathrm{Re}}{\mathrm{Ha}^4}\right). \tag{2.54}$$

Substituting (2.54) into (2.49), we have:

$$\frac{\partial^2 u_0}{\partial r^2} - \frac{1}{r}\frac{\partial u_0}{\partial r} - \mathrm{Ha}u_0 + \mathrm{Ha} - \frac{7\mathrm{Re}^2}{36r\mathrm{Ha}^3}\frac{\partial}{\partial r}\left(\frac{u_0^3}{r^2}\right) = 0. \tag{2.55}$$

An analogous equation was obtained in paper [65]. This equation determines the radial profile of the angular momentum of the fluid rotating in an annular channel. It has a clear physical meaning. The first two terms in the equation are viscous forces due to the radial dependence of the angular momentum and the third term is the viscous force in the Hartmann layers. The fourth term is the Ampere force (electrical drive) which is proportional to the total current flowing through the channel. The last nonlinear term is the inertia force (the coupling between the azimuthal rotation and the poloidal circulation of the fluid).

Depending on the comparative values of the inertia and Ampere forces, two flow regimes are realized. Simple estimates show that the inertia in equation (2.55) can be neglected if

$$\mathrm{Re} \ll \mathrm{Ha}^2\left(\frac{R_1}{H}\right)^2. \tag{2.56}$$

This is the so-called *inertialess* approximation. In this regime viscous forces near the channel walls are balanced by the Ampere force. The case of opposite inequality corresponds to the *inertial* flow with the viscosity balanced by the inertia. In the subsequent consideration, we find the analytical solutions to equation (2.55) for these two regimes.

2.3.4 Inertialess regime, $\mathbf{Re} = 0$

If the inertia force is small compared to the Ampere force the nonlinear term in the equation (2.55) can be neglected:

$$\frac{\partial^2 u_0}{\partial r^2} - \frac{1}{r}\frac{\partial u_0}{\partial r} - \mathrm{Ha}u_0 + \mathrm{Ha} = 0. \tag{2.57}$$

This ordinary differential equation possesses an exact solution which is expressed in terms of the modified Bessel function of the first kind:

$$u_0(r) = 1 - \frac{r}{I_1(\sqrt{\mathrm{Ha}}(r_2 - r_1))}\left[\frac{1}{r_1} I_1(\sqrt{\mathrm{Ha}}(r_2 - r)) + \frac{1}{r_2} I_1(\sqrt{\mathrm{Ha}}(r - r_1))\right]. \quad (2.58)$$

Despite its complex appearance, this dependence is quite simple. To demonstrate this, we consider the case of a small gap between the side walls ($r_2 - r_1 \ll r_{1,2}$), then the expression (2.58) becomes

$$u_0(x) = 1 - \frac{\cosh[xl\sqrt{\mathrm{Ha}}]}{\cosh[l\sqrt{\mathrm{Ha}}]}, \quad (2.59)$$

where $l = (R_2 - R_1)/H$ is a ratio between the width of the channel and its height (aspect ratio) and $x = (2R - R_1 - R_2)/(R_2 - R_1) \in [-1; 1]$ is a normalized distance from the center of the channel. We note that the dependence (2.59) describes the side boundary layers of thickness $O(H/\sqrt{\mathrm{Ha}})$. If $l\sqrt{\mathrm{Ha}} \gg 1$, i.e.,

$$R_2 - R_1 \gg \frac{H}{\sqrt{\mathrm{Ha}}}, \quad (2.60)$$

then these layers are small compared to the channel width and the normalized angular momentum is close to 1 in the most part of the flow. In this case, the angular velocity of electrically driven flow can be approximated as (in dimensional units)

$$\Omega(R) = \frac{M_0}{R^2}, \quad (2.61)$$

where M_0 is defined in (2.39). Such rotation is stable in hydrodynamics according to Rayleigh criterion (1.3) but can be unstable with respect to magnetorotational instability (1.3).

For Re = 0, Ha = 30, the calculated angular momentum profile $u(r, z)$ of electrically driven flow is presented in Fig. 2.4. As one can see, the normalized angular momentum is equal to 1 almost entirely in the cross-section of the channel with the exception of boundary layers near the walls. This result is in a good agreement with (2.48) and (2.58); the comparison with the latter is plotted in Fig. 2.5.

The calculated poloidal current stream function $h(r, z)$ is shown in Fig. 2.6. The electric current lines (contours of the function $h(r, z)$) are plotted in Fig. 2.7. As mentioned above, at large Ha almost all the current in electrically driven fluid is expelled to the top and bottom walls and flows through the thin Hartmann layers.

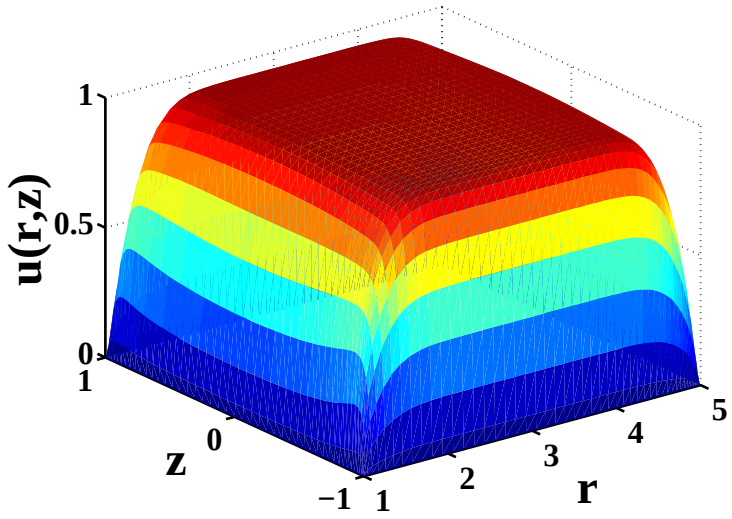

Figure 2.4: The profile of normalized angular momentum $u(r, z)$ in the cross-section of the channel for electrically driven flow, Ha $= 30$, Re $= 0$.

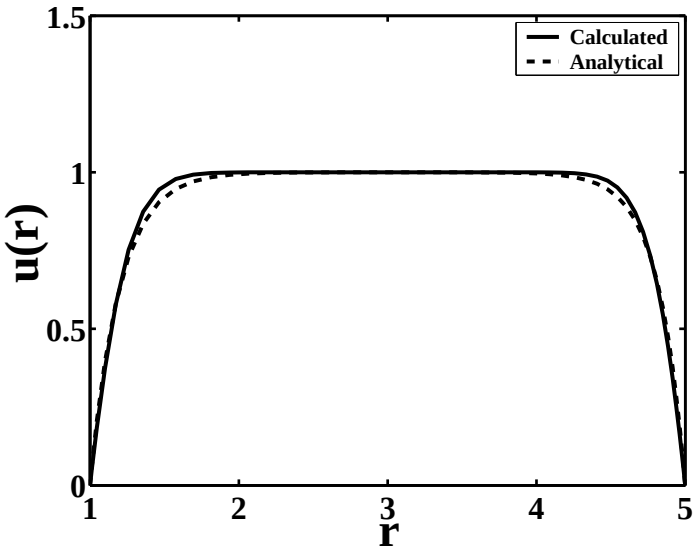

Figure 2.5: The radial dependence of normalized angular momentum $u(r, z)$ at the midplane of the channel at $z = 0$ in the electrically driven flow, Ha $= 30$, Re $= 0$. The solid line corresponds to the numerical simulation while the dashed line corresponds to the analytical expression (2.58).

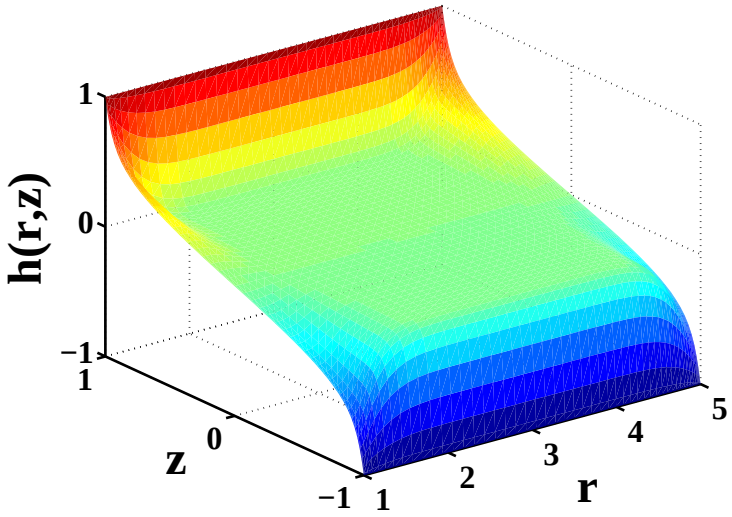

Figure 2.6: The profile of normalized current function $h(r, z)$ in the cross-section of the channel for electrically driven flow, Ha = 30, Re = 0.

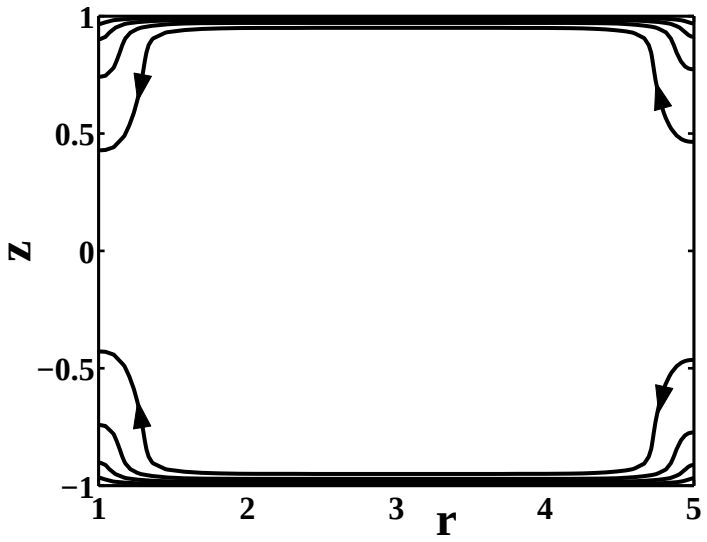

Figure 2.7: The electric current lines (contours of $h(r, z)$) in the cross-section of the channel for electrically driven flow, Ha = 30, Re = 0.

2.3.5 The effect of inertia, Re $\neq 0$

Now we consider the influence of inertia (the nonlinear term in equation (2.55)) on the radial profile of angular momentum $u_0(r)$. For simplicity, we solve equation (2.55) in the region near the inner side wall r_1. In this case, the boundary conditions for function $u_0(r)$ are

$$u_0(r_1) = 0, \quad u_0(\infty) = 1. \tag{2.62}$$

We look for a solution in the form of the expansion:

$$u_0(r) = a_0(r) + a_1(r)e^{-Q(r)/\varepsilon} + a_2(r)e^{-2Q(r)/\varepsilon} + \dots, \tag{2.63}$$

where $Q(r)$ is nonnegative monotonic function of r and each $a_j(r)$ is developed in the asymptotic series of a small parameter ε:

$$a_j(r) = a_j^{(0)}(r) + \varepsilon a_j^{(1)}(r) + \varepsilon^2 a_j^{(2)}(r) + \dots, \tag{2.64}$$

so the method of multiple scales can be used (see, for example, [92]), with $Q(r)/\varepsilon$ being a fast variable. We will be interested only in the first few terms of the expansion (2.63) since the main dependence of the function $u_0(r)$ is related to them (the other terms are decreasing rapidly with r).

The leading order approximation of the angular momentum radial profile is

$$u_0(r) = 1 - \exp\left[-\int_{r_1}^{r} K(r')dr' \right], \tag{2.65}$$

where $K(r)$ satisfies the following equation:

$$K^2 + \frac{7\mathrm{Re}^2}{12r^3\mathrm{Ha}^3}\, K - \mathrm{Ha} = 0. \tag{2.66}$$

The nonnegative root of this quadratic equation is:

$$K(r) = \frac{1}{2}(-C(r) + \sqrt{C(r)^2 + 4\mathrm{Ha}}), \tag{2.67}$$

where $C(r) = 7\mathrm{Re}^2/12r^3\mathrm{Ha}^3$.

One can see that the solution (2.65) corresponds to the boundary layer near the inner side wall, where the angular momentum grows from 0 to 1. The thickness of

this layer $\delta_1 \sim 1/K(r_1)$ is determined by the parameters of the flow, as should be expected. When inertia is small, i.e., $C^2 \ll 4\mathrm{Ha}$, expression (2.67) results in

$$\delta_1 \sim \frac{1}{\sqrt{\mathrm{Ha}}}, \tag{2.68}$$

which is in agreement with (2.59). In the case of the reverse inequality, $C^2 \gg 4\mathrm{Ha}$, the thickness of the boundary layer is estimated by

$$\delta_1 \sim \frac{C(r_1)}{\mathrm{Ha}} \sim \frac{\mathrm{Re}^2}{r_1^3 \mathrm{Ha}^4}. \tag{2.69}$$

Thus, if inertia is large, the inner boundary layer penetrates the bulk of the flow. As a result, the rotation profile is changed significantly and the conditions for MRI excitation may not be met.

We note that the second (negative) root of the equation (2.66) describes the boundary layer near the outer side wall. Its thickness is

$$\delta_2 \sim \frac{1}{\sqrt{\mathrm{Ha}}}, \tag{2.70}$$

if the magnetic field prevails over the inertia, and

$$\delta_2 \sim \frac{1}{C(r_2)} \sim \frac{r_2^3 \mathrm{Ha}^3}{\mathrm{Re}^2} \tag{2.71}$$

in the opposite case. Therefore, the outer boundary layer decreases with growth of Reynolds number.

The calculated equilibrium structure of electrically driven flow in inertial regime (Ha = 30, Re = 4000) is shown in Figs. 2.8–2.12. We note that the angular momentum profile (Fig. 2.8) and the distribution of electrical current (Figs. 2.9 and 2.10) are different from corresponding characteristics at Re = 0 (Figs. 2.4–2.7). The typical feature of the flow in inertial regime is the development of two poloidal circulation cells (Figs. 2.11 and 2.12). Their presence leads to a coupling of the azimuthal velocity component with radial and axial ones (inertial effects), which results in a change of the angular momentum.

The radial profiles of the angular momentum u for different values of Reynolds number are presented in Fig. 2.13. As follows from this figure, with growth of Re,

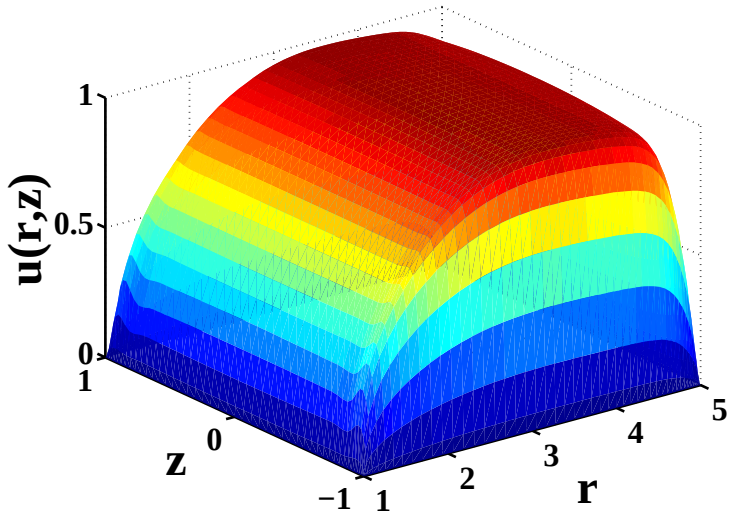

Figure 2.8: The profile of normalized angular momentum $u(r, z)$ in the cross-section of the channel for electrically driven flow, Ha = 30, Re = 4000.

the boundary layer increases near the inner wall of the channel and decreases near the outer wall. Such behavior of the side boundary layers is described by formulas (2.69) and (2.71).

Our numerical simulations show that the dependence of the angular momentum in the Hartmann layers near the top and bottom walls of the channel remains practically the same for the wide range of Reynolds numbers (Fig. 2.14) and corresponds to the Hartmann flow profile (2.46). This validates the use of representation (2.48).

2.4 Taylor-Couette flow

In this section, we perform a theoretical study of a liquid metal Taylor-Couette flow between two coaxial rotating cylinders (Fig. 1.1) placed in an axial magnetic field. In order to demonstrate characteristic features of Taylor-Couette flow at the different Reynolds and Hartmann numbers we choose the following dimensions of the channel: normalized radii of inner and outer cylinders are $r_1 = R_1/L = 1$ and $r_2 = R_2/L = 1.5$, respectively, where $H = 2L$ is the height of the channel.

Our main results are obtained for the configuration where both cylinders are

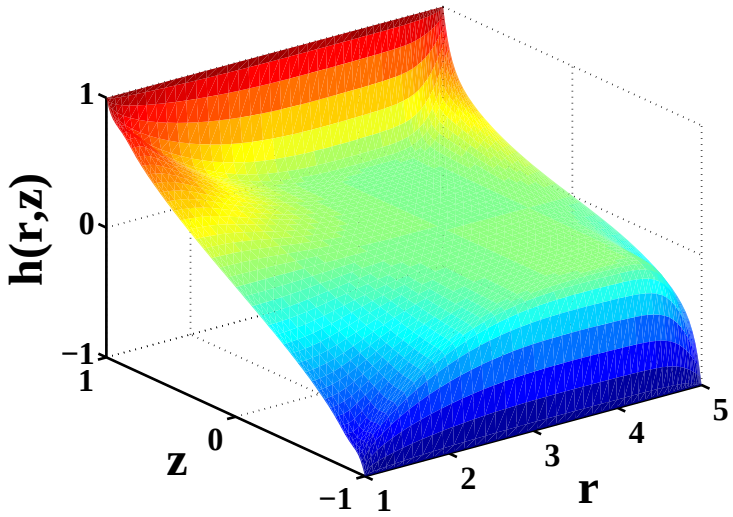

Figure 2.9: The profile of normalized current function $h(r, z)$ in the cross-section of the channel for electrically driven flow, Ha = 30, Re = 4000.

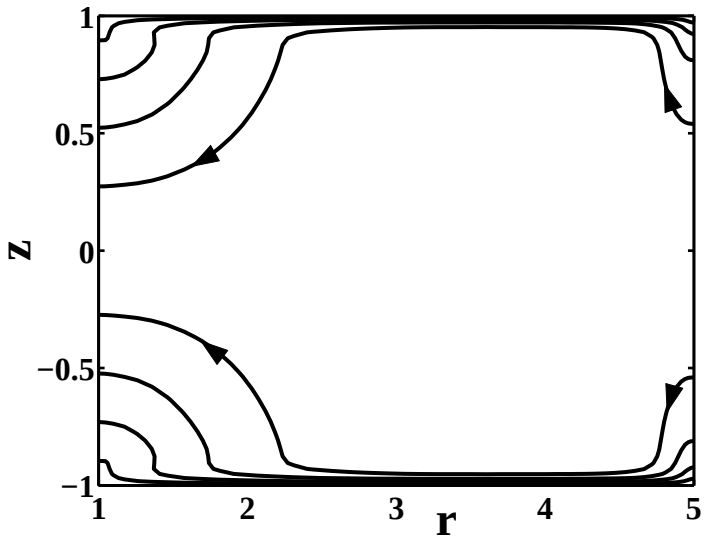

Figure 2.10: The electric current lines (contours of $h(r, z)$) in the cross-section of the channel for electrically driven flow, Ha = 30, Re = 4000.

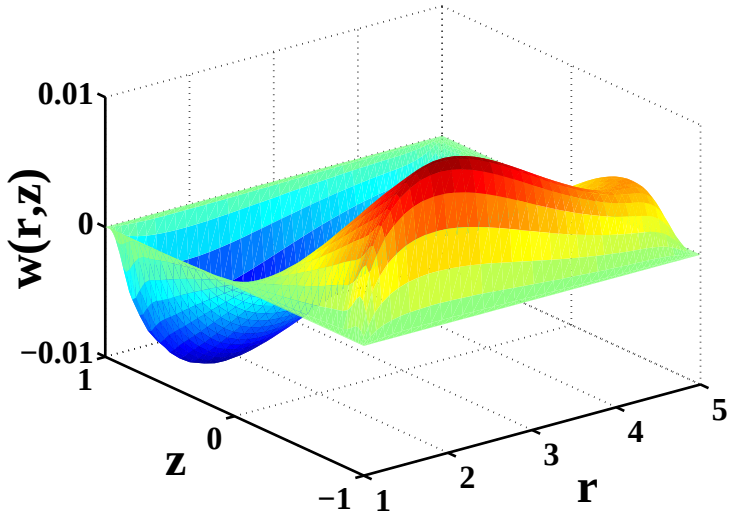

Figure 2.11: The profile of normalized poloidal stream function $w(r, z)$ in the cross-section of the channel for electrically driven flow, Ha = 30, Re = 4000.

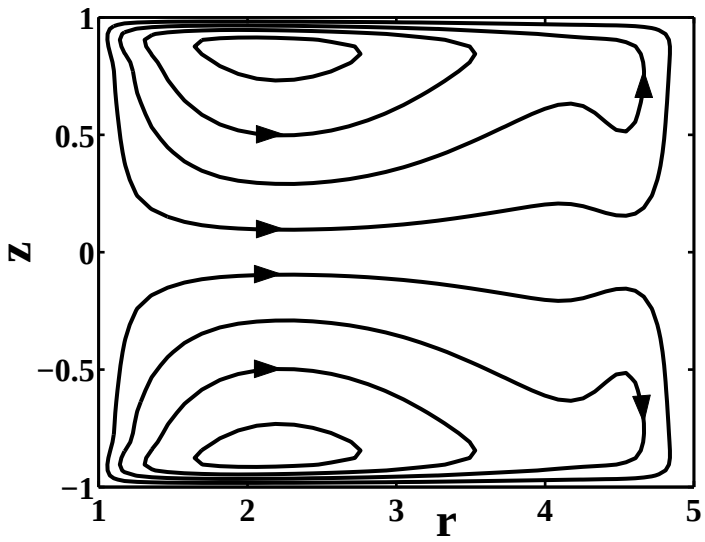

Figure 2.12: The poloidal flow streamlines (contours of $w(r, z)$) in the cross-section of the channel for electrically driven flow, Ha = 30, Re = 4000.

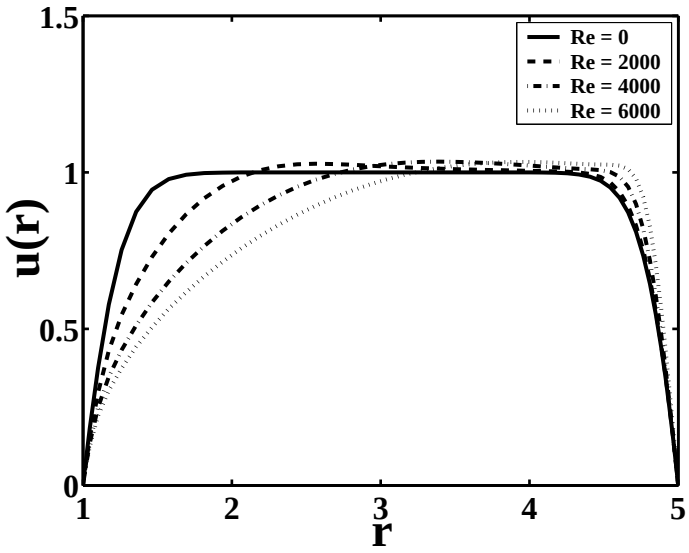

Figure 2.13: The radial profile of the normalized angular momentum $u(r, z)$ at the midplane of the channel at $z = 0$ for different values of Reynolds number Re in the electrically driven flow, Ha = 30.

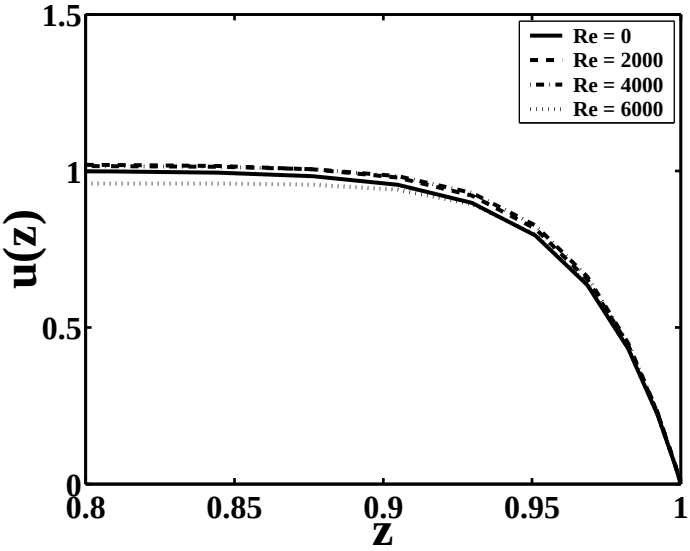

Figure 2.14: The dependence of the normalized angular momentum $u(r, z)$ in the Hartmann layer at $r = 3$ for different values of Reynolds number Re in the electrically driven flow, Ha = 30.

rotating with the same angular momentum, i.e., $\Omega_1 R_1^2 = \Omega_2 R_2^2 = M_0$; however, these results are quite general. The choice of this configuration was dictated by two reasons. First, such flow is hydrodynamically stable for any values of M_0 (Rayleigh criterion (1.1)), i.e., it does not admit transition to more complex states [93] and its analysis is simplified. Second, such configuration allows comparison of Taylor-Couette flow with the electrically driven flow (which is, roughly speaking, a flow with constant angular momentum, see (2.61)).

2.4.1 Boundary conditions

In the case of Taylor-Couette flow (Fig. 2.15), the boundary conditions for velocity components are analogous to (2.32) and (2.33):

$$u|_{z=\pm 1} = 0, \qquad u|_{r=(r_1,r_2)} = u_{1,2}, \tag{2.72}$$

$$\nabla w|_{z=\pm 1} = 0, \quad \nabla w|_{r=(r_1,r_2)} = 0, \tag{2.73}$$

where u_1 and u_2 are normalized angular momenta corresponding to rotating inner and outer walls, i.e.,

$$u_1 = \frac{M_1}{M_0} = \frac{\Omega_1 R_1^2}{M_0}, \quad u_2 = \frac{M_2}{M_0} = \frac{\Omega_2 R_2^2}{M_0}. \tag{2.74}$$

Here M_0 is the characteristic angular momentum. It can be chosen to be equal to either M_1 or M_2, whichever is not zero. Once M_0 is fixed, the typical value of the velocity in the system is determined as $V = 2M_0/H$.

Assuming all channel walls insulating and using (2.18), one obtains the boundary conditions for the normalized current function $h(r, z)$

$$\left.\frac{\partial h}{\partial r}\right|_{z=\pm 1} = 0, \quad \left.\frac{\partial h}{\partial z}\right|_{r=(r_1,r_2)} = 0. \tag{2.75}$$

These conditions can be integrated to give

$$h|_\Gamma = 0,$$

where the oddness of $h(r, z)$ is taken into account.

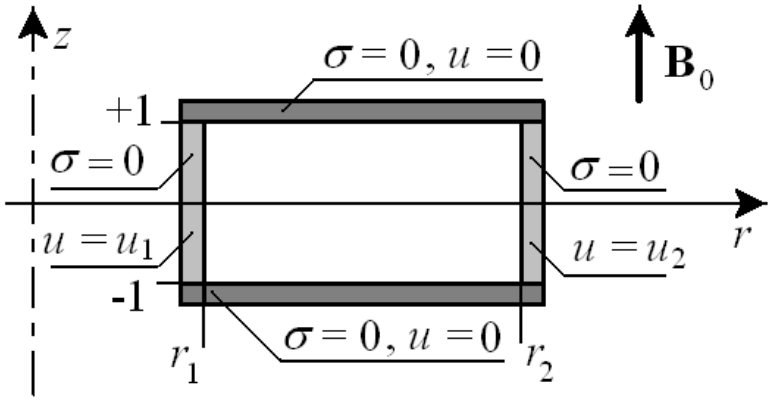

Figure 2.15: Cross section of the channel in the case of Taylor-Couette flow. All channel walls are insulators (conductivity $\sigma = 0$). Side walls are rotating with angular momenta u_1 and u_2 respectively, top and bottom walls are stationary ($u = 0$).

Finally, the boundary conditions for the system (2.7)-(2.9) in the case of Taylor-Couette flow are

$$u|_{z=\pm 1} = 0, \qquad u|_{r=(r_1,r_2)} = u_{1,2}, \tag{2.76}$$

$$h|_{z=\pm 1} = 0, \qquad h|_{r=(r_1,r_2)} = 0, \tag{2.77}$$

$$w|_{z=\pm 1} = 0, \qquad w|_{r=(r_1,r_2)} = 0, \tag{2.78}$$

$$\left.\frac{\partial w}{\partial z}\right|_{z=\pm 1} = 0, \qquad \left.\frac{\partial w}{\partial r}\right|_{r=(r_1,r_2)} = 0. \tag{2.79}$$

2.4.2 Boundary layers near end-plates

It is well-known that Taylor-Couette flow is strongly affected by the boundary layers developed near the top and bottom end-plates [52, 94, 95]. The simple estimates for the thickness of these boundary layers can be obtained from the equation of the force balance (1.16). In the case of steady end-plates there are three basic boundary layers.

Viscous layer

If the viscous forces are much larger than both the inertia and Ampere forces then the force-balance equation is reduced to

$$\nabla^2 \mathbf{V}_e = 0. \tag{2.80}$$

The boundary layer in this case is referred to as *viscous layer* and the corresponding flow is *viscous flow*. From equation (2.80) it is obvious that the thickness of the viscous layers near the end-plates is determined by a characteristic spatial scale in r-direction, which is a gap between cylindrical walls, i.e.,

$$d_{visc} \approx R_2 - R_1,$$

or, in non-dimensional terms (unit of length is $L = H/2$, where H is the channel height):

$$\delta_{visc} \approx r_2 - r_1. \tag{2.81}$$

Ekman layer

Ekman layers are developed near the steady end-plates if the Ampere force is negligible and the viscosity is balanced by the inertia:

$$\nu \nabla^2 \mathbf{V}_e = (\mathbf{V}_e \cdot \nabla)\mathbf{V}_e. \tag{2.82}$$

Such regime is referred to as *inertial flow*. In this case, the thickness of the boundary layer is

$$d_{\mathrm{Ek}} \approx \sqrt{\frac{\nu}{\Omega}},$$

or, in non-dimensional terms:

$$\delta_{\mathrm{Ek}} \approx \frac{r_1}{\sqrt{\mathrm{Re}}}. \tag{2.83}$$

Hartmann layer

When the magnetic field is sufficiently large, the Ampere force can overcome the inertia. In this case the force balance is

$$\rho \nu \nabla^2 \mathbf{V}_e = -\frac{1}{c}\, \mathbf{J}_e \times \mathbf{B}_e. \tag{2.84}$$

Such regime is referred to as *magnetized* or *Hartmann flow*. In this flow, the *Hartmann layers* are developed near the steady insulating end-plates, their thickness is

$$d_{\mathrm{Ha}} \approx \frac{\sqrt{\rho\nu\eta}}{B_0},$$

or, in non-dimensional terms:

$$\delta_{\mathrm{Ha}} \approx \frac{1}{\mathrm{Ha}}. \tag{2.85}$$

For arbitrary values of the Reynolds and Hartmann numbers the thickness of the boundary layers near the end-plates can be approximated as

$$\frac{1}{\delta} \approx \left(\frac{1}{\delta_{visc}} + \frac{1}{\delta_{\mathrm{Ek}}} + \frac{1}{\delta_{\mathrm{Ha}}}\right) \approx \left(\frac{1}{r_2 - r_1} + \frac{\sqrt{\mathrm{Re}}}{r_1} + \mathrm{Ha}\right). \tag{2.86}$$

Therefore, depending on the relative values of the Reynolds and Hartmann numbers and geometrical parameters of the channel three different regimes of Taylor-Couette flow can be realized. Below, we consider them in more detail.

2.4.3 Viscous regime

In the viscous regime, we can assume $\mathrm{Ha} = 0$ and $\mathrm{Re} = 0$, so the system (2.7)-(2.9) is reduced to one equation

$$\frac{\partial^2 u}{\partial r^2} - \frac{1}{r}\frac{\partial u}{\partial r} + \frac{\partial^2 u}{\partial z^2} = 0. \tag{2.87}$$

Strictly speaking, the case for $\mathrm{Re} = 0$ presumes no rotation at all; it is physically meaningful to consider it only as the limit of small Reynolds numbers, $\mathrm{Re} \to 0$. Equation (2.87) with boundary conditions (2.76) can be solved exactly in terms of infinite series. In a small gap approximation ($r_2 - r_2 \ll r_{1,2}$), the solution has a form:

$$\begin{aligned} u(r,z) &= \frac{u_1 r_2^2 - u_2 r_1^2}{r_2^2 - r_1^2} + \frac{u_2 - u_1}{r_2^2 - r_1^2}\, r^2 + \sum_{j=1}^{\infty} a_j \sin\left[2jk_r\left(r - \frac{r_1 + r_2}{2}\right)\right] \frac{\cosh[2jk_r z]}{\cosh[2jk_r]} \\ &+ \sum_{j=0}^{\infty} b_j \cos\left[(2j+1)k_r\left(r - \frac{r_1 + r_2}{2}\right)\right] \frac{\cosh[(2j+1)k_r z]}{\cosh[(2j+1)k_r]}, \end{aligned} \tag{2.88}$$

where

$$k_r = \frac{\pi}{r_2 - r_1},$$

and the coefficients a_j and b_j are

$$a_j = \frac{(-1)^j(u_2 - u_1)}{\pi j}, \tag{2.89}$$

$$b_j = -\frac{2(-1)^j(u_1 + u_2)}{\pi(2j+1)} + \frac{8(-1)^j(u_2 - u_1)(r_2 - r_1)}{\pi^3(2j+1)^3(r_1 + r_2)}. \tag{2.90}$$

The expression (2.88) is simplified if we consider a rotation with $u_1 = u_2 = 1$. In this case, the z-profile of normalized angular momentum in the middle section of the channel (at $r = (r_1 + r_2)/2$) can be approximated as

$$u(r, z) \approx 1 - \frac{\cosh[k_r z]}{\cosh k_r}. \tag{2.91}$$

The numerical solution to the equation (2.87) for $u_1 = u_2 = 1$ is shown in Fig. 2.16. As one can see, the normalized angular momentum is equal to 1 in the central part of the cross-section of the channel and decreases to 0 in the viscous boundary layers near the end-plates. This result is in a good agreement with (2.91); the comparison is shown in Fig. 2.17. Thus, we conclude that the viscous Taylor-Couette flow is appropriate for MRI experiments if the boundary layers are much less than the hight of the channel or, in other words, if

$$R_2 - R_1 \ll H. \tag{2.92}$$

2.4.4 Inertial regime

In the inertial regime, we can neglect the magnetic field, so the system (2.7)-(2.9) becomes

$$0 = \Delta^* u + \frac{\mathrm{Re}}{r}[u, w], \tag{2.93}$$

$$0 = \Delta^*\Delta^* w - \mathrm{Re}\left(r\left[w, \frac{\Delta^* w}{r^2}\right] + \frac{1}{r^2}\frac{\partial u^2}{\partial z}\right). \tag{2.94}$$

The analytical treatment of such system is quite difficult since the equations are nonlinear. In this section we discuss only the numerical results for the case $u_1 = u_2 = 1$.

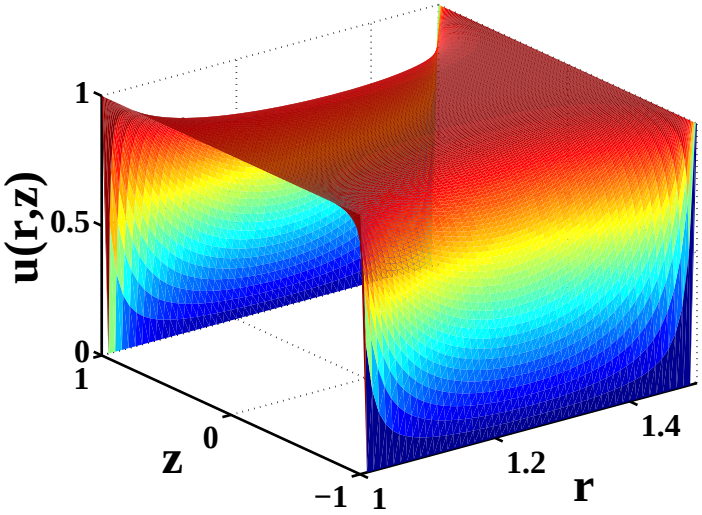

Figure 2.16: The profile of normalized angular momentum $u(r, z)$ in the cross-section of the channel for Taylor-Couette flow, Ha $= 0$, Re $= 0$.

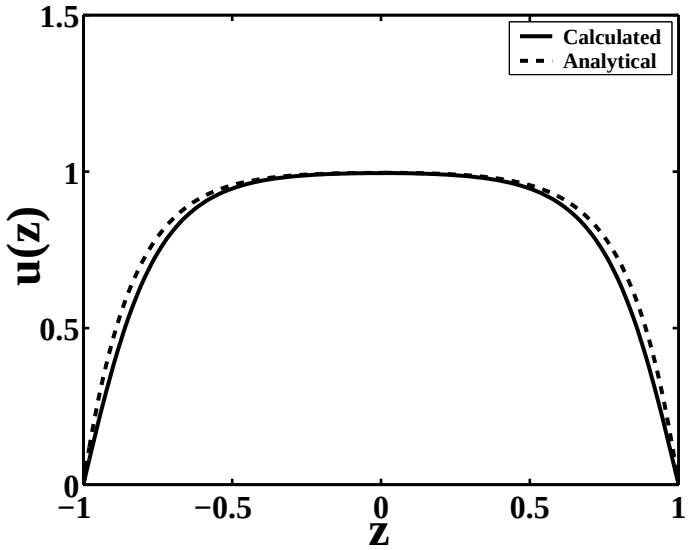

Figure 2.17: The z-dependence of normalized angular momentum $u(r, z)$ at the middle section of the channel at $r = 1.25$ in Taylor-Couette flow, Ha $= 0$, Re $= 0$. The solid line corresponds to the numerical simulation while the dashed line corresponds to the analytical expression (2.91).

The equilibrium structure of the inertial Taylor-Couette flow is presented in Figs. 2.18-2.21. One of the typical features of high-Re Taylor-Couette flow is the existence of the jet-like formation near the midplane (at $z = 0$) of the azimuthal momentum profile u (Figs. 2.18 and 2.19). It is undoubtedly the counterpart of the strong radial outflow which is seen in Fig. 2.21. Such jet-like structures in the flow can be explained by the presence of the steady end-caps [46, 52].

These results suggest that the inertial regime of Taylor-Couette flow is of little use in the MRI experiments. The instabilities one obtains in this regime (even with magnetic field) will most probably be the familiar Kelvin-Helmholtz instabilities of the jet-like structures, rather than the magneto-rotational instability. At best, one might hope to obtain the MRI superimposed on these Kelvin-Helmholtz modes. Any subsequent interpretation of experimental results will be quite complicated.

2.4.5 Magnetized regime

Magnetized regime of Taylor-Couette flow is formally described by the system (2.7)-(2.9) in the limit of small Reynolds numbers, $\mathrm{Re} \to 0$:

$$0 = \Delta^* u + \mathrm{Ha}\frac{\partial h}{\partial z}, \tag{2.95}$$

$$0 = \Delta^* h + \mathrm{Ha}\frac{\partial u}{\partial z}. \tag{2.96}$$

Similar to the case of electrically driven flow we can represent the normalized angular momentum $u(r, z)$ in a form (2.48)

$$u(r, z) = u_0(r)\frac{\cosh \mathrm{Ha} - \cosh(\mathrm{Ha}\, z)}{\sinh \mathrm{Ha}}.$$

Then we use the method of averaging along the magnetic field lines to find the radial profile $u_0(r)$. As shown in Section 2.3.3, this method results in equation (2.57) which for Taylor-Couette flow reads:

$$\frac{\partial^2 u_0}{\partial r^2} - \frac{1}{r}\frac{\partial u_0}{\partial r} - \mathrm{Ha} u_0 = 0. \tag{2.97}$$

The only difference between this equation and equation (2.57) is the absent in the former of the term related to the electrical current drive. As a result, the approximate

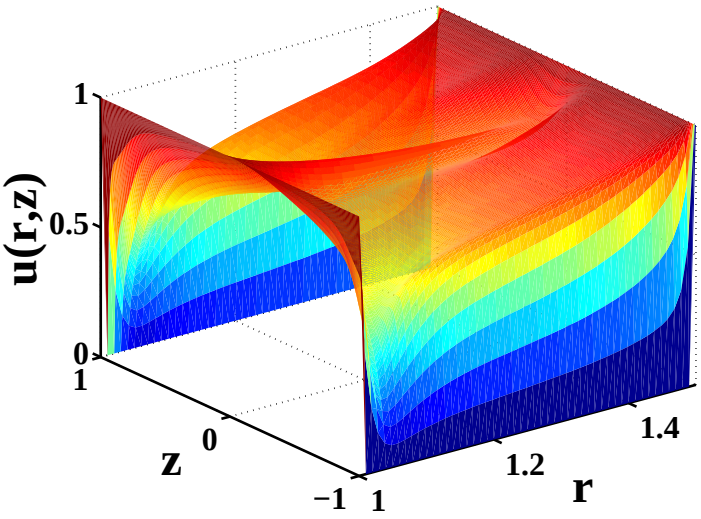

Figure 2.18: The profile of normalized angular momentum $u(r, z)$ in the cross-section of the channel for Taylor-Couette flow, Ha $= 0$, Re $= 2000$.

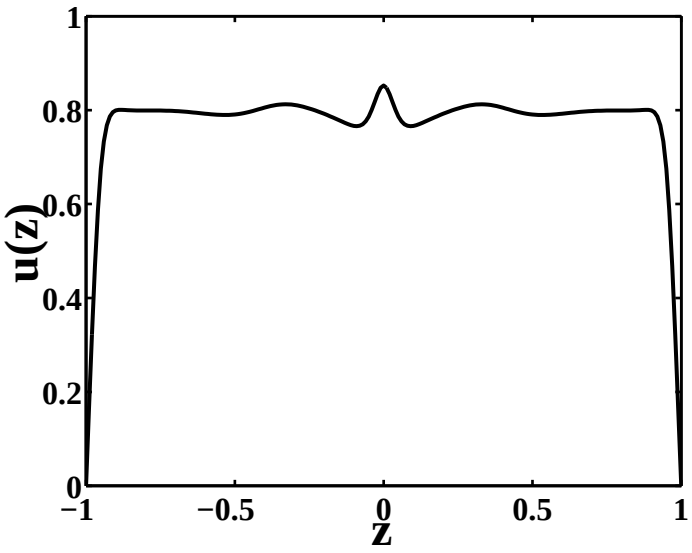

Figure 2.19: The z-dependence of normalized angular momentum $u(r, z)$ at the middle section of the channel at $r = 1.25$ in Taylor-Couette flow, Ha $= 0$, Re $= 2000$.

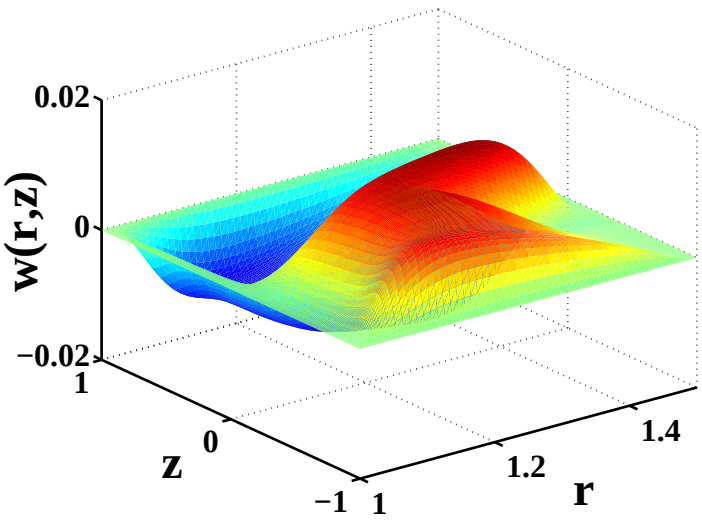

Figure 2.20: The profile of normalized poloidal stream function $w(r, z)$ in the cross-section of the channel for Taylor-Couette flow, Ha = 0, Re = 2000.

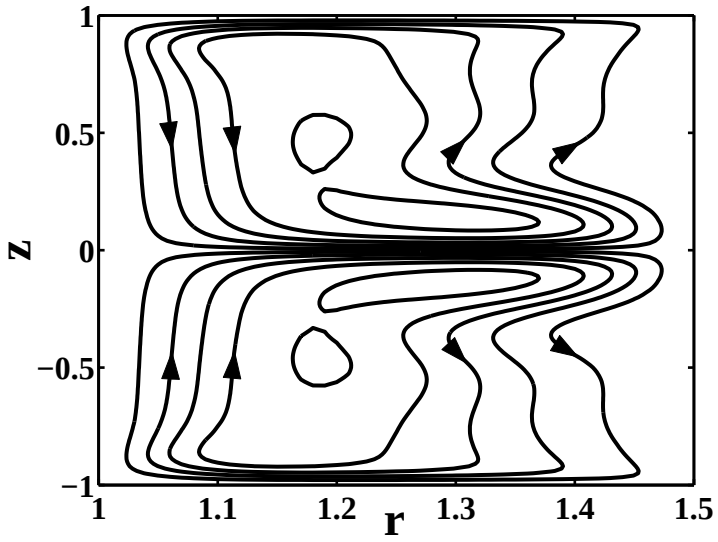

Figure 2.21: The poloidal flow streamlines (contours of $w(r, z)$) in the cross-section of the channel for Taylor-Couette flow, Ha = 0, Re = 2000.

solution to equation (2.97) satisfying the boundary conditions (2.76) can be written in a form analogous to (2.58):

$$u_0(r) = \frac{r}{I_1(\sqrt{\mathrm{Ha}}(r_2 - r_1))}\left[\frac{u_1}{r_1} I_1(\sqrt{\mathrm{Ha}}(r_2 - r)) + \frac{u_2}{r_2} I_1(\sqrt{\mathrm{Ha}}(r - r_1))\right]. \quad (2.98)$$

If we consider a small gap between the side walls of the channel and assume $u_1 = u_2 = 1$ then (2.98) becomes

$$u_0(x) = \frac{\cosh[xl\sqrt{\mathrm{Ha}}]}{\cosh[l\sqrt{\mathrm{Ha}}]}, \quad (2.99)$$

where $l = (R_2 - R_1)/H$ is an aspect ratio and $x = (2R - R_1 - R_2)/(R_2 - R_1) \in [-1; 1]$ is a normalized distance from the center of the channel. As follows from expression (2.99), the radial profile of angular momentum is close to constant when $l\sqrt{\mathrm{Ha}} \ll 1$, i.e.,

$$R_2 - R_1 \ll \frac{H}{\sqrt{\mathrm{Ha}}}. \quad (2.100)$$

Generally speaking, condition (2.100) has to be satisfied to validate the approximation of long cylinders for magnetized Taylor-Couette flow. In this case, the angular velocity of the fluid can be described by (in dimensional units)

$$\Omega(R) = \frac{M_2 - M_1}{R_2^2 - R_1^2} + \left(\frac{M_1 R_2^2 - M_2 R_1^2}{R_2^2 - R_1^2}\right)\frac{1}{R^2}, \quad (2.101)$$

where $M_1 = \Omega_1 R_1^2$, $M_2 = \Omega_2 R_2^2$ are angular momenta of the inner and outer walls, respectively.

For Ha = 50 and Re = 0, the angular momentum profile in the cross-section of the channel is shown in Fig. 2.22. It is almost homogeneous in the z-direction and has a parabolic radial dependence as predicted by (2.98). For comparison, the analytical and calculated radial profiles of u are plotted in Fig. 2.23. Figs. 2.24 and 2.25 show the configuration of poloidal electric current for this case.

The dependence of the angular momentum's z-profile on the Reynolds numbers is shown in Fig. 2.26. As one can see, the increase of Reynolds number results in a considerable change of the flow structure. In fact, when $\mathrm{Re} \gtrsim 1000$ the flow turns to inertial regime.

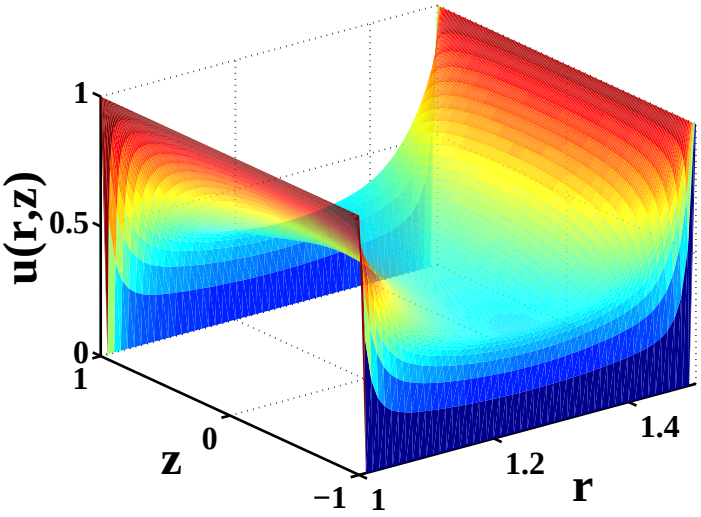

Figure 2.22: The profile of normalized angular momentum $u(r, z)$ in the cross-section of the channel for Taylor-Couette flow, Ha $= 50$, Re $= 0$.

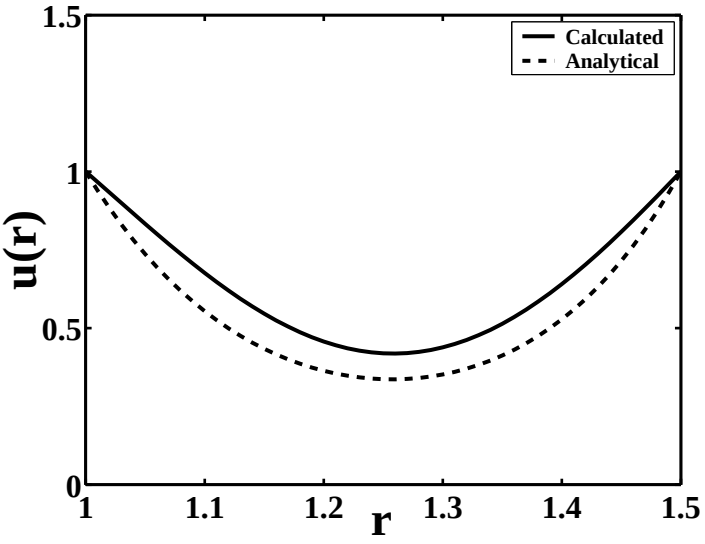

Figure 2.23: The radial dependence of normalized angular momentum $u(r, z)$ at the midplane of the channel at $z = 0$ in Taylor-Couette flow, Ha $= 50$, Re $= 0$. The solid line corresponds to the numerical simulation while the dashed line corresponds to the analytical expression (2.98).

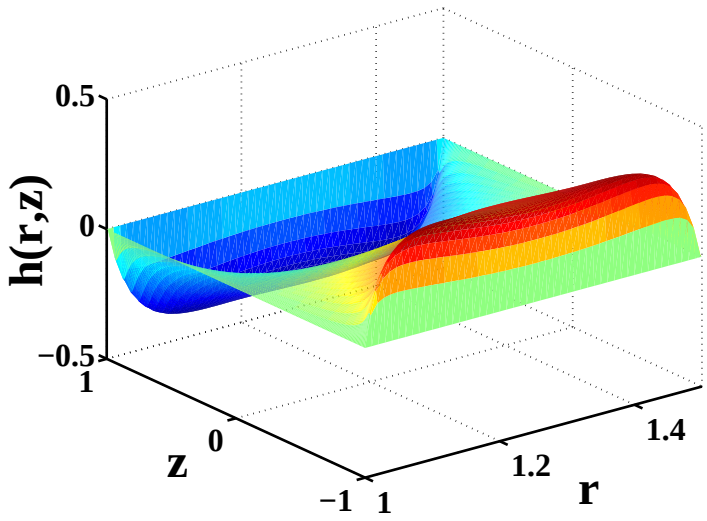

Figure 2.24: The profile of normalized current function $h(r, z)$ in the cross-section of the channel for Taylor-Couette flow, Ha $= 50$, Re $= 0$.

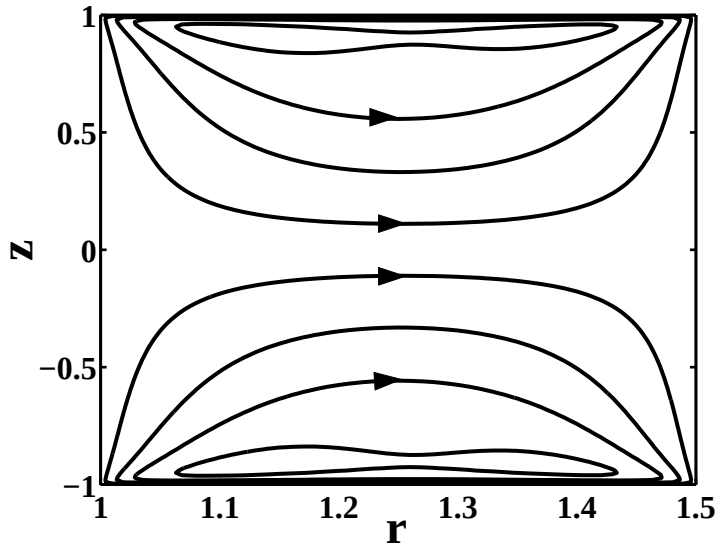

Figure 2.25: The electric current lines (contours of $h(r, z)$) in the cross-section of the channel for Taylor-Couette flow, Ha $= 50$, Re $= 0$.

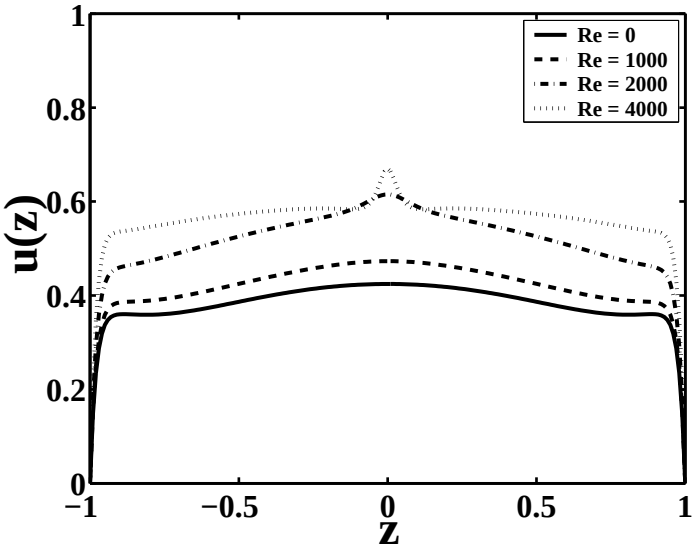

Figure 2.26: The z-dependence of the normalized angular momentum $u(r, z)$ at $r = 1.25$ for different values of Reynolds number Re in the Taylor-Couette flow, Ha $= 50$.

2.5 Conclusions

According to results of this chapter, both electrically driven and Taylor-Couette flows can be used as an initial background in MRI experiments, however, different conditions have to be satisfied in both cases to achieve the rotation profiles appropriate for MRI excitation. In the case of Taylor-Couette flow, the height of the channel should be much bigger than the gap between the side walls, i.e., $H \gg R_2 - R_1$ (2.100). For electrically driven flow, on the contrary, it is enough to have $H \lesssim R_2 - R_1$ (2.60).

The main advantage of Taylor-Couette flow is the possibility to change the rotation profile by applying different angular velocities to the side walls (2.101), while in electrically driven flow, the rotation profile is predetermined and one can change only its amplitude (2.61). Electrically driven flow is simpler from a technical point of view, since the corresponding experimental device does not contain moving parts.

As shown in our analysis, the inertial effects change the equilibrium flow structure considerably in both cases, so that the conditions for MRI excitation may not be met. These effects have to be reduced in any MRI experiment. From equation (2.55),

it follows that the inertia becomes negligible if

$$\mathrm{Re} \lesssim \mathrm{Ha}^2 \left(\frac{R_1}{H} \right)^2. \tag{2.102}$$

This inequality determines the range of "good" parameters for MRI experiment (see Figs. 2.27 and 2.28). For the parameters of the Obninsk MRI experiment (Table 2.1), inequality (2.102) is satisfied if $\mathrm{Re} \lesssim 10^4$ or, equivalently, if the total current passed through the channel is less than $I_0 \approx 10$ A.

In Chapters 3 and 4 we study the stability of the equilibrium flow with constant angular momentum (corresponding angular velocity is $\Omega(R) \propto 1/R^2$), which approximates the electrically driven flow when $\mathrm{Ha} \gg 1$ and conditions (2.60), (2.102) are satisfied.

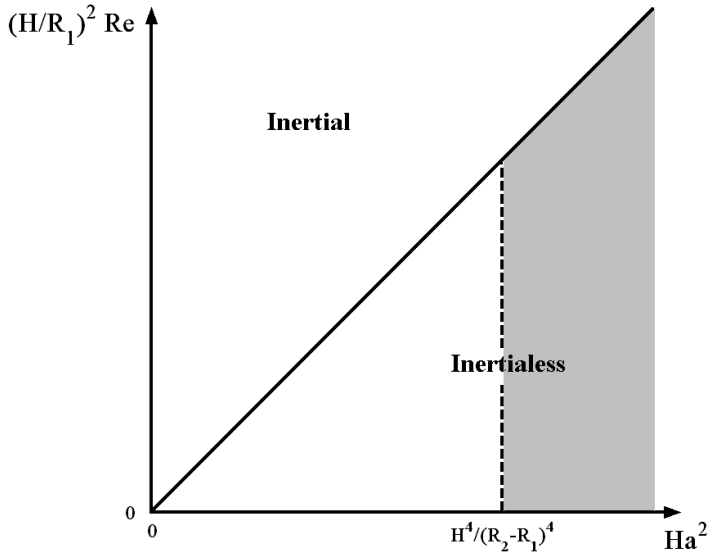

Figure 2.27: Regimes of electrically driven flow and the region of "good" parameters for MRI experiment (shaded area).

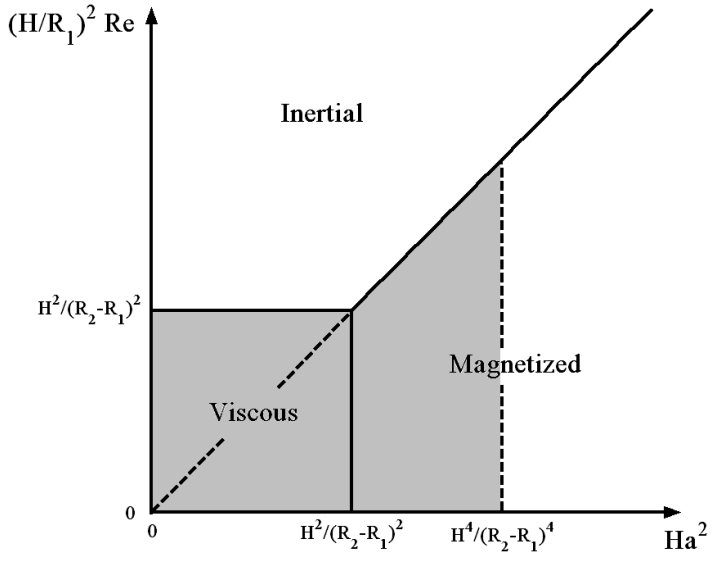

Figure 2.28: Regimes of Taylor-Couette flow and the region of "good" parameters for MRI experiment (shaded area).

Chapter 3

Spectral stability of electrically driven flow in an annular channel: ideal MHD

In the present chapter, the spectral stability of liquid metal rotating in a transverse magnetic field is studied analytically and numerically by solving the eigenvalue problem with rigid-wall boundary conditions. The study is performed for the rotation with angular velocity $\Omega(R) \propto 1/R^2$ in the frame of ideal MHD, neglecting all dissipative effects.

It should be noted that the spectral stability of ideal conducting fluids rotating in a magnetic field have been studied intensively after the rediscovery of magnetorotational instability in the astrophysical context [34, 96–103]. Most of these studies are restricted either to the case of axisymmetric modes (azimuthal number $m = 0$) [34–36, 100, 101] or to the analysis of non-axisymmetric modes ($m \neq 0$) in local approximation [96–99]. The novelty of our study is that we consider the global eigen-modes (satisfying the specific boundary conditions) in both axisymmetric and non-axisymmetric cases. It is shown that non-axisymmetric modes have lower instability threshold.

We also investigate the energetics of non-axisymmetric modes and show that they have negative energy. Therefore, one can expect that such modes are prone to dissipative instabilities as well as instabilities due to coupling of waves with positive and negative energy.

3.1 Statement of the problem

We consider the spectral stability of electrically driven flow of liquid metal in an annular channel (Fig. 1.2). As found in Chapter 2, the angular velocity in such flow has the form (see (2.61))

$$\Omega(R) = \frac{I_0}{4\pi R^2\sqrt{\sigma\rho\nu}} \tag{3.1}$$

almost entirely in the cross-section of the channel[1], if the Hartmann number is large, $\mathrm{Ha} \gg 1$; the effects of inertia are small, $\mathrm{Re} \ll \mathrm{Ha}^2(R_1/H)^2$; and the channel is wide enough, $R_2 - R_1 \gg H/\sqrt{\mathrm{Ha}}$. In the following consideration, we neglect the deviations of the real rotation profile from (3.1) in the boundary layers. We assume that the equilibrium flow has no poloidal circulation (this is justified by the smallness of the poloidal stream function w, see (2.52)) and that the equilibrium magnetic field has no induced components (they are of the order of $\mathrm{Re}_m/\mathrm{Ha} \ll 1$, see (2.2)), so that,

$$\mathbf{V}_e = R\Omega(R)\,\mathbf{e}_\varphi, \tag{3.2}$$

$$\mathbf{B}_e = B_0\mathbf{e}_z. \tag{3.3}$$

Here and subsequently, the index e denotes equilibrium quantity.

Despite the fact that the value of stationary velocity is determined by dissipative effects (finite conductivity σ and viscosity ν of the fluid), in the stability study presented in this Chapter we neglect all of them. We assume that the liquid metal is a perfectly conducting, inviscid, incompressible fluid with constant density ρ. This idealization is valid for flow with high values of the Reynolds ($\mathrm{Re} \gg 1$) and the magnetic Reynolds ($\mathrm{Re}_m \gg 1$) numbers. Such an approach is an important first step for the understanding of the possibility of MRI in an electrically driven flow and revealing MRI's basic physical features in the experiment.

The fluid dynamics in our model is described by the equations of ideal incom-

[1]The angular velocity profile (3.1) also corresponds to Taylor-Couette flow (2.101) with $M_0 = M_1 = M_2$ in the approximation of long cylinders (2.100); this approximation is not valid for the channels considered in Chapters 3 and 4.

pressible MHD (Section 1.3.2)

$$\nabla \cdot \mathbf{V} = 0, \tag{3.4}$$

$$\frac{\partial \mathbf{V}}{\partial t} + (\mathbf{V} \cdot \nabla)\mathbf{V} = -\nabla \Pi + \frac{1}{4\pi\rho}(\mathbf{B} \cdot \nabla)\mathbf{B}, \tag{3.5}$$

$$\nabla \cdot \mathbf{B} = 0, \tag{3.6}$$

$$\frac{\partial \mathbf{B}}{\partial t} = \nabla \times (\mathbf{V} \times \mathbf{B}), \tag{3.7}$$

where $\Pi = (P + \mathbf{B}^2/8\pi)/\rho$ is the total pressure divided by density. The equilibrium state ($\partial/\partial t \to 0$) of the system is determined by (3.2) and (3.3). In general, the equilibrium angular velocity $\Omega(R)$ is arbitrary, since equilibrium can always be maintained by a radial pressure gradient but we will focus mainly on the form of $\Omega(R)$ defined in expression (3.1).

For the purpose of the spectral stability analysis, we linearize equations (3.4)-(3.7) near the equilibrium state (3.2), (3.3):

$$\begin{aligned}
\nabla \cdot \delta\mathbf{V} &= 0, && (3.8)\\
\frac{\partial}{\partial t}\delta\mathbf{V} &+ (\mathbf{V}_e \cdot \nabla)\delta\mathbf{V} + (\delta\mathbf{V} \cdot \nabla)\mathbf{V}_e = && (3.9)\\
&= -\nabla\delta\Pi + \frac{1}{4\pi\rho}(\mathbf{B}_e \cdot \nabla)\delta\mathbf{B} + \frac{1}{4\pi\rho}(\delta\mathbf{B} \cdot \nabla)\mathbf{B}_e, &&\\
\nabla \cdot \delta\mathbf{B} &= 0, && (3.10)\\
\frac{\partial}{\partial t}\delta\mathbf{B} &= \nabla \times (\mathbf{V}_e \times \delta\mathbf{B}) + \nabla \times (\delta\mathbf{V} \times \mathbf{B}_e). && (3.11)
\end{aligned}$$

In ideal MHD model it is advantageous to represent the perturbations of velocity and magnetic field via the Lagrangian displacement vector $\boldsymbol{\xi}$ [23]:

$$\begin{aligned}
\delta\mathbf{V} &= \frac{\partial \boldsymbol{\xi}}{\partial t} + (\mathbf{V}_e \cdot \nabla)\boldsymbol{\xi} - (\boldsymbol{\xi} \cdot \nabla)\mathbf{V}_e = \frac{\partial \boldsymbol{\xi}}{\partial t} + \nabla \times [\boldsymbol{\xi} \times \mathbf{V}_e], && (3.12)\\
\delta\mathbf{B} &= \nabla \times (\boldsymbol{\xi} \times \mathbf{B}_e). && (3.13)
\end{aligned}$$

In this case equations (3.10) and (3.11) are satisfied automatically. The dynamics of the displacement vector $\boldsymbol{\xi}$ is obtained from equation (3.9):

$$\begin{aligned}
\frac{\partial^2 \boldsymbol{\xi}}{\partial t^2} &+ 2(\mathbf{V}_e \cdot \nabla)\frac{\partial \boldsymbol{\xi}}{\partial t} + (\mathbf{V}_e \cdot \nabla)^2\boldsymbol{\xi} - (\boldsymbol{\xi} \cdot \nabla)(\mathbf{V}_e \cdot \nabla)\mathbf{V}_e = && (3.14)\\
&= -\nabla\delta\Pi + \frac{1}{4\pi\rho}(\mathbf{B}_e \cdot \nabla)\delta\mathbf{B} + \frac{1}{4\pi\rho}(\delta\mathbf{B} \cdot \nabla)\mathbf{B}_e.
\end{aligned}$$

Besides, the incompressibility condition (3.8) gives:

$$\nabla \cdot \boldsymbol{\xi} = 0. \tag{3.15}$$

Since all equilibrium quantities depend on the radius R only, the solution to the system (3.14)-(3.15) can be sought in the form of normal modes:

$$\boldsymbol{\xi}(R,\phi,Z,t) = \boldsymbol{\xi}(r)e^{i(m\varphi+K_zZ-\omega t)}, \tag{3.16}$$

$$\delta\Pi(R,\phi,Z,t) = \delta\Pi(r)e^{i(m\varphi+K_zZ-\omega t)}, \tag{3.17}$$

where m (integer) and K_z are the azimuthal mode-number and the axial wave-number, respectively, and ω is the eigen-frequency. Since normal modes (3.16), (3.17) are generally complex, to find the perturbations of physical quantities one has to take either real or imaginary parts of the righthand sides in expressions (3.12), (3.13) and (3.17).

Substituting the normal mode representation (3.16) into equations (3.12) and (3.13) we find the perturbations:

$$\delta\mathbf{V} = -i\bar{\omega}\boldsymbol{\xi} - R\frac{\partial\Omega}{\partial R}\,\xi_r\mathbf{e}_\varphi, \tag{3.18}$$

$$\delta\mathbf{B} = iK_zB_0\boldsymbol{\xi}. \tag{3.19}$$

Then the system (3.14)-(3.15) can be written as

$$(\omega_A^2-\bar{\omega}^2)\xi_r + 2i\Omega\bar{\omega}\xi_\varphi + 2R\Omega\frac{\partial\Omega}{\partial R}\,\xi_r = -\frac{\partial}{\partial R}\,\delta\Pi \tag{3.20}$$

$$(\omega_A^2-\bar{\omega}^2)\xi_\varphi - 2i\Omega\bar{\omega}\xi_r = -\frac{im}{R}\,\delta\Pi, \tag{3.21}$$

$$(\omega_A^2-\bar{\omega}^2)\xi_z = -iK_z\delta\Pi, \tag{3.22}$$

$$\frac{1}{R}\,\frac{\partial(R\xi_r)}{\partial R} + \frac{im}{R}\,\xi_\varphi + iK_z\xi_z = 0, \tag{3.23}$$

where we have introduced the shifted eigen-frequency,

$$\bar{\omega} = \omega - m\Omega(R),$$

and the Alfven frequency,

$$\omega_A = K_zV_A = \frac{K_zB_0}{\sqrt{4\pi\rho}}.$$

The analogous derivation for a more general case, including a toroidal magnetic field, is given in [104].

For computational convenience, we introduce dimensionless quantities, taking as a unit of length the radius of the inner cylindrical boundary R_1 and as a unit of frequency the angular velocity at this radius $\Omega_1 = \Omega(R_1)$. Then we have:

$$r = \frac{R}{R_1}, \quad r_1 = 1, \quad r_2 = \frac{R_2}{R_1}, \quad h = \frac{H}{R_1}, \quad k_z = K_z R_1,$$

$$v_A = \frac{V_A}{R_1\Omega_1}, \quad \tilde{\omega} = \frac{\omega}{\Omega_1}, \quad \tilde{\omega}_A = \frac{\omega_A}{\Omega_1} = k_z v_A, \quad \tilde{\Omega}(r) = \frac{1}{r^2},$$

where R_2 is the radius of the outer cylindrical boundary and H is the channel height. In the following consideration we will omit tildes to simplify the notation.

The system (3.20)-(3.23) can be reduced to one differential equation which in non-dimensional terms is:

$$\begin{aligned}\frac{\partial}{\partial r}\left(\frac{(\bar{\omega}^2-\omega_A^2)r}{m^2+k_z^2r^2}\,\frac{\partial(r\xi_r)}{\partial r}\right) &+ \xi_r\Bigg[-(\bar{\omega}^2-\omega_A^2)+\frac{m\bar{\omega}}{m^2+k_z^2r^2}\left(2r\frac{\partial\Omega}{\partial r}-\frac{4k_z^2r^2\Omega}{m^2+k_z^2r^2}\right)+\\ &+ \frac{4k_z^2r^2\omega_A^2\Omega^2}{(m^2+k_z^2r^2)(\bar{\omega}^2-\omega_A^2)}+\frac{k_z^2r^2\kappa^2}{m^2+k_z^2r^2}\Bigg]=0, \qquad (3.24)\end{aligned}$$

where

$$\kappa^2 \equiv 4\Omega^2 + 2r\Omega\frac{\partial\Omega}{\partial r}$$

is a square of the so-called *epicyclic frequency*. Equation (3.24) is valid for any rotation profile $\Omega(r)$. In our case $\Omega(r) = 1/r^2$, so the epicyclic frequency is zero, $\kappa^2 = 0$.

Since we consider the channel with rigid walls, the velocity components which are perpendicular to the boundary should vanish at that boundary. For the side walls it gives the following boundary conditions

$$\xi_r(r_1) = \xi_r(r_2) = 0. \qquad (3.25)$$

The absence of a z-component of the velocity at the top and bottom walls of the channel leads to a quantization of the axial wave-number k_z, namely,

$$k_z = \frac{\pi n_z}{h}, \qquad (3.26)$$

where n_z is an integer (axial mode-number) and h is the non-dimensional height of the channel.

Equation (3.24) with boundary conditions (3.25) constitutes an eigenvalue problem. The primary objective of our stability study is to determine the spectrum of eigen-frequencies ω which has to be found as a part of the solution. Analyzing this eigenvalue problem, one can conclude that its solution (and eigen-frequency spectrum as well) depends on five parameters: three mode-numbers – azimuthal m, axial n_z and radial n_r (which will be introduced later), a geometrical factor r_2 and the dimensionless Alfven velocity v_A. The present chapter is mainly devoted to the study of the dependencies of eigen-frequencies ω on the mode-numbers m, n_z and n_r.

In numerical calculations, equation (3.24) was discretized on the uniform grid (up to 100 points in the radial direction) and then reduced to the generalized matrix eigen-value problem, which was solved by means of MATLAB. The found eigenvalues and eigen-functions were verified by the standard shooting method using a finer grid (up to 10^6 points in the radial direction); the corresponding code was implemented in C++. Calculations were performed for the geometry of the Obninsk MRI experiment (Table 2.1). In Sections 3.2 and 3.3, the value of normalized Alfven velocity is fixed at $v_A = 0.25$.

3.2 Axisymmetric perturbations, $m = 0$

In the axisymmetric case, with $\Omega(r) = 1/r^2$, equation (3.24) is reduced to

$$\frac{\partial}{\partial r}\left(\frac{1}{r}\frac{\partial(r\xi_r)}{\partial r}\right) + k_z^2\xi_r\left(-1 + \frac{4\omega_A^2\Omega^2}{(\omega^2-\omega_A^2)^2}\right) = 0. \tag{3.27}$$

Multiplying this equation by the complex conjugate $r\xi_r^*$ and integrating over the interval $[r_1, r_2]$, one obtains the following variational form

$$\int_{r_1}^{r_2}\left(-\frac{1}{r^2}\left|\frac{\partial(r\xi_r)}{\partial r}\right|^2 - k_z^2|\xi_r|^2 + \frac{4k_z^2\omega_A^2\Omega^2}{(\omega^2-\omega_A^2)^2}|\xi_r|^2\right)rdr = 0. \tag{3.28}$$

Some conclusions can be made from its consideration:

1. The expression $\alpha^4 \equiv (\omega^2 - \omega_A^2)^2$ has a real positive value. Therefore, $\omega^2 = \omega_A^2 \pm \alpha^2$ is real and eigen-frequencies ω are either purely real or purely imaginary.

2. The eigen-frequency spectrum is symmetric with respect to both axes in the complex ω-plane.

3. The eigen-functions ξ_r can always be chosen to be real.

4. There is a degeneracy: each eigen-function ξ_r corresponds to four eigen-frequencies ω. Two of them are always real, $\omega = \pm\sqrt{\omega_A^2 + \alpha^2}$, which means stability. Two others can be imaginary, $\omega = \pm\sqrt{\omega_A^2 - \alpha^2}$, which means instability. This instability is known as the axisymmetric magnetorotational instability (MRI of the axisymmetric modes).

Besides the azimuthal and axial mode-numbers, m and n_z, to describe eigen-frequencies completely we have to introduce the radial mode-number n_r which is defined in the axisymmetric case as a number of nodes of the corresponding real eigen-function. The eigen-spectrum can be represented now by the formal dispersion relation $\omega = \omega(n_r, m, n_z)$, which relates each set of mode-numbers (n_r, m, n_z) with values of eigen-frequencies ω.

It should be noted here that the axisymmetric modes are well described by the so-called *WKB approximation*[2] [100]. In this approximation, fast oscillating radial dependence of perturbations is assumed, i. e.,

$$\xi_r(r) \sim e^{ik_r r}, \quad k_r r \gg 1, \tag{3.29}$$

where radial wave-number k_r is related to the radial mode-number n_r by

$$k_r = \frac{\pi(n_r + 1)}{r_2 - r_1}. \tag{3.30}$$

Substitution of (3.29) into equation (3.27) results in

$$\omega = \pm\sqrt{\omega_A^2 \pm \frac{2k_z\omega_A\Omega}{\sqrt{k_r^2 + k_z^2}}}, \tag{3.31}$$

[2]This method is named after physicists Wentzel, Kramers, and Brillouin, who developed it in 1926 for semiclassical calculations in quantum mechanics.

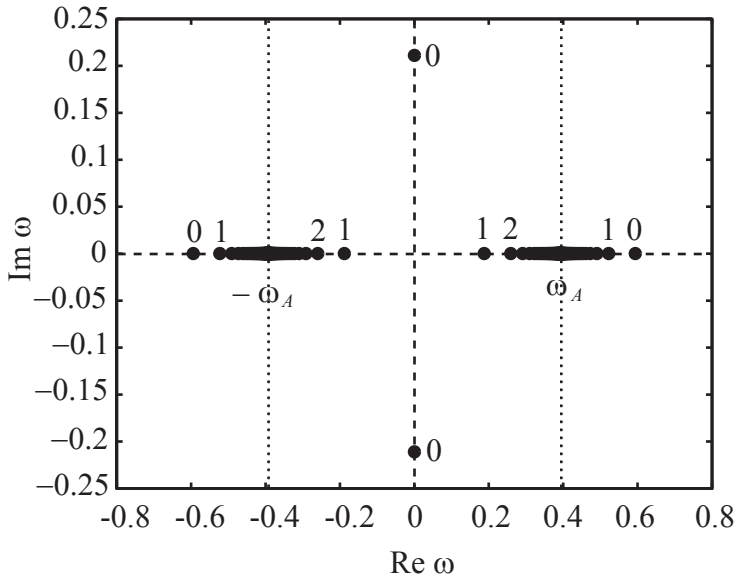

Figure 3.1: Eigen-frequency spectrum in the case $m = 0$, $k_z = \pi/2$, $v_A = 0.25$. Dashed lines represent real and imaginary axes, dotted lines correspond to Alfven resonances. Radial mode-numbers n_r are shown for some modes. The unit of frequency is Ω_1.

which is an approximate dispersion relation for axisymmetric modes. From this equation it follows that the instability in the system is excited if

$$\Omega > \frac{1}{2}\sqrt{k_r^2 + k_z^2}\, v_A.$$

Using the definition of the Alfven number (1.27), the threshold of axisymmetric MRI can be also written as

$$\mathrm{Re}_{cr} = \frac{\mathrm{Ha} R^2 \sqrt{K_r^2 + K_z^2}}{2L\sqrt{\mathrm{Pr}_m}}. \tag{3.32}$$

For $m = 0$ and the lowest axial wave-number $k_z = \pi/2$ ($n_z = 1$), the spectrum of eigen-frequencies is shown in Fig. 3.1. As one can see, there is a purely imaginary eigen-frequency in the upper half-plane which corresponds to the magneto-rotational instability. Also the spectrum has two accumulation points at $\omega = \pm\omega_A$ (Alfven resonances). When approaching these points, the radial wave-number increases, which is confirmed by the dispersion relation (3.31).

The eigen-spectrum shown in Fig. 3.1 is formed from coupled Alfven and slow magnetosonic modes. Unlike [105], we did not obtain the fast magnetosonic modes since our consideration is restricted to the incompressible MHD model.

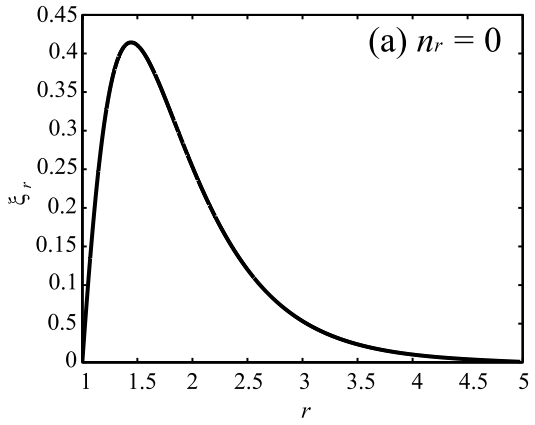

(a) $n_r = 0$, $\omega = \pm 0.2099i$, $\pm\, 0.5937$

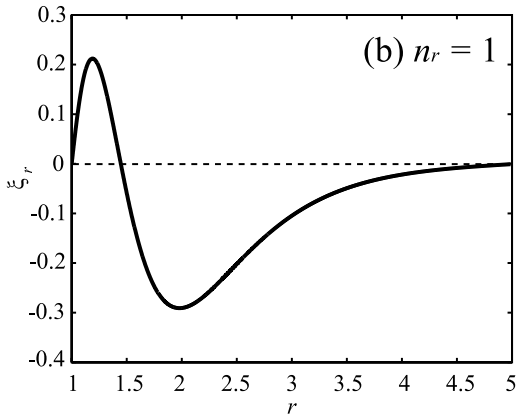

(b) $n_r = 1$, $\omega = \pm 0.1908$, $\pm\, 0.5216$

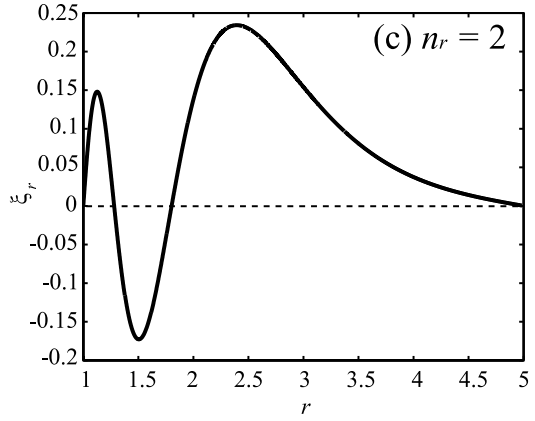

(c) $n_r = 2$, $\omega = \pm 0.2625$, $\pm\, 0.4894$

Figure 3.2: Eigen-functions in the case $m = 0$, $k_z = \pi/2$, $v_A = 0.25$. The corresponding radial wave-numbers and eigen-frequencies are shown. The unit of frequency is Ω_1.

It should be noted here that the Alfven resonance lines, $Re\,\omega = \pm\omega_A$, divide the complex ω-plane into 3 regions[3]:

1. left outer, $Re\,\omega < -\omega_A$;
2. inner, $-\omega_A < Re\,\omega < \omega_A$;
3. right outer, $Re\,\omega > \omega_A$.

The outer modes belonging to regions 1 and 3 are always stable (the corresponding eigen-frequencies are real). The unstable modes can emerge only in the central region 2 as a result of coupling of originally stable inner modes. As we show in Section 3.3, this tendency is valid for non-axisymmetric modes as well.

In Fig. 3.2, the samples of axisymmetric eigen-functions with different radial wave-numbers n_r are shown. In general, no conclusion about the localization of these modes can be made.

3.3 Non-axisymmetric perturbations, $m \neq 0$

In the case of non-axisymmetric perturbations one has to solve the full equation (3.24) in order to obtain the eigen-frequencies and make a judgment on the stability of the system. Some important properties of the eigen-frequency spectrum can be established prior to solving the problem:

1. The eigen-frequencies of non-axisymmetric modes may assume generally complex values.
2. In the complex ω-plane, the eigen-frequency spectrum is symmetric with respect to the line $Im\,\omega = 0$. That is, if ω is an eigen-frequency then its complex conjugate ω^* is also eigen-frequency. The presence of complex conjugate pairs in the eigenvalue spectrum indicates the instability of the equilibrium under consideration since one of these eigen-frequencies corresponds to the perturbation growing in time.

[3] *Re* and *Im* denote the real and imaginary parts of the complex number, respectively

3. Eigen-functions ξ_r are generally complex.

4. There is no degeneracy in this case: each eigen-frequency corresponds to a different eigen-function.

In the non-axisymmetric case, the Alfven resonances form two resonance zones in the complex ω-plane: left

$$\min_{r\in[r_1,\ r_2]}(-\omega_A + m\Omega(r)) < Re\ \omega < \max_{r\in[x_1,\ r_2]}(-\omega_A + m\Omega(r)), \tag{3.33}$$

and right

$$\min_{r\in[r_1,\ r_2]}(\omega_A + m\Omega(r)) < Re\ \omega < \max_{r\in[r_1,\ r_2]}(\omega_A + m\Omega(r)), \tag{3.34}$$

where the resonance condition $Re\ \omega = \pm\omega_A + m\Omega(r)$ is satisfied for some point $r \in [r_1,\ r_2]$. As follows from our numerical analysis, for each set of mode-numbers (n_r, m, n_z) there are four different eigen-frequencies. Two of them are always real (stable) and situated just outside the resonance zones, one in the left outer region, with

$$Re\ \omega < \min_{r\in[r_1,\ r_2]}(-\omega_A + m\Omega(r)),$$

and another one in the right outer region, with

$$Re\ \omega > \max_{r\in[r_1,\ r_2]}(\omega_A + m\Omega(r)).$$

The other two eigen-frequencies lie either in the inner region between the resonances

$$\max_{r\in[r_1,\ r_2]}(-\omega_A + m\Omega(r)) < Re\ \omega < \min_{r\in[r_1,\ r_2]}(\omega_A + m\Omega(r)),$$

or in the resonance zones if these zones overlap. In the former case, the eigen-frequencies can be real or complex conjugate, depending on the problem parameters. In the latter case, the eigen-frequencies are necessarily complex conjugate, signifying the presence of instability.

As a typical example of a non-axisymmetric eigen-frequency spectrum, the spectrum for $m = 1$ modes is shown in Fig. 3.3. In this case, the resonance zones overlap and all the inner eigen-frequencies are complex conjugate (due to the resolution of Fig. 3.3 this fact is not so obvious for modes with small imaginary parts of eigen-frequencies). In Fig. 3.4 samples of these unstable eigen-modes are presented.

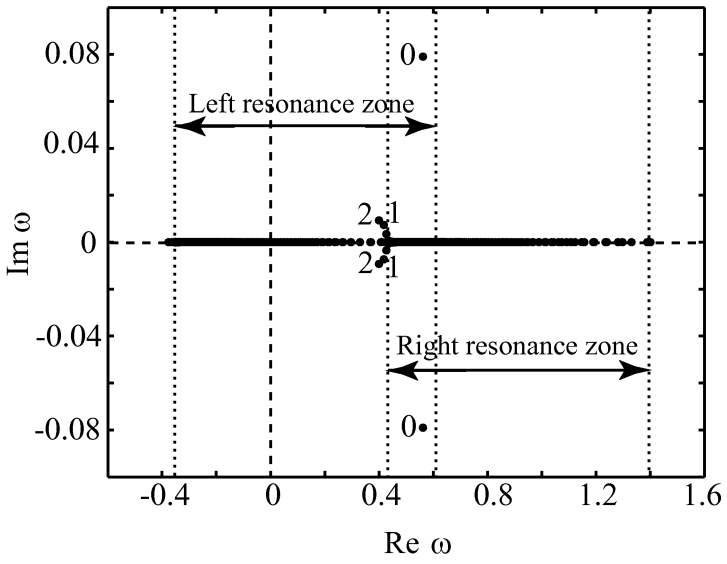

Figure 3.3: Eigen-frequency spectrum in the case $m = 1$, $k_z = \pi/2$, $v_A = 0.25$. Dashed lines represent real and imaginary axes, dotted lines correspond to the boundaries of Alfven resonance zones. Radial mode-numbers n_r are shown for some modes. The unit of frequency is Ω_1.

Note that in the case of an unstable mode with a very small imaginary part of the eigen-frequency, a narrow singular layer is formed around the resonance point r_s defined by the condition

$$\text{Re } \omega = \pm\omega_A + m\Omega(r_s).$$

The eigen-function has steep gradients in the neighborhood of this point (see Fig. 3.4(b), 3.4(c)).

For an unstable non-axisymmetric mode the definition of its radial mode-number n_r is not so obvious as for an axisymmetric one because the non-axisymmetric eigen-function is complex. We resolve this problem as follows: changing m continuously from its initial value to $m = 0$, we find the corresponding axisymmetric mode with known n_r; this n_r is taken to be the radial mode-number of the original non-axisymmetric mode. Although such a definition is mathematically correct and non-ambiguous, sometimes it leads to confusing results. For example, comparing Fig. 3.4(b) and Fig. 3.4(c) one can see that both real and imaginary parts of the

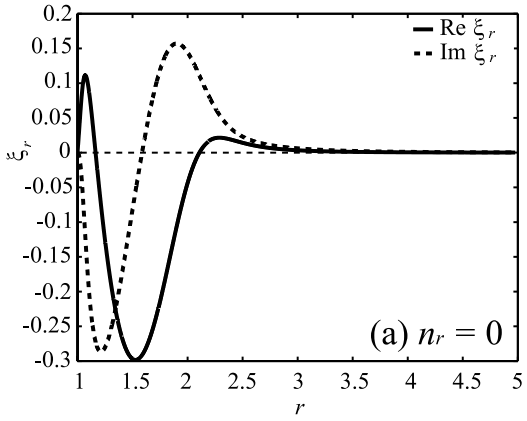

(a) $n_r = 0$, $\omega = 0.5623 + 0.0791i$

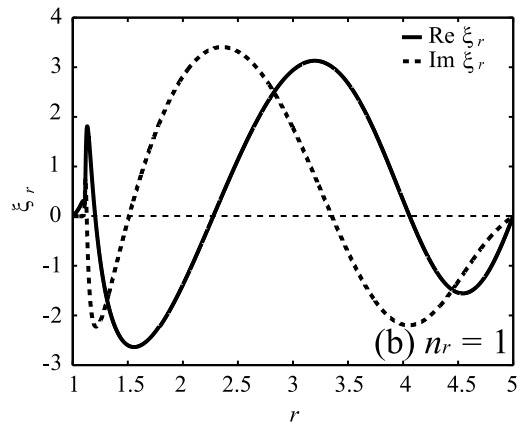

(b) $n_r = 1$, $\omega = 0.4173 + 0.0073i$

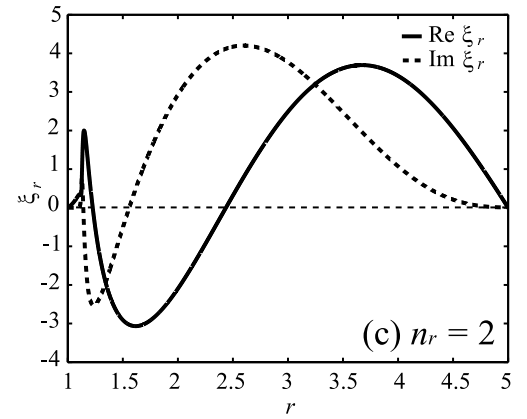

(c) $n_r = 2$, $\omega = 0.3994 + 0.0093i$

Figure 3.4: Eigen-functions in the case $m = 1$, $k_z = \pi/2$, $v_A = 0.25$. Real part is solid line and imaginary part is dashed line. Corresponding radial mode-numbers and eigen-frequencies are shown. The unit of frequency is Ω_1.

eigen-function with $n_r = 2$ have a less number of nodes than the corresponding parts of the eigen-function with $n_r = 1$.

Our main numerical results are related to the study of MRI growth rate (or increment, $\gamma = Im\ \omega$) as a function of numbers n_r, m, k_z. Fig. 3.5 demonstrates the dependence of the instability growth rate on the azimuthal wave-number m (m is used here as continuous parameter) for eigen-modes with different radial mode-numbers n_r. As one can see, beginning with $n_r = 1$, the system under consideration has a threshold of instability, m_{cr}; m_{cr} is larger for larger n_r. If $m > m_{cr}$ the eigen-mode with corresponding radial mode-number is always unstable, although the increment of instability decreases with growth of m. This fact contradicts the local approximation in which the unstable modes become stabilized with increasing values of m (see, for example, [98]). Also it is worth noting that the maximum possible value of the increment decreases with the increase of radial wave-number n_r. In this sense the most unstable mode is the mode with the lowest radial wave-number, $n_r = 0$.

Fig. 3.6 demonstrates the dependence of the increment γ on the azimuthal mode-number m and the axial wave-number k_z for most unstable modes with $n_r = 0$. According to this dependence, for every value of m there exists a threshold value of the axial wave-number $k_z^{(cr)}(m)$ after which the eigen-mode with $n_r = 0$ is always stable. This threshold value increases with growth of m and approaches the asymptote $k_z^{(cr)} \propto m$ (this is explained further in Section 3.4). Dependencies of the increment on k_z for some m are shown in more details in Fig. 3.7. In fact, this figure represents the sections of Fig. 3.6 at corresponding m.

Since the minimal axial wave-number k_z is determined by the height of the channel (see equation 3.26), we conclude that choosing the height to be small enough (that is the minimal k_z is bigger than $k_z^{(cr)}$) one can suppress the instabilities with low m. In particular, the situation is possible when there is instability for $m = 1$ mode but there is no instability for the axisymmetric $m = 0$ mode.

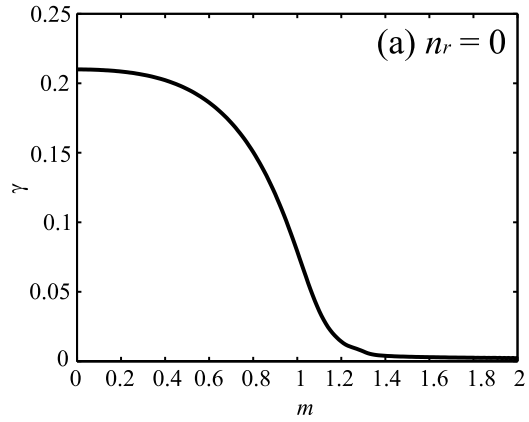

(a) $n_r = 0$

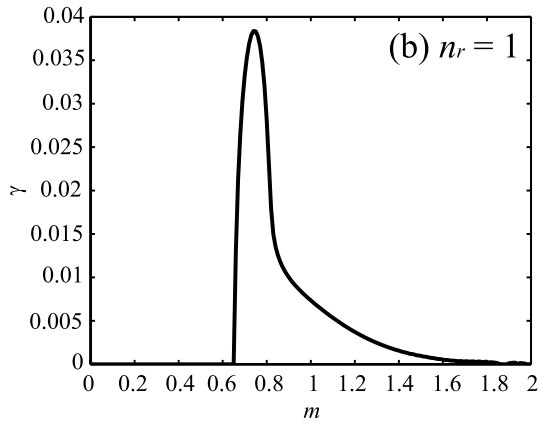

(b) $n_r = 1$

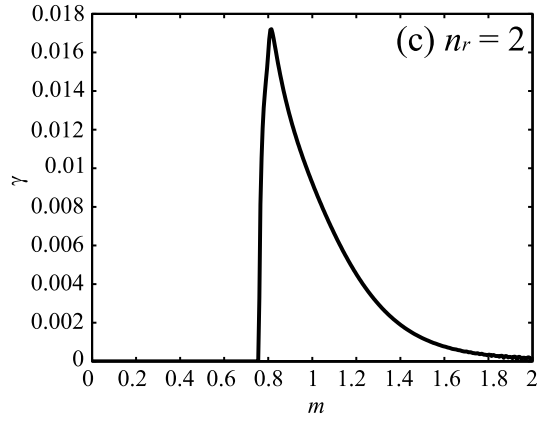

(c) $n_r = 2$

Figure 3.5: Growth rate dependence on azimuthal mode-number m in the case $k_z = \pi/2$, $v_A = 0.25$ for different radial mode-numbers n_r. The unit of frequency is Ω_1.

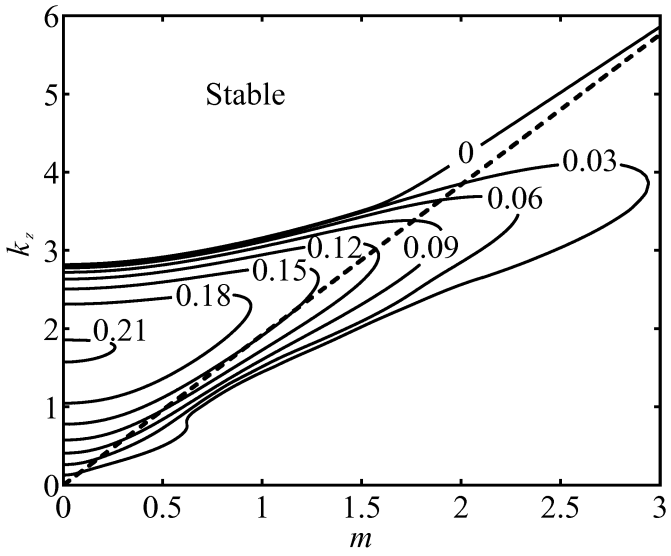

Figure 3.6: Growth rate dependence on the azimuthal mode-number m and the axial wave-number k_z in the case $n_r = 0$, $v_A = 0.25$. Solid contours show the levels of function $\gamma(m, k_z)$. The dashed line is the asymptote for the contour $\gamma(m, k_z) = 0$. The unit of frequency is Ω_1.

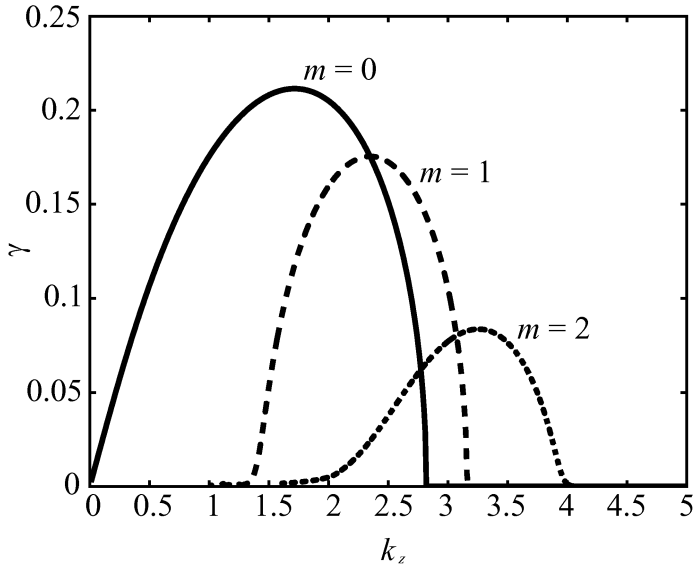

Figure 3.7: Growth rate dependence on the axial wave-number k_z for different m in the case $n_r = 0$, $v_A = 0.25$. Solid line is for $m = 0$, dashed – for $m = 1$, dotted – for $m = 2$. The unit of frequency is Ω_1.

3.4 Marginal stability

As we have mentioned in Section 3.3, if the Alfven resonance zones in the complex ω-plane overlap then the inner modes become unstable. Although we checked this statement only for the small range of m (from 0 to 3) we believe that this is also true for larger m. Our limitations in m are related to computer accuracy: in fact, the growth rates for large m are so small that they cannot be resolved in the code even by double float representation.

From this statement and conditions (3.33), (3.34) it follows that all inner modes (with any radial mode-number n_r) become unstable if

$$\max_{r\in[r_1,\ r_2]}(m\Omega(r)-\omega_A)=\min_{r\in[r_1,\ r_2]}(m\Omega(r)+\omega_A).$$

Taking into account that the angular velocity profile is $\Omega(x)=1/r^2$, we obtain

$$m-\omega_A=\frac{m}{r_2^2}+\omega_A,$$

which gives a critical value for the axial wave-number k_z as a function of m:

$$k_z^{(cr)}(m)=\frac{m}{2v_A}\left(1-\frac{1}{r_2^2}\right). \tag{3.35}$$

This means that all inner modes (with any n_r) become unstable if the axial wave-number k_z is less than the critical value defined by (3.35).

In reality the instability can occur for larger values of k_z as the actual marginal stability curves depend on the radial mode-number n_r. In Fig. 3.8 the marginal stability curves calculated for $n_r=0$ and $n_r=1$ are shown. For comparison, the critical line $k_z^{(cr)}(m)$ is also plotted. It is quite clear that this line is an asymptote for both of the presented curves in the limit $m\to\infty$. The critical line almost coincides with the marginal stability in the case of large radial wave-numbers, $n_r\gg 1$.

Note that the system under consideration has the only unstable axisymmetric mode with radial mode-number $n_r=0$. All axisymmetric modes with $n_r\geq 1$ are stable regardless of the value of k_z. From Fig. 3.8 and expression (3.35) it also follows that in this system there are always non-axisymmetric eigen-modes which are spectrally unstable due to a magnetorotational instability.

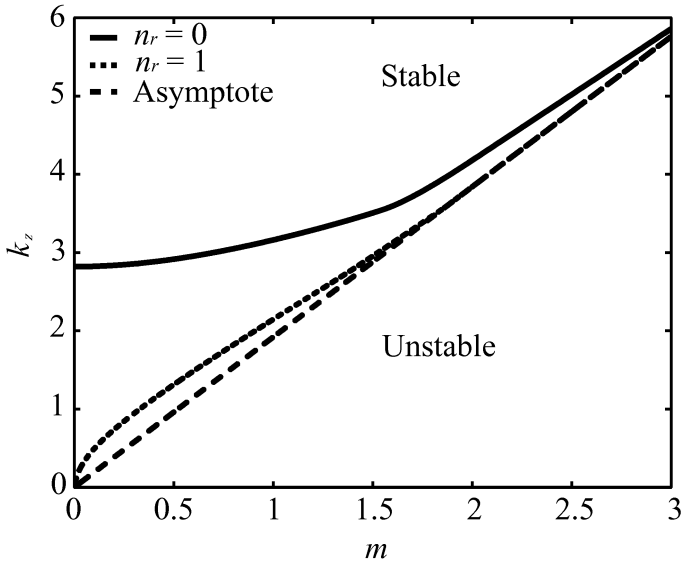

Figure 3.8: Marginal stability in (k_z, m)-plane for different radial mode-numbers n_r. Solid line is $n_r = 0$, dotted is $n_r = 1$; dashed line is their asymptote (3.35).

Expression (3.35) can be written in dimensional terms as

$$\frac{\Omega_1^{cr}}{\omega_A} = \frac{2}{m(1 - R_1^2/R_2^2)}. \tag{3.36}$$

This equation determines the MRI threshold for the ratio of angular velocity to Alfven frequency at large m. The threshold decreases with azimuthal number m and therefore the most dangerous modes with respect to MRI are those with larger m (though they have a smaller instability growth rate). The dependence of the MRI threshold on the azimuthal number m is shown in Fig. 3.9. Using the definition of the Alfven number (1.27), equation (3.36) can be also cast in the form:

$$\mathrm{Re}_{cr} = \frac{2K_z R_1^2 \mathrm{Ha}}{mL\sqrt{\mathrm{Pr}_m}\,(1 - R_1^2/R_2^2)}, \tag{3.37}$$

which gives a high-m MRI threshold on the Ha $-$ Re plane.

3.5 Modes with negative energy

Energy consideration is of primary significance in the stability study of different MHD systems. It is well known that the energy associated with waves (purely

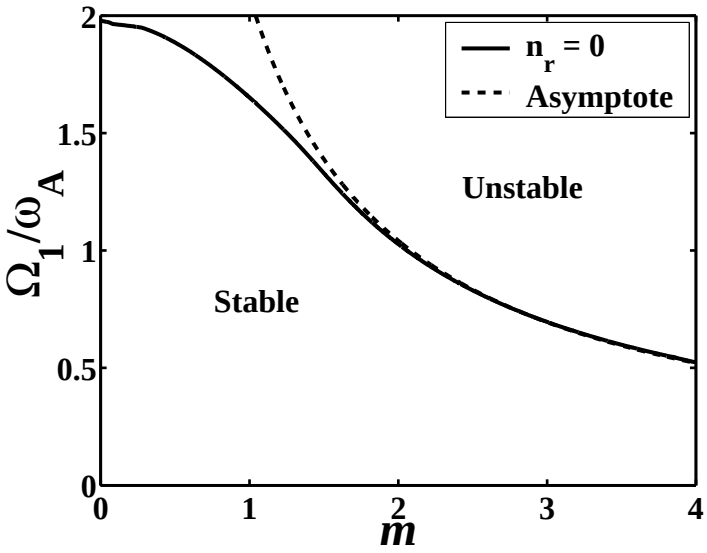

Figure 3.9: The dependence of the stability threshold Ω_1/ω_A on m for the radial mode-number $n_r = 0$ (solid line) and its asymptote for large m (3.36) (dashed line).

oscillatory linear modes) in systems with flows may change its sign and become negative [106, 107]. As the negative energy waves are excited, the total energy of the medium with such a wave diminishes. A negative energy wave is a potential source of instability since no energy is needed to increase its intensity; instead, the energy needs to be withdrawn from the wave. For example, if a negative energy wave is subject to external dissipation, the subsequent removal of energy from the wave will cause it to grow. In a conservative system, the instability can occur due to the simultaneous excitation of positive and negative energy waves. In this case, energy flows from the negative energy wave to the positive energy wave, allowing both modes to grow and the total energy to remain constant. Waves having energies of various signs enable researchers to explain different types of instabilities in fluid dynamics [108].

In the present section, we calculate the energy of the eigen-modes in ideal one-fluid MHD and show that almost all the instabilities in MHD systems with equilibrium flows are related to the coupling of negative and positive energy waves. In our discussion we follow [23] and represent linear dynamics of displacement vector $\boldsymbol{\xi}$

(3.14) in the form:

$$\rho\frac{\partial^2\boldsymbol{\xi}}{\partial t^2} + 2\rho(\mathbf{V}_e\cdot\nabla)\frac{\partial\boldsymbol{\xi}}{\partial t} - \mathbf{F}[\boldsymbol{\xi}] = 0, \tag{3.38}$$

This equation is valid for both compressible and incompressible MHD models, the difference being only in the particular form of the linearized force operator $\mathbf{F}[\boldsymbol{\xi}]$. In the case of incompressible MHD it is given by[4]

$$\begin{aligned}\mathbf{F}[\boldsymbol{\xi}] &= -\rho(\mathbf{V}_e\cdot\nabla)^2\boldsymbol{\xi} + \rho(\boldsymbol{\xi}\cdot\nabla)(\mathbf{V}_e\cdot\nabla)\mathbf{V}_e - \rho\nabla\delta\Pi + \\ &+ \frac{1}{4\pi}(\mathbf{B}_e\cdot\nabla)\delta\mathbf{B} + \frac{1}{4\pi}(\delta\mathbf{B}\cdot\nabla)\mathbf{B}_e.\end{aligned} \tag{3.39}$$

A number of formal properties of equation (3.38) can be established. The force operator $\mathbf{F}[\boldsymbol{\xi}]$ is Hermitian (self-adjoint) in the following sense,

$$\int \boldsymbol{\eta}\cdot\mathbf{F}[\boldsymbol{\xi}]\,d^3\mathbf{R} = \int \boldsymbol{\xi}\cdot\mathbf{F}[\boldsymbol{\eta}]\,d^3\mathbf{R}, \tag{3.40}$$

while the second term in (3.38) is antisymmetric:

$$\int \rho\boldsymbol{\eta}\cdot(\mathbf{V}_e\cdot\nabla)\boldsymbol{\xi}\,d^3\mathbf{R} = -\int \rho\boldsymbol{\xi}\cdot(\mathbf{V}_e\cdot\nabla)\boldsymbol{\eta}\,d^3\mathbf{R}. \tag{3.41}$$

Integration in equations (3.40) and (3.41) is performed over the fluid volume and perturbations at the boundary are taken to be zero.

In the subsequent consideration, the displacement vector $\boldsymbol{\xi}$ can generally assume complex values. In order to obtain the correct expression for energy in this case, we multiply equation (3.38) by the complex conjugate $\partial\boldsymbol{\xi}^*/\partial t$ and integrate it over the entire space:

$$\int\left(\rho\frac{\partial\boldsymbol{\xi}^*}{\partial t}\cdot\frac{\partial^2\boldsymbol{\xi}}{\partial t^2} + 2\rho\frac{\partial\boldsymbol{\xi}^*}{\partial t}\cdot(\mathbf{V}_e\cdot\nabla)\frac{\partial\boldsymbol{\xi}}{\partial t} - \frac{\partial\boldsymbol{\xi}^*}{\partial t}\cdot\mathbf{F}[\boldsymbol{\xi}]\right)d^3\mathbf{R} = 0. \tag{3.42}$$

The complex conjugate of this equality is

$$\int\left(\rho\frac{\partial\boldsymbol{\xi}}{\partial t}\cdot\frac{\partial^2\boldsymbol{\xi}^*}{\partial t^2} + 2\rho\frac{\partial\boldsymbol{\xi}}{\partial t}\cdot(\mathbf{V}_e\cdot\nabla)\frac{\partial\boldsymbol{\xi}^*}{\partial t} - \frac{\partial\boldsymbol{\xi}}{\partial t}\cdot\mathbf{F}[\boldsymbol{\xi}^*]\right)d^3\mathbf{R} = 0. \tag{3.43}$$

Summing up equations (3.42), (3.43) and using the properties (3.40), (3.41) we arrive at the energy conservation law in the form $\partial E/\partial t = 0$, where

$$E = \frac{1}{2}\int\left(\rho\left|\frac{\partial\boldsymbol{\xi}}{\partial t}\right|^2 - \boldsymbol{\xi}^*\cdot\mathbf{F}[\boldsymbol{\xi}]\right)d^3\mathbf{R}. \tag{3.44}$$

[4]The expression for the force operator $\mathbf{F}[\boldsymbol{\xi}]$ in ideal compressible MHD is given in Chapter 5.

As usual in mechanics, the energy consists of a kinetic part (first term) and a potential part (second term).

Since the equilibrium quantities have no time dependence, we look for a normal-mode solution to the equation (3.38)

$$\boldsymbol{\xi}(\mathbf{R},t) = \hat{\boldsymbol{\xi}}(\mathbf{R})e^{-i\omega t}. \tag{3.45}$$

Then the equation of motion (3.38) leads to the eigenvalue problem

$$\omega^2\rho\hat{\boldsymbol{\xi}} + 2i\omega\rho(\mathbf{V}_e\cdot\nabla)\hat{\boldsymbol{\xi}} + \mathbf{F}[\hat{\boldsymbol{\xi}}] = 0. \tag{3.46}$$

Multiplying this equation by the complex conjugate $\hat{\boldsymbol{\xi}}^*$ and integrating over the fluid volume, we arrive at a quadratic equation for eigen-frequency ω:

$$A\,\omega^2 - 2B\,\omega - C = 0, \tag{3.47}$$

with coefficients

$$A = \int \rho|\hat{\boldsymbol{\xi}}|^2\,d^3\mathbf{R} > 0, \tag{3.48}$$

$$B = -i\int \rho\hat{\boldsymbol{\xi}}^*\cdot(\mathbf{V}_e\cdot\nabla)\hat{\boldsymbol{\xi}}\,d^3\mathbf{R}, \tag{3.49}$$

$$C = -\int \hat{\boldsymbol{\xi}}^*\cdot\mathbf{F}[\hat{\boldsymbol{\xi}}]\,d^3\mathbf{R}. \tag{3.50}$$

We note that the coefficient B is real (this follows immediately from the equation (3.41)). The solution to the equation (3.47) is

$$\omega_{1,2} = \frac{B \pm \sqrt{B^2+AC}}{A}, \tag{3.51}$$

which means that instability in the system is possible only if $B^2 + AC < 0$.

We are now able to determine the energy of the eigen-modes corresponding to the eigen-frequencies (3.51). Substituting (3.45) into expression (3.44) one obtains:

$$E = \frac{1}{2}\,(A\,|\,\omega|^2 + C). \tag{3.52}$$

In the case of unstable modes, $B^2 + AC < 0$ and

$$|\,\omega_{1,2}|^2 = -\frac{C}{A},$$

so the energy is

$$E_{1,2} = 0. \tag{3.53}$$

For stable modes, we have $B^2 + AC \geq 0$ and the energy is

$$E_{1,2} = \frac{\sqrt{B^2+AC}}{A}\left(\sqrt{B^2+AC} \pm B\right). \tag{3.54}$$

Depending on the system parameters, the following options are possible for stable eigen-modes (we assume $B \geq 0$ for simplicity):

1. $C = -B^2/A \quad \Longrightarrow \quad E_1 = 0,\ E_2 = 0; \quad \omega_1 > 0,\ \omega_2 > 0;$
2. $-B^2/A < C < 0 \quad \Longrightarrow \quad E_1 > 0,\ E_2 < 0; \quad \omega_1 > 0,\ \omega_2 > 0;$
3. $C = 0 \quad \Longrightarrow \quad E_1 > 0,\ E_2 = 0; \quad \omega_1 > 0,\ \omega_2 = 0;$
4. $C > 0 \quad \Longrightarrow \quad E_1 > 0,\ E_2 > 0; \quad \omega_1 > 0,\ \omega_2 < 0.$

As one can see, there is an interval of parameters at which the eigen-modes with positive and negative energies exist (option 2). One boundary of this interval corresponds to the marginal stability (option 1), the other – to the change of sign of eigen-frequency ω_2 (option 3). This result suggests that instability in the ideal MHD system with flow can be associated with coupling of positive and negative energy waves.

In order to verify these simple analytical results, we calculate the energy of eigen-modes in the system described in the present Chapter (see Section 3.1). The energy corresponding to the force operator (3.39) with equilibrium velocity (3.2) and magnetic field (3.3) is given by

$$E = \frac{\rho}{2}\int\left(\left|\frac{\partial \boldsymbol{\xi}}{\partial t}\right|^2 + (\omega_A^2 - m^2\Omega^2)|\boldsymbol{\xi}|^2 + R\frac{\partial \Omega^2}{\partial R}|\,\xi_r|^2 + 2im\Omega^2(\xi_r\xi_\varphi^* - \xi_r^*\xi_\varphi)\right) d^3\mathbf{R}. \tag{3.55}$$

Substituting $\boldsymbol{\xi}$ from the eigenvalue problem (3.20)-(3.23) we find the energy of the stable eigen-mode with frequency ω:

$$E_{m\neq 0} = \pi\rho H\omega\int_{R_1}^{R_2}\left[\bar{\omega}\left(\xi_r^2 \;+\; \frac{1}{m^2+K_z^2R^2}\left(\frac{\partial(R\xi_r)}{\partial R}\right)^2 + \frac{4K_z^2R^2\Omega^2\omega_A^2\xi_r^2}{(\omega_A^2-\bar{\omega}^2)^2(m^2+K_z^2R^2)}\right) + \right.$$
$$\left. + \;\frac{2m\Omega\xi_r}{m^2+K_z^2R^2}\frac{\partial(R\xi_r)}{\partial R}\right] R\,dR. \tag{3.56}$$

For axisymmetric perturbations with $m = 0$ this expression is reduced to

$$E_{m=0} = \pi\rho H\omega^2 \int_{R_1}^{R_2} \left[\xi_r^2 + \frac{1}{K_z^2 R^2}\left(\frac{\partial(R\xi_r)}{\partial R}\right)^2 + \frac{4\Omega^2\omega_A^2\xi_r^2}{(\omega_A^2 - \omega^2)^2}\right] R\,dR > 0. \qquad (3.57)$$

Therefore, the energy of axisymmetric perturbations is always positive if $\omega \neq 0$. Formally, this case is described by (3.54) with coefficient $B = 0$.

In figures 3.10, 3.11 the calculated dependencies of energy and frequency for two potentially unstable modes on the parameter Ω_1/ω_A are shown. In the case $m = 0$, both branches of energy are positive and coincident (Fig. 3.10(a)). The merging point corresponds to $\Omega_1/\omega_A \approx 2.0$ which is the MRI threshold for $m = 0$ (see Fig. 3.9). The nature of axisymmetric (classical) MRI is not related to the subject of negative energy waves and can be explained by a mechanism similar to Rayleigh-Taylor instability [35].

For $m = 1$ the behavior of both energy curves in Fig. 3.11(a) is completely described by equation (3.54). The MRI threshold in this case is $\Omega_1/\omega_A \approx 1.7$ (see Fig. 3.9). When $1.1 \lesssim \Omega_1/\omega_A \lesssim 1.7$ the positive and negative energy wave can coexist in the system. At $\Omega_1/\omega_A \approx 1.1$ the frequency ω_2 changes sign (Fig. 3.11(b)), so both energy branches become positive. These numerical results confirm the analytical part of our study and suggest that non-axisymmetric MRI in a rotating fluid can be explained as a coupling of positive and negative energy waves.

3.6 Conclusions

We have examined the spectral stability of electrically driven liquid metal flow in the model relevant to MRI experiment and presented a detailed numerical analysis of eigen-functions and eigen-frequencies inherent in this model. The obtained results show that the rotation profile given by expression (3.1) is unstable due to MRI. For the chosen parameters of the experimental device, the highest growth rate of instability γ corresponds to the axisymmetric mode $m = 0$ with the lowest radial wave-number $n_r = 0$.

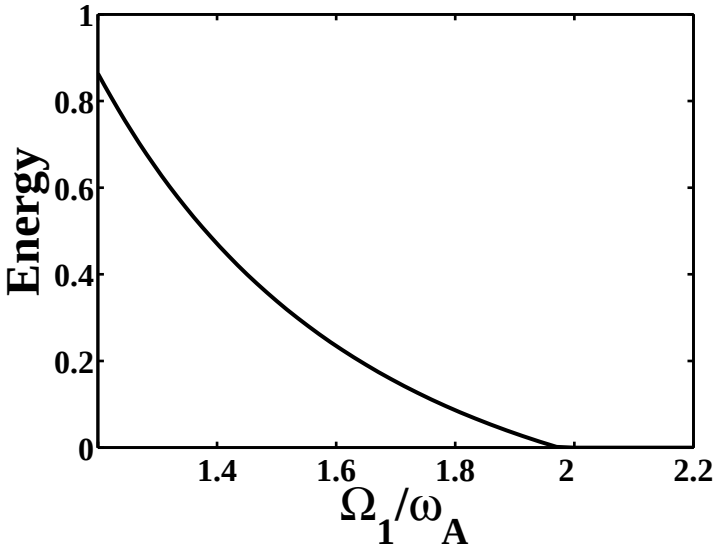

(a) Energy (arbitrary units)

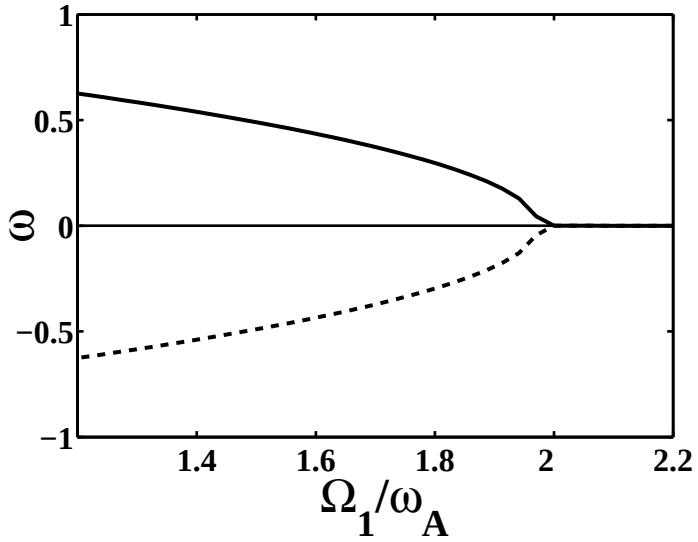

(b) Frequency (in units of Ω_1)

Figure 3.10: Dependencies of energy and frequency on the ratio Ω_1/ω_A for two inner eigen-modes in the case $m = 0$.

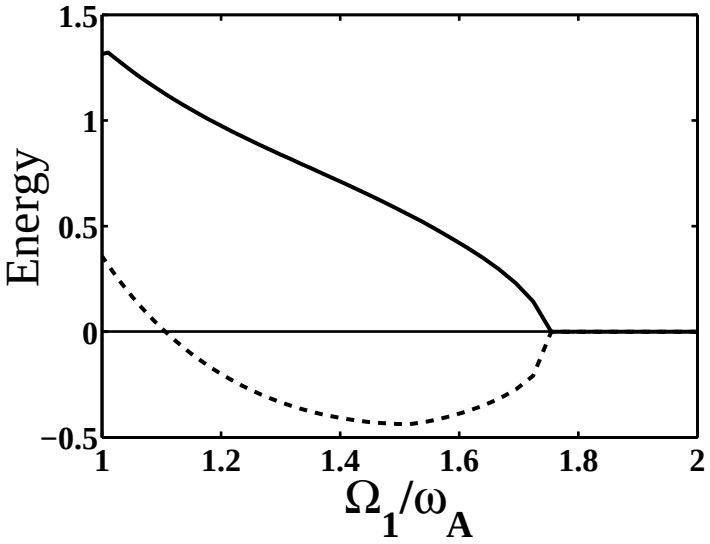

(a) Energy (arbitrary units)

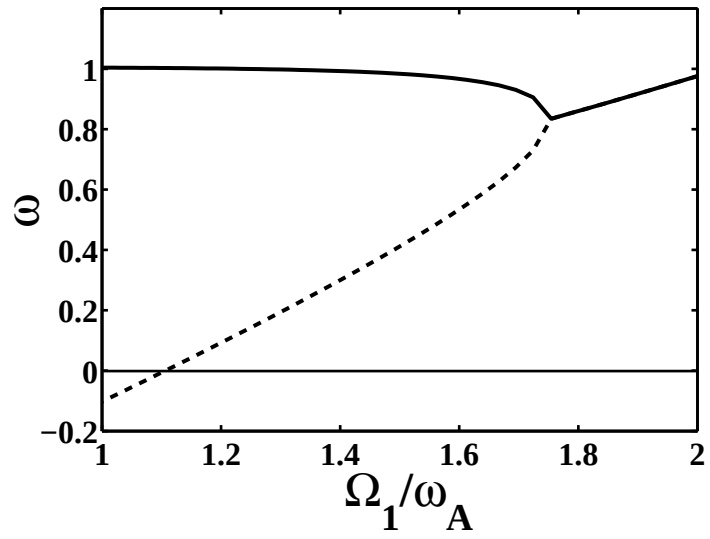

(b) Frequency (in units of Ω_1)

Figure 3.11: Dependencies of energy and frequency on the ratio Ω_1/ω_A for two inner eigen-modes in the case $m = 1$.

From our analysis it turns out that the growth rate of axisymmetric MRI is quite sensitive to the device parameters. For example, the axisymmetric MRI is suppressed for all $k_z > k_z^{cr}(m = 0)$, while the unstable modes with $m \neq 0$ still exist.

It was found that the threshold value of velocity decreases for large azimuthal numbers as $\sim 1/m$ (3.36). Consequently, in the frame of ideal MHD it is always easier to excite unstable non-axisymmetric MRI modes (though they have lower instability growth rate). The calculation of the energy of eigen-modes in such a system shows that this non-axisymmetric MRI can be explained as a coupling of originally stable positive and negative energy waves.

Chapter 4

Spectral stability of electrically driven flow in an annular channel: dissipative MHD

In this chapter, the results of spectral stability study of electrically driven rotation with $\Omega(R) \propto 1/R^2$ in the frame of dissipative MHD model are presented. It is shown that such flow can be destabilized through the mechanism of MRI if the velocity exceeds some instability threshold, which is determined by non-axisymmetric modes with large azimuthal numbers m.

A number of similar studies was performed by different researchers [45,50,51,53–55,109], who considered the stability of more general rotation profile $\Omega(R) = a+b/R^2$. The major part of these studies is restricted to the case of axisymmetric modes (with azimuthal mode-numbers $m = 0$) [45, 50, 51], which are known to have the largest growth rate of MRI. Numerical analysis of non-axisymmetric modes with small m [54, 55] shows that they can have lower instability threshold (lower critical values of the Reynolds number Re), so that they might be easier to excite in real experiment. For electrically driven flow it was found [103] that in ideal MHD the MRI threshold decreases with m as $\mathrm{Re}_{cr} \propto 1/m$ (3.37). Therefore, the most dangerous modes in such flow are those with larger m (though they have smaller instability growth rate).

The material of the present chapter suggest that overall stability of the flow in a finite height circular channel is determined by dissipative perturbations with large azimuthal numbers m. Our results are compared with available experimental data.

It appears that the results from the Grenoble experiment [110] can be explained by the MRI of dissipative non-axisymmetric modes.

4.1 Statement of the problem

4.1.1 Model and equations

We consider the spectral stability of electrically driven flow of liquid metal in the geometry relevant to the MRI experiment (Fig. 1.2); more specifically, we are interested in the analysis of instability threshold for such flow. As in Chapter 3, we neglect all boundary layers and assume that the fluid rotates in the uniform axial magnetic field $\mathbf{B}_e = B_0\mathbf{e}_z$, with equilibrium velocity $\mathbf{V}_e = R\Omega(R)\mathbf{e}_\varphi$, where $\Omega(R) = M_0/R^2$ throughout the cross-section of the channel. The equilibrium angular momentum of the velocity M_0 is determined by the total electric current I_0 passing through the channel (2.39):

$$M_0 = \frac{I_0}{4\pi\sqrt{\rho\sigma\nu}},$$

where ρ, σ and ν are fluid density, electric conductivity and kinematic viscosity, respectively.

We use dissipative incompressible MHD equations in non-dimensional form (1.20)-(1.23), taking as a unit of length the half-height of the channel $L = H/2$, as a unit of magnetic field the external field $B = B_0$ and as a unit of velocity a quantity $V = M_0/L$. Linearization of these equations near the equilibrium state yields:

$$\begin{aligned}
\nabla\cdot\delta\mathbf{v} &= 0, && (4.1)\\
\frac{\partial}{\partial\tau}\delta\mathbf{v} &= -(\mathbf{v}_e\cdot\nabla)\delta\mathbf{v} - (\delta\mathbf{v}\cdot\nabla)\mathbf{v}_e - \nabla\delta p + && (4.2)\\
&+ \frac{\mathrm{Ha}^2}{\mathrm{Re}_m\mathrm{Re}}(\mathbf{b}_e\cdot\nabla)\delta\mathbf{b} + \frac{\mathrm{Ha}^2}{\mathrm{Re}_m\mathrm{Re}}(\delta\mathbf{b}\cdot\nabla)\mathbf{b}_e + \frac{1}{\mathrm{Re}}\nabla^2\delta\mathbf{v},\\
\nabla\cdot\delta\mathbf{b} &= 0, && (4.3)\\
\frac{\partial}{\partial\tau}\delta\mathbf{b} &= \nabla\times(\mathbf{v}_e\times\delta\mathbf{b}) + \nabla\times(\delta\mathbf{v}\times\mathbf{b}_e) + \frac{1}{\mathrm{Re}_m}\nabla^2\delta\mathbf{b}, && (4.4)
\end{aligned}$$

where the Hartmann, Reynolds and magnetic Reynolds numbers are

$$\mathrm{Ha} = \frac{HB_0}{2c}\sqrt{\frac{\sigma}{\rho\nu}}, \quad \mathrm{Re} = \frac{M_0}{\nu}, \quad \mathrm{Re}_m = \frac{M_0}{\eta} = \frac{4\pi\sigma M_0}{c^2}. \tag{4.5}$$

All perturbations can be represented in the form $f(r,z)\exp(\gamma\tau + im\varphi)$ in the cylindrical system of coordinates $\{r,\varphi,z\}$. In order to simplify the notation we introduce vectors $\mathbf{u}$ and $\mathbf{h}$

$$\delta\mathbf{v} = \mathbf{u}, \quad \delta\mathbf{b} = \frac{\mathrm{Re}_m}{\mathrm{Ha}}\,\mathbf{h}.$$

As usual in incompressible hydrodynamics, we take the curl of equation (4.2) to remove the unknown gradient of pressure $\nabla\delta p$, so the system (4.1)-(4.4) is reduced to

$$\mathrm{Re}\,\gamma\,\boldsymbol{\omega} = -\frac{im\mathrm{Re}}{r^2}\,\boldsymbol{\omega} - \frac{2\mathrm{Re}}{r^2}\,\omega_r\mathbf{e}_\varphi + \mathrm{Ha}\frac{\partial}{\partial z}\,(\nabla\times\mathbf{h}) + \nabla^2\boldsymbol{\omega}, \tag{4.6}$$

$$\mathrm{Re}_m\,\gamma\,\mathbf{h} = -\frac{im\mathrm{Re}_m}{r^2}\,\mathbf{h} - \frac{2\mathrm{Re}_m}{r^2}\,h_r\mathbf{e}_\varphi + \mathrm{Ha}\frac{\partial}{\partial z}\,\mathbf{u} + \nabla^2\mathbf{h}, \tag{4.7}$$

where $\boldsymbol{\omega} = \nabla\times\mathbf{u}$ is the perturbation of the vorticity. Note that the r and φ components of these equations are enough to find the full solution (z-components can be deduced from $\nabla\cdot\boldsymbol{\omega} = 0$ and $\nabla\cdot\mathbf{h} = 0$).

The incompressibility condition $\nabla\cdot\mathbf{u} = 0$ is automatically satisfied by assuming two velocity stream-functions W and Y:

$$\mathbf{u} = \frac{1}{r}\nabla(rW)\times\mathbf{e}_\varphi + \nabla Y\times\mathbf{e}_r. \tag{4.8}$$

The system (4.6), (4.7) can be rewritten in component form

$$\mathrm{Re}\,\gamma\,\omega_r = \hat{\Delta}\omega_r - \frac{2im}{r^2}\,\omega_\varphi - \frac{im\mathrm{Re}}{r^2}\,\omega_r + \tag{4.9}$$
$$+ \mathrm{Ha}\left[\frac{m^2}{r^2}\,h_\varphi - \frac{\partial^2 h_\varphi}{\partial z^2} - \frac{im}{r^2}\left(r\frac{\partial h_r}{\partial r} + h_r\right)\right],$$

$$\mathrm{Re}\,\gamma\,\omega_\varphi = \hat{\Delta}\omega_\varphi + \frac{2im}{r^2}\,\omega_r - \frac{im\mathrm{Re}}{r^2}\,\omega_\varphi - \frac{2\mathrm{Re}}{r^2}\,\omega_r + \tag{4.10}$$
$$+ \mathrm{Ha}\left[\frac{\partial^2 h_r}{\partial r^2} + \frac{1}{r}\,\frac{\partial h_r}{\partial r} - \frac{h_r}{r^2} + \frac{\partial^2 h_r}{\partial z^2} + \frac{im}{r^2}\left(r\frac{\partial h_\varphi}{\partial r} - h_\varphi\right)\right],$$

$$\mathrm{Re}_m\,\gamma\,h_r = \hat{\Delta}h_r - \frac{2im}{r^2}\,h_\varphi - \frac{im\mathrm{Re}_m}{r^2}\,h_r - \mathrm{Ha}\frac{\partial^2 W}{\partial z^2}, \tag{4.11}$$

$$\mathrm{Re}_m\,\gamma\,h_\varphi = \hat{\Delta}h_\varphi + \frac{2im}{r^2}\,h_r - \frac{im\mathrm{Re}_m}{r^2}\,h_\varphi - \frac{2\mathrm{Re}_m}{r^2}\,h_r + \mathrm{Ha}\frac{\partial^2 Y}{\partial z^2}, \tag{4.12}$$

where the modified Laplacian $\hat{\Delta}$ is

$$\hat{\Delta} = \frac{\partial^2}{\partial r^2} + \frac{1}{r}\frac{\partial}{\partial r} + \frac{\partial^2}{\partial z^2} - \frac{1+m^2}{r^2},$$

and the components of the vorticity $\boldsymbol{\omega}$ are expressed through the stream functions W and Y

$$\omega_r = -\frac{\partial^2 Y}{\partial z^2} + \frac{m^2}{r^2}Y + \frac{im}{r^2}\left(r\frac{\partial W}{\partial r} + W\right), \tag{4.13}$$

$$\omega_\varphi = -\frac{\partial^2 W}{\partial r^2} - \frac{1}{r}\frac{\partial W}{\partial r} + \frac{W}{r^2} - \frac{\partial^2 W}{\partial z^2} + \frac{im}{r^2}\left(r\frac{\partial Y}{\partial r} - Y\right). \tag{4.14}$$

4.1.2 Boundary conditions

Proper boundary conditions should be specified prior to solving the system (4.9)-(4.14). In the flow of a viscous fluid, all velocity components vanish at the rigid walls, i. e.,

$$\mathbf{u}|_{r=r_1,r_2} = 0, \quad \mathbf{u}|_{z=\pm 1} = 0,$$

which results in

$$Y|_{r=r_1,r_2} = 0, \quad Y|_{z=\pm 1} = 0, \quad \left.\frac{\partial Y}{\partial z}\right|_{z=\pm 1} = 0, \tag{4.15}$$

$$W|_{r=r_1,r_2} = 0, \quad W|_{z=\pm 1} = 0, \quad \left.\frac{\partial (rW)}{\partial r}\right|_{r=r_1,r_2} = 0, \quad \left.\frac{\partial W}{\partial z}\right|_{z=\pm 1} = 0. \tag{4.16}$$

The boundary conditions for the magnetic field are determined by the conductivity of the walls. In an MRI experiment with electrically driven flow, the side walls of the channel can be considered perfect conducting (Fig. 2.1). At the surface of the perfect conductor the time-varying normal component of magnetic field as well as the tangential components of electric current should be zero. This means

$$h_r|_{r=r_1,r_2} = 0, \quad \left.\frac{\partial (rh_\varphi)}{\partial r}\right|_{r=r_1,r_2} = 0. \tag{4.17}$$

The other two walls (Hartmann walls) are electrical insulators. To find the correct boundary conditions in this case one has to solve the equations for magnetic field both in the fluid and in the insulating walls and then match the solutions at the

surface. For simplicity we assume that the perturbed components of the field are zero at these walls, i. e.,

$$h_r|_{z=\pm 1} = 0, \quad h_\varphi|_{z=\pm 1} = 0, \tag{4.18}$$

which guarantees the absence of the normal component of the current at the surface of the insulator.

The system (4.9)-(4.14) with boundary conditions (4.15)-(4.18) constitutes an eigen-value problem (γ is eigen-value), which can be solved numerically. It should be stressed here that in the present study we consider the channel of finite height and do not apply the Fourier transformation in z-direction since it is not consistent with boundary conditions (4.15), (4.16); this is a substantial difference of our stability analysis from previous studies.

4.2 Analytical results

4.2.1 Local approximation

The approximate analytical solution to the system (4.6), (4.7) can be found by means of the so-called *local approximation*. In this approximation all unknown functions are assumed to have radial dependence of the form $\exp(ik_r r)$ with radial wave-number k_r being sufficiently large so that, $k_r r \gg 1$ and $\partial/\partial r \sim k_r$[1]. Assuming also that z-dependence has the form $\exp(ik_z z)$, one obtains from (4.6), (4.7):

$$(\mathrm{Re}\,\bar{\gamma} + k^2)\boldsymbol{\omega} = -\frac{2\mathrm{Re}}{r^2}\,\omega_r \mathbf{e}_\varphi - k_z \mathrm{Ha}\mathbf{k}\times\mathbf{h}, \tag{4.19}$$

$$(\mathrm{Re}_m\,\bar{\gamma} + k^2)\mathbf{h} = -\frac{2\mathrm{Re}_m}{r^2}\,h_r \mathbf{e}_\varphi + ik_z \mathrm{Ha}\mathbf{u}, \tag{4.20}$$

where

$$k^2 = \mathbf{k}^2 = k_r^2 + k_\varphi^2 + k_z^2, \quad k_\varphi = \frac{m}{r},$$

$\mathbf{k}$ is wave-vector

$$\mathbf{k} = k_r \mathbf{e}_r + k_\varphi \mathbf{e}_\varphi + k_z \mathbf{e}_z,$$

[1] A particular case of local approximation for second-order differential equation is referred to as the WKB approximation; it is considered in Section 3.2.

and

$$\bar{\gamma} = \gamma + \frac{im}{r^2}$$

is the Doppler shifted eigen-value. Vorticity $\boldsymbol{\omega}$ can be expressed through components of the velocity $\mathbf{u}$:

$$\boldsymbol{\omega} = i\mathbf{k} \times \mathbf{u} = i \begin{pmatrix} k_\varphi u_z - k_z u_\varphi \\ k_z u_r - k_r u_z \\ k_r u_\varphi - k_\varphi u_r \end{pmatrix} = \frac{i}{k_z} \begin{pmatrix} -k_r k_\varphi u_r - (k_\varphi^2 + k_z^2) u_\varphi \\ (k_r^2 + k_z^2) u_r + k_r k_\varphi u_\varphi \\ k_r u_\varphi - k_\varphi u_r \end{pmatrix}, \qquad (4.21)$$

where the incompressibility condition is used, $\mathbf{k} \cdot \mathbf{u} = 0$. An analogous expression is obtained for the quantity $\mathbf{k} \times \mathbf{h}$. Finally, the r and φ components of equations (4.19), (4.20) yield:

$$\begin{aligned}
0 &= i(\mathrm{Re}\,\bar{\gamma} + k^2)[k_r k_\varphi u_r + (k_\varphi^2 + k_z^2) u_\varphi] + k_z \mathrm{Ha}[k_r k_\varphi h_r + (k_\varphi^2 + k_z^2) h_\varphi], \quad (4.22) \\
0 &= i(\mathrm{Re}\,\bar{\gamma} + k^2)[(k_r^2 + k_z^2) u_r + k_r k_\varphi u_\varphi)] - \frac{2i\mathrm{Re}}{r^2}\,[k_r k_\varphi u_r + (k_\varphi^2 + k_z^2) u_\varphi] + \\
&+ k_z \mathrm{Ha}[(k_r^2 + k_z^2) h_r + k_r k_\varphi h_\varphi], \qquad (4.23) \\
0 &= (\mathrm{Re}_m\,\bar{\gamma} + k^2) h_r - i k_z \mathrm{Ha} u_r, \qquad (4.24) \\
0 &= (\mathrm{Re}_m\,\bar{\gamma} + k^2) h_\varphi + \frac{2\mathrm{Re}_m}{r^2}\,h_r - i k_z \mathrm{Ha} u_\varphi. \qquad (4.25)
\end{aligned}$$

These equations should be considered as the homogenous linear system for unknowns u_r, u_φ, h_r and h_φ. In order for this system to have a nontrivial solution, its determinant must be zero. Thus, we obtain

$$4\mathrm{Re}_m \mathrm{Re}\,\mathrm{Ha}^2 (k_\varphi^2 + k_z^2)^2 = k^2 r^4 [k_z^2 \mathrm{Ha}^2 + (\mathrm{Re}_m \bar{\gamma} + k^2)(\mathrm{Re}\bar{\gamma} + k^2)]^2. \qquad (4.26)$$

According to equation (4.26), the flow becomes unstable (there is a root with $Re\ \bar{\gamma} > 0$) if the Reynolds number exceeds the threshold value determined by

$$\mathrm{Re}_{cr} = \frac{r^2 k}{2\sqrt{\mathrm{Pr}_m}\,(k_\varphi^2 + k_z^2)} \left[k_z^2 \mathrm{Ha} + \frac{k^4}{\mathrm{Ha}} \right]. \qquad (4.27)$$

The last term in the square brackets of (4.27) is related to dissipative effects (the resistivity and the viscosity). At large Hartmann numbers, when this term is unimportant, the ideal marginal stability limit is obtained

$$\mathrm{Re}_{cr} = \frac{r^2 k k_z^2 \mathrm{Ha}}{2\sqrt{\mathrm{Pr}_m}\,(k_\varphi^2 + k_z^2)}. \qquad (4.28)$$

For non-axisymmetric modes with large azimuthal wave-number k_φ, equation (4.28) has the asymptotic behavior

$$\mathrm{Re}_{cr} = \frac{r^2 k_z^2 \mathrm{Ha}}{2k_\varphi \sqrt{\mathrm{Pr}_m}}, \tag{4.29}$$

which is not correct (compare with (3.37)). This mistake is a result of an improper use of the local approximation. As discussed in [111], the failure of the local approximation in the case of non-axisymmetric modes is due to the rapid shearing that occurs between even nearby locations. Here the local approximation is no substitute for solving the full eigen-value problem.

Nonetheless, because they are not sheared the local approximation works well for axisymmetric disturbances with $k_\varphi = 0$. Taking $k_\varphi = 0$ in (4.28), one recovers the instability threshold for ideal axisymmetric modes (3.32). In dissipative MHD, the axisymmetric instability threshold is given by

$$\mathrm{Re}_{cr} = \frac{r^2 k}{2\sqrt{\mathrm{Pr}_m}} \left[\mathrm{Ha} + \frac{k^4}{k_z^2 \mathrm{Ha}} \right], \tag{4.30}$$

i. e., the dissipation has a stabilizing effect on axisymmetric MRI, which is confirmed by numerical simulations.

4.2.2 Scaling laws for the MRI threshold

The principal dependencies of instability threshold on the system parameters can be obtained analytically from the eigen-value problem (4.6), (4.7). We consider here two cases: the ideal MHD limit and the limit of small magnetic Prandtl numbers. In both cases non-axisymmetric modes with large azimuthal numbers are assumed ($m \gg 1$) for which

$$\nabla^2 \sim -k^2 \sim -\frac{m^2}{r^2}.$$

Ideal MHD limit

In ideal MHD, the last two terms in equations (4.6), (4.7) can be neglected. This corresponds to the limit

$$\mathrm{Re} \gg \frac{m}{\mathrm{Pr}_m} \tag{4.31}$$

for Prandtl numbers $\mathrm{Pr}_m < 1$. Also we neglect the second terms on the right hand sides of both equations (it is justified by the condition $m \gg 1$). After the renormalization

$$\gamma = m\tilde{\gamma}, \quad \mathbf{h} = \frac{ik_z\mathrm{Ha}}{m\mathrm{Re}_m}\,\tilde{\mathbf{h}},$$

the equations (4.6), (4.7) take the form:

$$\tilde{\gamma}\,\boldsymbol{\omega} = -\frac{i}{r^2}\,\boldsymbol{\omega} - \frac{k_z^2\mathrm{Ha}^2}{m^2\mathrm{Re}_m\mathrm{Re}}\,\nabla\times\tilde{\mathbf{h}}, \tag{4.32}$$

$$\tilde{\gamma}\,\tilde{\mathbf{h}} = -\frac{i}{r^2}\,\tilde{\mathbf{h}} + \mathbf{u}. \tag{4.33}$$

The solution to this system is determined by just one parameter, namely, the combination

$$\frac{k_z^2\mathrm{Ha}^2}{m^2\mathrm{Re}_m\mathrm{Re}}.$$

Therefore, the instability threshold can be represented as

$$\mathrm{Re}_{cr} = C\frac{k_z\mathrm{Ha}}{m\sqrt{\mathrm{Pr}_m}}, \tag{4.34}$$

where C is some constant. This is exactly the dependence (3.37) with C being

$$C = \frac{2r_1^2}{(1 - r_1^2/r_2^2)}.$$

Limit of zero magnetic Prandtl number

This limit is valid for most liquid metals with $\mathrm{Pr}_m \ll 1$. Since $\mathrm{Re}_m = \mathrm{Pr}_m\mathrm{Re}$, we can neglect all terms with Re_m in equation (4.7). The more rigorous condition for that is

$$\mathrm{Re} \ll \frac{m}{\mathrm{Pr}_m}. \tag{4.35}$$

From the physical point of view, this limit corresponds to a highly resistive fluid, in which the changes of the magnetic field follow the changes of the fluid velocity instantly. The renormalization of the quantities in this case is

$$\gamma = \frac{m^2}{\mathrm{Re}}\,\tilde{\gamma}, \quad \mathbf{h} = \frac{ik_z\mathrm{Ha}}{m^2}\,\tilde{\mathbf{h}},$$

and system (4.6), (4.7) is reduced to

$$\tilde{\gamma}\,\boldsymbol{\omega} = -\frac{1}{r^2}\,\boldsymbol{\omega} - \frac{\mathrm{Re}}{m}\frac{i}{r^2}\,\boldsymbol{\omega} - \frac{k_z^2 \mathrm{Ha}^2}{m^4}\,\nabla \times \tilde{\mathbf{h}}, \tag{4.36}$$

$$0 = -\frac{1}{r^2}\,\tilde{\mathbf{h}} + \mathbf{u}. \tag{4.37}$$

The solution now depends on two parameters

$$\frac{\mathrm{Re}}{m}, \quad \frac{k_z \mathrm{Ha}}{m^2},$$

and the threshold of instability is expressed as

$$\mathrm{Re}_{cr} = m f\left(\frac{k_z \mathrm{Ha}}{m^2}\right), \tag{4.38}$$

where f is some function, which can be found numerically.

4.3 Experimental results

In this Section we outline the results of an experimental study of the flow of a liquid metal (mercury) in an annular channel, which has been performed in the Grenoble High Magnetic Field Laboratory (France) [110]. Originally this experiment was developed to investigate the stability of Hartmann layers. However, it appears that its design completely corresponds to the design of an MRI experiment with electrically driven flow (Fig. 1.2). The parameters of the Grenoble and Obninsk [49] experiments are given in Tables 4.1 and 2.1, respectively. It should be mentioned that the experimental results are not available from the Obninsk MRI experiment at present time.

In the Grenoble experiment, a well-marked transition to turbulence was found when the ratio of Reynolds number to Hartmann number, R = Re/Ha, exceeded the critical value $\mathrm{R}_c^{Gr} \approx 380$ (superscript Gr denotes the quantities taken from [110]). This value of R_c^{Gr} was also valid for the inverse process of laminarization without a visible hysteresis and for intensities of the magnetic field between 1 and 13 T (the corresponding Hartmann numbers are $\mathrm{Ha}^{Gr} = 130 - 1690$). In Fig. 4.1, the

Table 4.1: Parameters of the Grenoble experiment

Parameter	Value	Corresponding non-dimensional parameter	Value of non-dimensional parameter
Geometry of the channel			
Inner radius, R_1	4 cm	$r_1 = R_1/L$	$r_1 = 8$
Outer radius, R_2	5 cm	$r_2 = R_2/L$	$r_2 = 10$
Height, $H = 2L$	1 cm	$h = H/L$	$h = 2$
Properties of liquid mercury			
Density, ρ	13.55 g/cm^3	–	–
Kinematic viscosity, ν	$1.14{\cdot}10^{-3}$ cm^2/s	$\mathrm{Pr}_m = \nu/\eta$	$\mathrm{Pr}_m = 1.49 \cdot 10^{-7}$
Resistivity, η	$7.7 \cdot 10^3$ cm^2/s		
Parameters of the experiment			
Total current, I_0	$0 - 400$ A	$\mathrm{Re} = M_0/\nu = I_0/(\nu c\sqrt{4\pi\rho\mathrm{Pr}_m}) = 2800 \cdot I_0[\mathrm{A}]$	$\mathrm{Re} = 0 - 1.1 \cdot 10^6$
Typical angular momentum of mercury, $M_0 = I_0/(c\sqrt{4\pi\rho\mathrm{Pr}_m})$	$0 - 1300$ cm^2/s	–	–
Velocity of mercury at R_1, $V_1 = M_0/R_1$	$0 - 320$ cm/s	–	–
Magnetic field, B_0	$0 - 13$ T	$\mathrm{Ha} = HB_0/\sqrt{16\pi\rho\nu\eta} = 130{\cdot}H[\mathrm{cm}]{\cdot}B_0{\cdot}[\mathrm{T}]$	$\mathrm{Ha} = 0 - 1690$
Alfven velocity, $V_A = B_0/\sqrt{4\pi\rho}$	$0 - 10^4$ cm/s	–	–

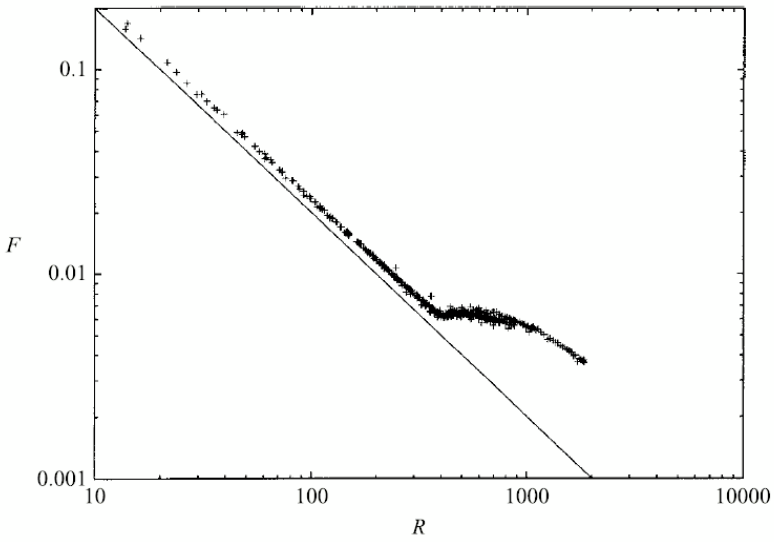

Figure 4.1: Grenoble experimental results: friction factor F vs. $\mathrm{R}^{Gr} = \mathrm{Re}^{Gr}/\mathrm{Ha}^{Gr}$ for discrete values of the current between 0 and 400 A, and magnetic fields between 1 and 13T ($\mathrm{Ha}^{Gr} = 130 - 1690$). The straight line corresponds to the friction factor for laminar flow. Figure is taken from [110].

experimental values of the so-called *friction factor* F are plotted as a function of R^{Gr}. The friction factor is defined as

$$F = \frac{I_0 B_0}{c\rho V_m^2 \pi (R_1 + R_2)}, \tag{4.39}$$

where V_m is the mean velocity in the flow, which was determined from the measurements of the voltage U, and the intensity of the injected electric current I_0:

$$V_m = \frac{cU}{(R_2 - R_1)B_0} - \frac{cI_0}{2\pi\sigma(R_2 - R_1)HB_0} \ln \frac{R_2}{R_1}. \tag{4.40}$$

This formula follows from the integral of Ohms law (1.13) over the cross-section of the channel [59].

The Hartmann and Reynolds numbers in [110] are defined as

$$\mathrm{Ha}^{Gr} \equiv \mathrm{Ha} = \frac{HB_0}{2c}\sqrt{\frac{\sigma}{\rho\nu}}, \quad \mathrm{Re}^{Gr} = \frac{HV_m}{\nu}, \tag{4.41}$$

so the definition of the Reynolds number is different from (4.5) used in our calculations[2]. In order to find the relation between Re^{Gr} and Re, we assume that

[2]We should note that the Hartmann number defined in equation (2.4) in Ref. [110] differs from the Hartmann number used in the figures of paper [110] by a factor of 2.

the equilibrium flow is purely azimuthal and depends on the radial coordinate as[3] $V_\varphi = M_0/R$. Then the mean velocity is

$$V_m = \frac{M_0}{R_2 - R_1} \int_{R_1}^{R_2} \frac{dR}{R} = \frac{M_0}{R_2 - R_1} \ln \frac{R_2}{R_1}. \tag{4.42}$$

This leads to the relation

$$\mathrm{Re}^{Gr} = \frac{HV_m}{\nu} = \frac{HM_0}{\nu(R_2 - R_1)} \ln \frac{R_2}{R_1} \approx 0.22\,\mathrm{Re},$$

and

$$\mathrm{R}_c = \frac{\mathrm{Re}}{\mathrm{Ha}} \approx \frac{1}{0.22}\mathrm{R}_c^{Gr} \approx 1700. \tag{4.43}$$

The critical value R_c^{Gr} obtained in the Grenoble experiment is two orders of magnitude smaller than $\mathrm{R}_c^{\mathrm{Ha}} \approx 50,000$ predicted by the linear stability theory for Hartmann layers [112]. A possible explanation to this paradox is discussed in papers [113, 114], where a complicated two-step transition scenario to turbulence in the Hartmann layers is assumed. In these papers the radial dependence of the velocity profile in the main part of the flow is completely disregarded. However, in our present consideration, it is suggested that the magnetized flow can be destabilized via the MRI mechanism.

4.4 Numerical results

Equations (4.9)-(4.14) with boundary conditions (4.15)-(4.18) constitute an eigenvalue problem with γ being an unknown eigenvalue. A solution to this problem was sought by expanding unknown functions ω_r, ω_φ, Y, W, h_r and h_φ in terms of either odd or even polynomials in z (up to $N_z = 8$), and by the discretization of the system (4.9)-(4.14) in terms of finite differences in the r-direction (up to $N_r = 50$). Then this system was reduced to a large $(4N_rN_z \times 4N_rN_z)$ matrix eigenvalue problem which was solved using the standard numerical methods of MATLAB.

[3]The conditions for this assumption are discussed in Section 2.5

The following numerical procedure was performed for two values of magnetic Prandtl number corresponding to mercury (Hg) and liquid sodium (Na) and for the geometries of both Grenoble and Obninsk experiments (Tables 4.1 and 2.1). Taking a value for the azimuthal number from the array $m = 0 - 200$, we scanned through a range of values of Re and Ha, finding the maximal growth rate for given parameters. For each value of Ha, we determined the value of Re that yields a marginal stability, i.e., corresponds to the zero maximal growth rate $Re\ \gamma = 0$. Thus we obtained the marginal stability curves at the plane $\mathrm{Re} - \mathrm{Ha}$ (Fig. 4.2, 4.3).

One can see from Fig. 4.2 and 4.3 that the instability threshold is determined by different azimuthal modes at different Hartmann numbers Ha. For larger Ha, the corresponding m is larger. In fact, a simple scaling law can be obtained for large m: $\mathrm{Ha} \propto m^2$, which is also confirmed by equation (4.38). The stability curves of axisymmetric modes with $m = 0$ are not shown because they are situated at much higher values of Re. Therefore, the non-axisymmetric modes play the decisive role for excitation of MRI in electrically driven flow.

It is worth noting here that the marginal stability curves do not practically depend on the magnetic Prandtl number, Pr_m, of the fluid; they are determined only by the geometry of the channel. This is true for non-axisymmetric modes in the limit $\mathrm{Pr}_m \ll 1$ which is common for most liquid metals. In this case, a good approximation for the instability threshold can be achieved by neglecting all the terms containing Pr_m in the equation (4.7) and reducing the system (4.6), (4.7) to one vector equation with hydrodynamical variables (see Section 4.2.2). Such an approach is not applicable for axisymmetric modes in axial magnetic field [115].

In ideal MHD, the MRI threshold to a significant degree is affected by singularities inherent in the eigenvalue problem [116]. In the incompressible limit, the MRI of non-axisymmetric modes is associated with one set of these singularities – the so-called Alfven resonances (Section 3.3). Within the frame of the MHD model considered here, the Alfven resonances are removed by dissipative effects (resistivity and viscosity). An important consequence of this is that the dissipative stability threshold for non-axisymmetric modes appears to be lower than the ideal one, i.e.

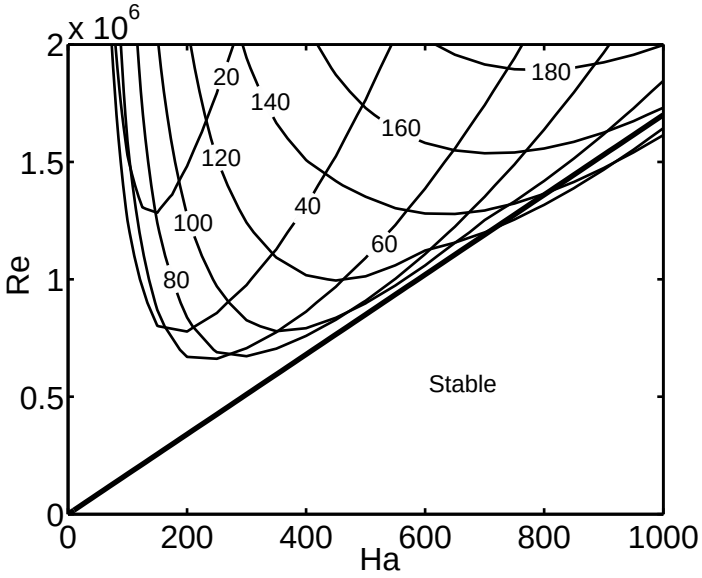

Figure 4.2: Calculated marginal stability curves for the Grenoble experiment. Azimuthal mode numbers m are shown. Straight line corresponds to the transition to turbulence observed in experiment, $Re = 1,700\text{Ha}$.

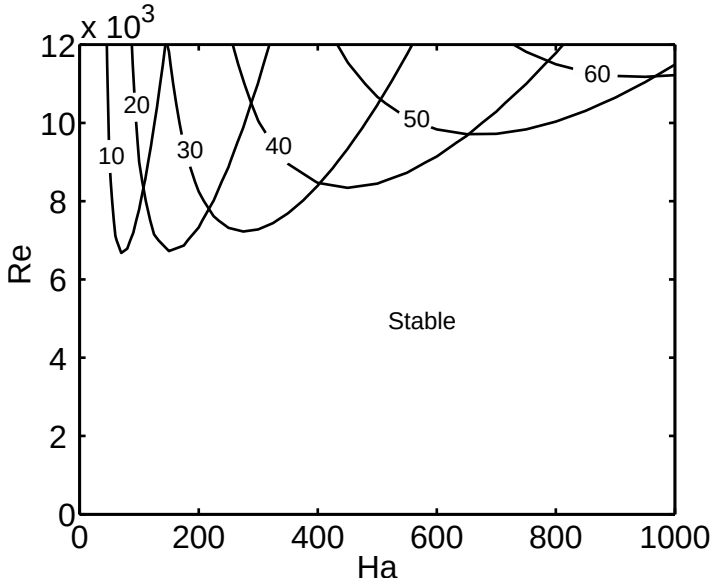

Figure 4.3: Calculated marginal stability curves for the Obninsk experiment. Azimuthal mode numbers m are shown.

the dissipation (mainly the resistivity) has destabilizing effect on the ideal modes. Such an effect can be explained by the existence of modes with negative energy in the system, which are destabilized in the presence of dissipation (Section 3.5).

Our main observation is that the MRI threshold of electrically driven flow is formed by the envelope of all marginal stability curves corresponding to modes with different azimuthal numbers m. The shape of the envelope depends on the particular geometry of the channel (see Fig. 4.2 and 4.3). In Fig. 4.2, the envelope is close to the form $\mathrm{Re} \propto \mathrm{Ha}$ when $\mathrm{Ha} \gtrsim 300$. This means that an instability should be excited in this geometry if the ratio $\mathrm{R} = \mathrm{Re}/\mathrm{Ha}$ exceeds some critical value R_c. As mentioned above, this effect was actually detected experimentally [110]. The line associated with the experimental value of R_c (4.43) is also plotted in Fig. 4.2. As one can see, the calculated threshold of MRI is in good agreement with experimental results.

A natural question arises: what do we observe in reality – MRI or Hartmann layer instability? A strong argument for MRI is the comparison of respective linear instability thresholds: the MRI threshold found in our calculations corresponds to that measured in the Grenoble experiment and is two orders of magnitude smaller than instability threshold of Hartmann layers [112]. Also it is evident that in the presence of a global (affecting the entire flow) robust linear instability, such as MRI, the nonlinear effects in Hartmann layers [113, 114] are unlikely to play the major role in destabilizing the flow. The global character of MRI is illustrated in Fig. 4.4, where a typical marginally stable eigenfunction u_φ (azimuthal perturbation of velocity) is shown.

4.5 Conclusions

In this Chapter it was shown that the instability threshold of electrically driven liquid metal in the plane $\mathrm{Ha} - \mathrm{Re}$ is determined by the MRI of global non-axisymmetric modes with large azimuthal mode numbers m. For a larger Hartmann number, the corresponding m is larger and the approximate scaling can be obtained from dependence (4.38).

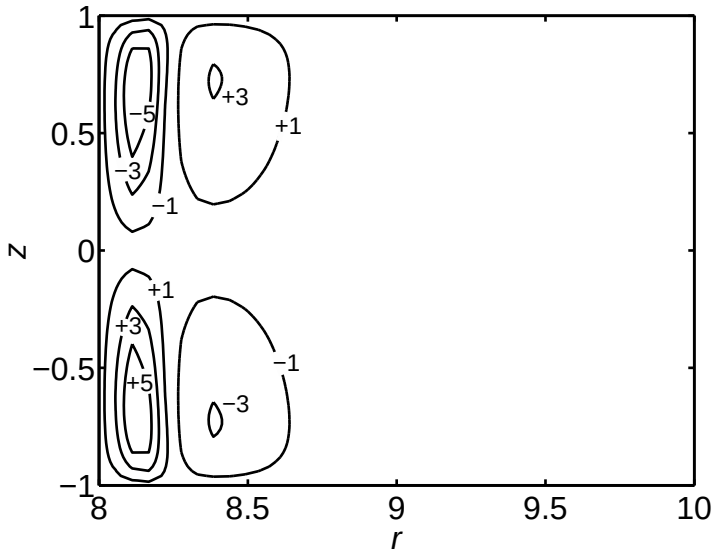

Figure 4.4: Calculated contours of the marginally stable eigenfunction v_φ (azimuthal perturbation of velocity) in the cross-section of the Grenoble channel at $m = 100$, Ha $= 500$, Re $= 9 \cdot 10^5$. Magnitude is shown in arbitrary units.

The MRI threshold does not depend on the type of conducting fluid as long as the magnetic Prandtl number of the fluid is small Pr $\ll 1$; it is determined completely by the geometry of the channel. It should be also noted that the instability threshold of dissipative non-axisymmetric modes is lower than the instability threshold of modes in ideal MHD (the critical Reynolds numbers are lower). This can be explained by the dissipative destabilization of non-axisymmetric negative energy waves which are always present in the system.

The MRI threshold calculated for the geometry of the Grenoble experiment agrees well with the critical ratio R_c found in this experiment. These results suggest that the transition to turbulence observed in the experiment [110] is associated with non-axisymmetric MRI in electrically driven flow. The material of the present chapter proposes that experiments with electrically driven flow of liquid metals are effective ways of detecting and studying MRI.

Chapter 5

Formal stability of ideal MHD flows

In the present chapter, a general variational method is developed for the study of the formal stability of flows in the frame of ideal compressible MHD. It is shown that the linearized dynamics of an ideal fluid possesses an infinite set of integrals of motion. The inclusion of one or several such integrals in Arnold's method (Theorem 1.7) makes it possible to obtain a sufficient condition for the stability of MHD flows. The condition appears to be softer (closer to a necessary condition) than previously known conditions. An analytical example is presented to confirm the fruitfulness of the developed method.

5.1 Linearized equation of fluid dynamics. Energy principle

We consider a compressible conducting fluid in the frame of the ideal MHD model (see equations (1.6)-(1.10)):

$$\dot{\rho} = -\nabla \cdot (\rho \mathbf{V}), \tag{5.1}$$

$$\rho \dot{\mathbf{V}} = -\rho(\mathbf{V} \cdot \nabla)\mathbf{V} - \nabla P + \frac{1}{4\pi}(\nabla \times \mathbf{B}) \times \mathbf{B} - \rho \nabla \Phi, \tag{5.2}$$

$$\dot{P} = -\mathbf{V} \cdot \nabla P - \gamma P \nabla \cdot \mathbf{V}, \tag{5.3}$$

$$\dot{\mathbf{B}} = \nabla \times (\mathbf{V} \times \mathbf{B}), \quad \nabla \cdot \mathbf{B} = 0, \tag{5.4}$$

where the dot denotes a partial time derivative $\partial/\partial t$, and all other notations are standard: ρ, P and $\mathbf{V}$ are the density, pressure and velocity of the fluid, respectively; $\mathbf{B}$ is the total magnetic field. In this model, we also assume the presence of an

external potential force (such as gravity), given by the potential Φ; all the processes in the fluid are assumed to be adiabatic with the adiabatic index γ. All quantities in (5.1)-(5.4) are considered as functions of time and space, $f = f(t, \mathbf{R})$.

Taking $\partial/\partial t \to 0$ in the system (5.1)-(5.4), we obtain equations describing the general equilibrium state:

$$
\begin{aligned}
0 &= \nabla \cdot (\rho_e \mathbf{V}_e), && (5.5)\\
0 &= -\rho_e (\mathbf{V}_e \cdot \nabla)\mathbf{V}_e - \nabla P_e + \frac{1}{4\pi} (\nabla \times \mathbf{B}_e) \times \mathbf{B}_e - \rho_e \nabla \Phi, && (5.6)\\
0 &= \mathbf{V}_e \cdot \nabla P_e + \gamma P_e \nabla \cdot \mathbf{V}_e, && (5.7)\\
0 &= \nabla \times (\mathbf{V}_e \times \mathbf{B}_e), \quad \nabla \cdot \mathbf{B}_e = 0, && (5.8)
\end{aligned}
$$

where subscript e denotes the equilibrium quantities, $f_e = f_e(\mathbf{R})$. We should note that equations (5.5)-(5.8) allow for the existence of stationary flows in the MHD system.

In order to analyze the stability of the equilibrium state (5.5)-(5.8), we linearize MHD equations (5.1)-(5.4) near that state:

$$
\begin{aligned}
\delta\dot{\rho} &= -\nabla \cdot (\delta\rho \mathbf{V}_e) - \nabla \cdot (\rho_e \delta\mathbf{V}), && (5.9)\\
\delta\dot{\mathbf{V}} &= -\delta\rho (\mathbf{V}_e \cdot \nabla)\mathbf{V}_e - \rho_e (\delta\mathbf{V} \cdot \nabla)\mathbf{V}_e - \rho_e (\mathbf{V}_e \cdot \nabla)\delta\mathbf{V} - \nabla\delta P + && (5.10)\\
&+ \frac{1}{4\pi} (\nabla \times \delta\mathbf{B}) \times \mathbf{B}_e + \frac{1}{4\pi} (\nabla \times \mathbf{B}_e) \times \delta\mathbf{B} - \delta\rho \nabla\Phi,\\
\delta\dot{P} &= -\delta\mathbf{V} \cdot \nabla P_e - \mathbf{V}_e \cdot \nabla\delta P - \gamma\delta P \nabla \cdot \mathbf{V}_e - \gamma P_e \nabla \cdot \delta\mathbf{V}, && (5.11)\\
\delta\dot{\mathbf{B}} &= \nabla \times (\delta\mathbf{V} \times \mathbf{B}_e) + \nabla \times (\mathbf{V}_e \times \delta\mathbf{B}), \quad \nabla \cdot \delta\mathbf{B} = 0, && (5.12)
\end{aligned}
$$

Equations (5.9), (5.11) and (5.12) can be integrated by introducing the *Lagrangian displacement vector* $\boldsymbol{\xi}(t, \mathbf{R})$ [23], namely:

$$
\begin{aligned}
\delta\rho &= -\nabla \cdot (\rho_e \boldsymbol{\xi}), && (5.13)\\
\delta\mathbf{V} &= \dot{\boldsymbol{\xi}} + (\mathbf{V}_e \cdot \nabla)\boldsymbol{\xi} - (\boldsymbol{\xi} \cdot \nabla)\mathbf{V}_e, && (5.14)\\
\delta P &= -\boldsymbol{\xi} \cdot \nabla P_e - \gamma P_e \nabla \cdot \boldsymbol{\xi}, && (5.15)\\
\delta\mathbf{B} &= \nabla \times (\boldsymbol{\xi} \times \mathbf{B}_e). && (5.16)
\end{aligned}
$$

As a result we obtain the linearized equation of fluid dynamics, which follows from

equation (5.10):

$$\rho_e \ddot{\boldsymbol{\xi}} + 2\rho_e(\mathbf{V}_e \cdot \nabla)\dot{\boldsymbol{\xi}} - \mathbf{F}[\boldsymbol{\xi}] = 0, \tag{5.17}$$

where $\mathbf{F}[\boldsymbol{\xi}]$ is linearized force operator

$$\begin{aligned}
\mathbf{F}[\boldsymbol{\xi}] &= -\rho_e(\mathbf{V}_e \cdot \nabla)^2\boldsymbol{\xi} + \rho_e(\boldsymbol{\xi} \cdot \nabla)((\mathbf{V}_e \cdot \nabla)\mathbf{V}_e) + \nabla \cdot (\rho_e \boldsymbol{\xi})(\mathbf{V}_e \cdot \nabla)\mathbf{V}_e + \\
&+ \frac{1}{4\pi}\Big((\nabla \times (\nabla \times (\boldsymbol{\xi} \times \mathbf{B}_e))) \times \mathbf{B}_e + (\nabla \times \mathbf{B}_e) \times (\nabla \times (\boldsymbol{\xi} \times \mathbf{B}_e))\Big) + \\
&+ \nabla\Big(\boldsymbol{\xi} \cdot \nabla P_e + \gamma P_e \nabla \cdot \boldsymbol{\xi}\Big) + \nabla \cdot (\rho_e \boldsymbol{\xi}) \nabla \Phi.
\end{aligned} \tag{5.18}$$

As mentioned in Section 3.5, a number of formal properties of equation (5.17) can be established. The force operator $\mathbf{F}[\boldsymbol{\xi}]$ is Hermitian (self-adjoint), i. e.,

$$\int \boldsymbol{\eta} \cdot \mathbf{F}[\boldsymbol{\xi}]\, d^3\mathbf{R} = \int \boldsymbol{\xi} \cdot \mathbf{F}[\boldsymbol{\eta}]\, d^3\mathbf{R}, \tag{5.19}$$

while the second term in (5.17) is antisymmetric:

$$\int \rho_e \boldsymbol{\eta} \cdot (\mathbf{V}_e \cdot \nabla)\boldsymbol{\xi}\, d^3\mathbf{R} = -\int \rho_e \boldsymbol{\xi} \cdot (\mathbf{V}_e \cdot \nabla)\boldsymbol{\eta}\, d^3\mathbf{R}. \tag{5.20}$$

The dynamics described by equation (5.17) is conservative; this is verified by multiplying equation (5.17) by $\dot{\boldsymbol{\xi}}$ and integrating over the entire space. As a result, one obtains the energy conservation law in the form $\dot{E} = 0$, where the energy functional is

$$E(\dot{\boldsymbol{\xi}}, \boldsymbol{\xi}) = \frac{1}{2}\int \left(\rho_e \dot{\boldsymbol{\xi}}^2 - \boldsymbol{\xi} \cdot \mathbf{F}[\boldsymbol{\xi}]\right) d^3\mathbf{R}. \tag{5.21}$$

Treating the energy functional $E(\dot{\boldsymbol{\xi}}, \boldsymbol{\xi})$ as a Lyapunov functional candidate near the equilibrium state $\dot{\boldsymbol{\xi}}_e = 0$, $\boldsymbol{\xi}_e = 0$ and minimizing it over $\dot{\boldsymbol{\xi}}$, which contributes only to nonnegative kinetic energy, we arrive at the formal stability condition in the form

$$W(\boldsymbol{\xi}) \equiv -\frac{1}{2}\int \boldsymbol{\xi} \cdot \mathbf{F}[\boldsymbol{\xi}]\, d^3\mathbf{R} > 0. \tag{5.22}$$

This result is formulated in the form of a general theorem.

Theorem 5.1 (Energy principle) *If the change of the potential energy is positive for any small deviations of a conservative system from the equilibrium state, then such an equilibrium state is stable.*

The positive definiteness in condition (5.22) can be substituted by nonnegativity of the potential energy ($W \geq 0$), which, nevertheless, ensures spectral stability.

For static MHD equilibrium (with $\mathbf{V}_e = 0$), condition (5.22) obtained in [24] is not only sufficient, which is ensured by the Lyapunov theorem (Theorem 1.2), but also necessary for stability. In other words, if there is a perturbation $\boldsymbol{\xi}_-$ such that $W(\boldsymbol{\xi}_-) < 0$, then a solution of equation (5.17) can be constructed near the equilibrium position $\dot{\boldsymbol{\xi}} = 0$, $\boldsymbol{\xi} = 0$ that increases in time no slower than exponentially [78]. In the case $\mathbf{V}_e \neq 0$, condition (5.22) originally obtained in [23] is only sufficient, i.e., if it is not satisfied for some $\boldsymbol{\xi}$ nothing can be concluded about stability. Moreover, this condition can be practically satisfied only for the flow of fluid directed strictly along the magnetic field, i.e., $\mathbf{V}_e \| \mathbf{B}_e$ [23], or in cases reduced to this one by a special transformation [79]. Indeed, by representing $W(\boldsymbol{\xi})$ in the form

$$\begin{aligned} W(\boldsymbol{\xi}) \;\equiv\; & \frac{1}{2}\int\left(\frac{1}{4\pi}(\nabla\times(\boldsymbol{\xi}\times\mathbf{B}_e))^2 - \frac{1}{\rho_e}(\nabla\times(\boldsymbol{\xi}\times\rho_e\mathbf{V}_e))^2 + \right. \\ & + \frac{1}{4\pi}(\boldsymbol{\xi}\times\nabla(\boldsymbol{\xi}\times\mathbf{B}_e))\cdot(\nabla\times\mathbf{B}_e) - (\boldsymbol{\xi}\times\nabla(\boldsymbol{\xi}\times\rho_e\mathbf{V}_e))\cdot(\nabla\times\mathbf{V}_e) + \\ & + \frac{\mathbf{V}_e^2}{\rho_e^2}(\nabla\cdot(\rho_e\boldsymbol{\xi}))^2 + \left(\boldsymbol{\xi}\cdot\nabla\frac{\mathbf{V}_e^2}{2} - 2\mathbf{V}_e\cdot(\mathbf{V}_e\cdot\nabla)\boldsymbol{\xi}\right)\nabla\cdot(\rho_e\boldsymbol{\xi}) + \\ & + \left.(\boldsymbol{\xi}\cdot\nabla P_e)\nabla\cdot\boldsymbol{\xi} + \gamma P_e(\nabla\cdot\boldsymbol{\xi})^2 - \nabla\cdot(\rho_e\boldsymbol{\xi})(\boldsymbol{\xi}\cdot\nabla\Phi)\right)d^3\mathbf{R}, \end{aligned} \tag{5.23}$$

it is easy to see that the first two terms in equation (5.23) have the same structure but opposite signs. If the equilibrium flow of the fluid occurs at an angle to the magnetic field direction, then the sum of these terms can be easily made negative by choosing a test perturbation that is nearly uniform along the magnetic field lines $\mathbf{B}_e$ but noticeably varied along the streamlines. This quite obvious circumstance was considered in detail in [25]. Since these terms include the highest order derivatives of $\boldsymbol{\xi}$, then $W(\boldsymbol{\xi})$ does not satisfy even the necessary for positive definiteness Legendre condition. All these statements also evidently refer to flows of a usual fluid (in the absence of the magnetic field), where the stabilizing perturbation of magnetic energy is absent.

Due to these reasons, the application of the energy principle in the form (5.22) for the stability study of equilibria with MHD flows is quite restricted.

5.2 Formal stability of MHD flows

According to Arnold's method (Theorem 1.7), the energy principle (5.22) can be improved by taking into account that $\dot{\boldsymbol{\xi}}$ and $\boldsymbol{\xi}$ in equation (5.21) are not completely independent but related through additional conservation laws (invariants) inherent in the system. Among possible invariants of the hydrodynamic equations, it is natural to consider first the momentum and angular momentum or their components, which are conserved under certain symmetries of the system. The corresponding invariant for equation (5.17) is expressed in terms of the so-called *neutral displacements*:

$$\mathbf{F}[\boldsymbol{\xi}_N] = 0, \quad \frac{\partial \boldsymbol{\xi}_N}{\partial t} = 0. \tag{5.24}$$

Indeed, taking the scalar product of equation (5.17) and $\boldsymbol{\xi}_N$, integrating over the entire space and using definition (5.24) and property (5.19), we obtain a conservation law in the form $\dot{I} = 0$, where

$$I(\dot{\boldsymbol{\xi}}, \boldsymbol{\xi}) = \int \left(\rho_e \boldsymbol{\xi}_N \cdot \dot{\boldsymbol{\xi}} + 2\rho_e \boldsymbol{\xi}_N \cdot (\mathbf{V}_e \cdot \nabla)\boldsymbol{\xi} \right) d^3\mathbf{R}. \tag{5.25}$$

In a particular geometry, the general form of the neutral displacement can be derived analytically. For example, for the topology of toroidal nested magnetic surfaces, given by label $\Psi = \text{const}$ and condition $\mathbf{B}_e \cdot \nabla\Psi = 0$, which is typical for fusion plasma experiments, the neutral displacement has the form [88]

$$\boldsymbol{\xi}_N = \lambda_u(\Psi)\mathbf{u} + \lambda_v(\Psi)\mathbf{v}, \tag{5.26}$$

where $\mathbf{u} = \mathbf{B}_e/\rho_e$, $\mathbf{v} = \mathbf{D}_e/\rho_e$ and $\mathbf{D}_e$ is the divergence-free frozen-in-plasma vector which is tangential (similar to $\mathbf{B}_e$) to the same magnetic surfaces but different from $\mathbf{B}_e$:

$$\mathbf{B}_e \times \mathbf{D}_e = \rho_e \nabla\Psi.$$

Invariant (5.25), corresponding to the neutral displacement (5.26), has its nonlinear analog, the known particular case of which is the conservation of cross-helicity (at $\lambda_v = 0$ in equation (5.26)).

The inclusion of invariant (5.25) in stability analysis allows us to improve the energy principle (5.22). Following Arnold's method (Theorem 1.7), we construct a Lyapunov functional candidate near the equilibrium state $\dot{\boldsymbol{\xi}}_e = 0$, $\boldsymbol{\xi}_e = 0$

$$U(\dot{\boldsymbol{\xi}}, \boldsymbol{\xi}) = E(\dot{\boldsymbol{\xi}}, \boldsymbol{\xi}) + \lambda I(\dot{\boldsymbol{\xi}}, \boldsymbol{\xi}), \tag{5.27}$$

where coefficient λ has to be chosen to satisfy the first condition of Theorem 1.7:

$$\delta U(0,0) = \delta E(0,0) + \lambda \delta I(0,0) = 0. \tag{5.28}$$

Since $\delta E(0,0) = 0$ (E is quadratic form of $\dot{\boldsymbol{\xi}}$ and $\boldsymbol{\xi}$) and $\delta I(0,0) \equiv I(\dot{\boldsymbol{\xi}}, \boldsymbol{\xi})$ is not identically zero, then the condition (5.28) can be satisfied only by taking $\lambda = 0$. Therefore, for the equilibrium to be stable, it is sufficient to have the sign-definiteness of functional $E(\dot{\boldsymbol{\xi}}, \boldsymbol{\xi})$ on the subspace $I(\dot{\boldsymbol{\xi}}, \boldsymbol{\xi}) = 0$ (the second condition of Theorem 1.7).

The analysis of sign-definiteness of the quadratic form E with imposed linear constraint $I = 0$ is a not quite trivial task (see, for example, [117]). However, in our case the condition $I = 0$, where I is given by expression (5.25), can be resolved explicitly. Representing $\dot{\boldsymbol{\xi}}$ as

$$\dot{\boldsymbol{\xi}} = -2(\mathbf{V}_e \cdot \nabla)\boldsymbol{\xi} + \boldsymbol{\zeta}, \tag{5.29}$$

and substituting (5.29) in (5.25), one obtains a condition for the vector-function $\boldsymbol{\zeta}$

$$\int \rho_e \boldsymbol{\zeta} \cdot \boldsymbol{\xi}_N \, d^3\mathbf{R} = 0, \tag{5.30}$$

which has to be satisfied for each neutral displacement $\boldsymbol{\xi}_N$. As follows from the Fredholm theorem (Appendix B), this condition is satisfied if and only if

$$\boldsymbol{\zeta} = \frac{\mathbf{F}[\boldsymbol{\eta}]}{\rho_e}, \tag{5.31}$$

where $\boldsymbol{\eta}$ is arbitrary vector-function. Therefore, the constraint $I = 0$ yields the local relation between $\dot{\boldsymbol{\xi}}$ and $\boldsymbol{\xi}$:

$$\dot{\boldsymbol{\xi}} = -2(\mathbf{V}_e \cdot \nabla)\boldsymbol{\xi} + \frac{\mathbf{F}[\boldsymbol{\eta}]}{\rho_e}. \tag{5.32}$$

Substitution of $\dot{\boldsymbol{\xi}}$ from (5.32) into energy functional E (5.21) yields

$$E_I(\boldsymbol{\eta},\boldsymbol{\xi}) = \frac{1}{2}\int\left(\frac{1}{\rho_e}\left(\mathbf{F}[\boldsymbol{\eta}] - 2\rho_e(\mathbf{V}_e\cdot\nabla)\boldsymbol{\xi}\right)^2 - \boldsymbol{\xi}\cdot\mathbf{F}[\boldsymbol{\xi}]\right)d^3\mathbf{R}. \tag{5.33}$$

The positive definiteness of this quadratic form for all $\boldsymbol{\xi}$ and $\boldsymbol{\eta}$ is a sufficient condition for formal stability. The condition $E_I > 0$ is "softer" than the energy principle (5.22), since E_I differs from W by a nonnegative quantity. The minimization of the functional E_I over $\boldsymbol{\eta}$ in systems with nested magnetic surfaces leads to the stability condition obtained in [25] and [88]. However, the problem of sign-definiteness of the energy functional for an arbitrary equilibrium flow is not solved completely even in this (improved) condition. For this reason, additional invariants should be involved in analysis.

Recently, it was shown that the linearized system (5.17) has an infinite set of nontrivial integrals of motion [90]. Taking the n-th time derivative of equation (5.17), we express the $(n+2)$-th time derivative of $\boldsymbol{\xi}$ in terms of lower derivatives:

$$\boldsymbol{\xi}^{(n+2)} = -2(\mathbf{V}_e\cdot\nabla)\boldsymbol{\xi}^{(n+1)} + \frac{\mathbf{F}[\boldsymbol{\xi}^{(n)}]}{\rho_e}. \tag{5.34}$$

Multiplying this equation by $\rho_e\boldsymbol{\xi}^{(n+1)}$, integrating over the fluid volume and using properties (5.19), (5.20), we conclude (as in the case of energy) that the quantities

$$E_{n+1}(\dot{\boldsymbol{\xi}},\boldsymbol{\xi}) = \frac{1}{2}\int\left(\rho_e(\boldsymbol{\xi}^{(n+1)})^2 - \boldsymbol{\xi}^{(n)}\cdot\mathbf{F}[\boldsymbol{\xi}^{(n)}]\right)d^3\mathbf{R}. \tag{5.35}$$

are exact integrals of motion (E_1 corresponds to energy (5.21)). It is obvious that using recurrence relation (5.34), one can express all higher time derivatives in (5.35) in terms of $\dot{\boldsymbol{\xi}}$ and $\boldsymbol{\xi}$. In particular,

$$E_2(\dot{\boldsymbol{\xi}},\boldsymbol{\xi}) = \frac{1}{2}\int\left(\frac{1}{\rho_e}\left(\mathbf{F}[\boldsymbol{\xi}] - 2\rho_e(\mathbf{V}_e\cdot\nabla)\dot{\boldsymbol{\xi}}\right)^2 - \dot{\boldsymbol{\xi}}\cdot\mathbf{F}[\dot{\boldsymbol{\xi}}]\right)d^3\mathbf{R}. \tag{5.36}$$

For continuous media, integrals of the form (5.35) are generally independent. Moreover, all these integrals except the energy E_1 have no nonlinear analogues.

It is easy to see that integrals (5.33) and (5.36) have completely the same structure, i.e., the analysis of sign-definiteness of energy functional E with constraint $I = 0$ is equivalent to the analysis of functional E_2 without additional constraints.

Taking into account the constraint $I = 0$ in the integral E_2, we arrive at a functional which has the same structure as the integral E_3, etc. So, the set of invariants (5.35) automatically allows for all constraints, imposed on $\dot{\boldsymbol{\xi}}$ and $\boldsymbol{\xi}$ by the condition $I = 0$.

The additional integrals of motion (5.35) can be incorporated into a Lyapunov functional candidate by means of Lagrange multipliers λ_n

$$U(\dot{\boldsymbol{\xi}}, \boldsymbol{\xi}) = E(\dot{\boldsymbol{\xi}}, \boldsymbol{\xi}) + \sum_{n=2} \lambda_n E_n(\dot{\boldsymbol{\xi}}, \boldsymbol{\xi}). \tag{5.37}$$

Since all integrals E_n are quadratic forms, the first condition of Arnold's theorem (Theorem 1.7)

$$\delta U(0, 0) = 0$$

does not limit the values of λ_n. For the same reason, the conditions $\delta E_n(0, 0) = 0$ do not restrict the class of possible perturbations. Therefore, Arnold's theorem in this case is reduced to the following statement.

Theorem 5.2 *If there exist such numbers λ_n that the form (5.37) is positively (semi-) definite for all $\dot{\boldsymbol{\xi}}$ and $\boldsymbol{\xi}$, then the form (5.37) is a Lyapunov functional and the equilibrium state is formally (spectrally) stable.*

This theorem is the improved energy principle which can be used to study the formal stability of ideal MHD systems with flows.

5.3 Analytical example

For illustration of the developed method, we consider the stability of an axisymmetric equilibrium of a cold (pressure $P_e = 0$), constant-density gas rotating about the attractive center in the absence of a magnetic field. For simplicity, we assume that all equilibrium quantities depend only on the radius R in the cylindrical system of coordinates (R, φ, Z). The equilibrium velocity is then

$$\mathbf{V}_e = R\Omega(R)\mathbf{e}_\varphi, \tag{5.38}$$

where $\Omega(R)$ is the angular velocity of the rotation related to the gravitational potential $\Phi(R)$

$$R\Omega^2(R) = \frac{\partial \Phi}{\partial R}.$$

Following the standard procedure of linear stability analysis, we introduce the displacement vector $\boldsymbol{\xi}(t, \mathbf{R})$, who's dynamics is described by equation (5.17). Axial symmetry of the equilibrium allows the solution to be sought in the form of a Fourier series in the symmetry direction

$$\boldsymbol{\xi}(t, \mathbf{R}) = \sum_m \xi_m(t, \mathbf{R}),$$

where

$$\boldsymbol{\xi}_m(t, \mathbf{R}) = \Big(\xi_r(t, R, Z)\mathbf{e}_r + \xi_\varphi(t, R, Z)\mathbf{e}_\varphi + \xi_z(t, R, Z)\mathbf{e}_z\Big)e^{im(\varphi - \Omega(R)t)}. \tag{5.39}$$

Here the term with $\Omega(R)t$ in the exponent means that the perturbations are considered in the reference frame, rotating around Z-axis with angular velocity $\Omega(R)$.

Substitution of (5.39) into equation (5.17) yields the equation for the dynamics of each mode

$$\ddot{\boldsymbol{\xi}}_m + 2\Omega\hat{\mathbf{A}}\,\dot{\boldsymbol{\xi}}_m - \hat{\mathbf{B}}\,\boldsymbol{\xi}_m = 0, \tag{5.40}$$

where matrices $\hat{\mathbf{A}}$ and $\hat{\mathbf{B}}$ are defined as

$$\hat{\mathbf{A}} = \begin{pmatrix} 0 & -1 & 0 \\ 1 & 0 & 0 \\ 0 & 0 & 0 \end{pmatrix}, \quad \hat{\mathbf{B}} = \begin{pmatrix} -R\partial(\Omega^2)/\partial R & 0 & 0 \\ 0 & 0 & 0 \\ 0 & 0 & 0 \end{pmatrix}. \tag{5.41}$$

The stability condition of solutions to equation (5.40) is easily established by the spectral method. Taking $\boldsymbol{\xi}_m \sim \exp(i\omega t)$, we arrive at the dispersion relation

$$\omega^2\left(\omega^2 - 4\Omega^2 - R\frac{\partial \Omega^2}{\partial R}\right) = 0. \tag{5.42}$$

From this equation one can conclude that for the spectral stability of rotation (5.38), it is necessary and sufficient to have

$$\kappa^2 \equiv 4\Omega^2 + R\frac{\partial \Omega^2}{\partial R} > 0, \tag{5.43}$$

where κ is *epicyclic frequency*. Condition (5.43) was mentioned above as the Rayleigh stability criterion (1.1).

Now let us apply to the system (5.40) the method developed in the previous section (Theorem 5.2). It should be noted first that in this example all conservation laws are local for each azimuthal mode $\boldsymbol{\xi}_m$, i.e., instead of integrals in (5.35) one can consider the conservation of integrands; in addition, the multipliers λ_n in the Lyapunov functional candidate U (5.37) can be functions of R and Z. Omitting for simplicity the subscript m in the mode notation, we obtain the first two invariants E and E_2 in the form

$$E = \frac{1}{2}\left(\dot{\boldsymbol{\xi}}^2 - \boldsymbol{\xi}^T\hat{\mathbf{B}}\boldsymbol{\xi}\right) = \frac{1}{2}\left(\dot{\xi}_r^2 + \dot{\xi}_\varphi^2 + \dot{\xi}_z^2 + R\frac{\partial\Omega^2}{\partial R}\boldsymbol{\xi}_r^2\right), \tag{5.44}$$

$$E_2 = \frac{1}{2}\left((\hat{\mathbf{B}}\boldsymbol{\xi} - 2\Omega\hat{\mathbf{A}}\dot{\boldsymbol{\xi}})^2 - \dot{\boldsymbol{\xi}}^T\hat{\mathbf{B}}\dot{\boldsymbol{\xi}}\right) = \tag{5.45}$$

$$= \frac{1}{2}\left(\left(2\Omega\begin{pmatrix} -\dot{\xi}_\varphi \\ \dot{\xi}_r \\ 0 \end{pmatrix} + R\frac{\partial\Omega^2}{\partial R}\begin{pmatrix} \xi_r \\ 0 \\ 0 \end{pmatrix}\right)^2 + R\frac{\partial\Omega^2}{\partial R}\,\dot{\xi}_r^2\right) =$$

$$= \frac{1}{2}\left(\left(-2\Omega\dot{\xi}_\varphi + R\frac{\partial\Omega^2}{\partial R}\,\xi_r\right)^2 + \left(4\Omega^2 + R\frac{\partial\Omega^2}{\partial R}\right)\dot{\xi}_r^2\right),$$

where the superscript T denotes the transpose of the corresponding vector. According to Theorem 5.2, if any linear combination of these two functionals is positively definite for all $\dot{\boldsymbol{\xi}}$ and $\boldsymbol{\xi}$, then this combination is a Lyapunov functional and the equilibrium is stable. Choosing energy E as a Lyapunov functional candidate U ($\lambda_n \to 0$ – usual energy principle), we obtain the stability condition in the form

$$R\frac{\partial\Omega^2}{\partial R} > 0,$$

which is stiffer than the Rayleigh criterion (5.43). If we choose $U = E_2$ ($\lambda_2 \to \infty$ in (5.37)), then the positive definiteness of E_2 is guaranteed if

$$4\Omega^2 + R\frac{\partial\Omega^2}{\partial R} > 0.$$

This condition coincides exactly with the necessary and sufficient stability condition (5.43) obtained from the local dispersion law (Rayleigh criterion). That confirms the fruitfulness of the developed approach.

5.4 Conclusions

In the present chapter, the generalization of the energy principle for the study of formal stability of stationary configurations with ideal MHD flows is suggested (Theorem 5.2). The key point of the method is the inclusion into a Lyapunov functional candidate of a new set of integrals (5.35) inherent in linearized fluid dynamics. The method allows one to obtain a sufficient condition for formal stability which is closer to a necessary condition than the previously known conditions.

The method is verified for a simple analytical example; the obtained stability condition is shown to be both necessary and sufficient. We should note that the relative simplicity of the stability analysis in considered example is due to the simple form of operators of linearized dynamics (5.17); they have no differentiation and their action is reduced to multiplication by matrices (5.41). In the general case of flow with finite pressure in a magnetic field, these operators become more complex. In such a case, to find the adequate stability criterion other integrals from set (5.35) can be used.

Chapter 6

Summary

In present thesis we performed a theoretical study of MHD flows of liquid metals in annular channels for the conditions relevant to magnetorotational instability (MRI) experiments. This study includes the detailed calculations of equilibrium MHD flow in a transverse magnetic field and the analysis of its spectral stability in both ideal and dissipative MHD models.

For the study of stationary (fully-developed) configurations of Taylor-Couette and electrically driven flows, numerical code has been developed which takes into account the characteristic features of axisymmetric dissipative MHD flows in annular channels with a rectangular cross-section. The code utilizes a finite difference scheme with Jacobi iterations for solving two-dimensional elliptical equations. Using this code, the structure of equilibrium flows has been calculated for different parameters of experimental devices, including the components of the velocity and induced magnetic field. We should note that this code, after some modifications, can be used for calculations of MHD flows in straight channels.

Approximate analytical expressions have been also obtained for equilibrium profiles of angular momentum in the cases of Taylor-Couette and electrically driven flows. Thus, the dependence of flow structure on parameters of the experiment (injected current, external magnetic field, geometry, etc.) has been established, which makes it possible to optimize the experimental device for MRI investigation. It was shown that both Taylor-Couette and electrically driven flows are suitable for MRI experiments. However, different geometries of the devices have to be used: long cylinders with a narrow gap between them in the case of Taylor-Couette flow, and an annular channel with comparable height and width in the case of electrically

driven flow. The effects of inertia can also considerably change the equilibrium flow structure in both cases, so these effects have to be reduced in any MRI experiment.

From the study of equilibrium MHD flows, it follows that at large Hartmann numbers, typical for MRI experiments, the angular velocity of toroidal fluid rotation in the electrically driven flow has the form $\Omega(R) \propto 1/R^2$ almost entirely in the cross-section of the channel. It is shown that, in the frame of ideal MHD, such a rotation profile is unstable with respect to MRI, with the highest growth rate of an instability corresponding to the axisymmetric modes with azimuthal number $m = 0$. As for non-axisymmetric modes with $m \neq 0$, their instability threshold value of velocity decreases for large m as $\sim 1/m$. Consequently, in ideal MHD it is always easier to excite unstable non-axisymmetric MRI modes, though they have a lower instability growth rate. The calculation of the energy of eigen-modes in such system shows that this non-axisymmetric MRI can be explained as a coupling of originally stable positive and negative energy waves.

We have also performed a numerical study of MRI in electrically driven flow in the frame of a dissipative MHD model. It was found that the instability threshold in this case is determined by MRI of global non-axisymmetric modes with large azimuthal mode numbers m. This threshold does not depend on the type of conducting fluid as long as the magnetic Prandtl number of the fluid is small; it is determined only by the geometry of the channel. Our results are found to be in a good agreement with data from the Grenoble experiment [110], suggesting that in this experiment the non-axisymmetric MRI in electrically driven flow has been detected.

In the present thesis, a variational method for the study of formal stability of ideal MHD flows is developed, which generalizes the energy principle. The method is based on the construction of a Lyapunov functional candidate from a new set of integrals of motion (5.35) inherent in the linearized dynamics of ideal fluids. The method allows one to obtain a necessary and sufficient criterion for the stability of MHD flows; it is demonstrated by a simple analytical example. The developed method is of great potential importance in physics, since it considerably simplifies the stability study of MHD flows and reduces it to the analysis of sign-definiteness

of a quadratic functional. This circumstance makes it expedient to use this method not only in analytical studies but also in numerical schemes (similar to the energy principle).

References

[1] J. Hartmann. Hg dynamics I. Theory of the laminar flow of an electrically conductive liquid in a homogeneous magnetic field. *Det Kongelige Danske Videnskabernes Selskab. Mathematisk-Fysiske Meddelelser*, 15(6):1–28, 1937.

[2] J. Hartmann and F. Lazarius. Hg dynamics II. Experimental investigations on the flow of mercury in a homogeneous magnetic field. *Det Kongelige Danske Videnskabernes Selskab. Mathematisk-Fysiske Meddelelser*, 15(7):1–45, 1937.

[3] H. Alfven. *Cosmical electrodynamics*. Oxford: Clarendon Press, 1950.

[4] H. Alfven and C. G. Falthammar. *Cosmical electrodynamics: fundamental principles*. Oxford: Clarendon Press, second edition, 1963.

[5] T. G. Cowling. *Magnetohydrodynamics*. New York: Interscience Publishers, 1957.

[6] J. A. Shercliff. *A textbook of magnetohydrodynamics*. Oxford; New York: Pergamon Press, 1965.

[7] W. F. Hughes and F. J. Young. *The electromagnetodynamics of fluids*. New York: John Wiley & Sons, Inc., 1966.

[8] J. A. Shercliff. *The theory of electromagnetic flow-measurement*. Cambridge: University Press, 1962.

[9] F. Hofmann. *Fundamental principles of electromagnetic flow measurement*. Duisburg: KROHNE Messtechnik GmbH & Co. KG., third edition, 2003.

[10] H. Branover and Y. Unger, editors. *Metallurgical technologies, energy conversion, and magnetohydrodynamic flows*, volume 148 of *Progress in Astronautics and Aeronautics Series*. American Institute of Aeronautics and Astronautics, 1993.

[11] R. J. Rosa. *Magnetohydrodynamic energy conversion*. New York: McGraw-Hill, 1968.

[12] M. Mitchner, H. Charles, and Jr. Kruger. *Partially ionized gases*. John Wiley & Sons, Inc., 1973.

[13] S. Takezawa, H. Tamama, K. Sugawawa, H. Sakai, C. Matsuyama, H. Morita, H. Suzuki, and Y. Ueyama. Operation of the thruster for superconducting electromagnetohydrodynamic propulsion ship "YAMATO 1". *Bulletin of the Marine Engineering Society of Japan*, 23(1):46–55, 1995.

[14] L. E. Kalikhman. *Elements of magnetogasdynamics*. WB Saunders, 1967.

[15] U. Müller and L. Bühler. *Magnetofluiddynamics in channels and containers*. Berlin: Springer, 2001.

[16] S. Suckewer, H. P. Eubank, R. J. Goldston, E. Hinnov, and N. R. Sauthoff. Toroidal plasma rotation in the Princeton Large Torus induced by neutral-beam injection. *Physical Review Letters*, 43(3):207–210, 1979.

[17] N. Asakura, R. J. Fonck, K. P. Jaehnig, S. M. Kaye, B. LeBlanc, and M. Okabayashi. Toroidal rotation and ion heating during neutral beam injection in PBX-M. *Nuclear Fusion*, 33(8):1165–1184, 1993.

[18] L.-G. Eriksson, E. Righi, and K.-D. Zastrow. Toroidal rotation in ICRF-heated H-modes on JET. *Plasma Physics and Controlled Fusion*, 39(1):27–42, 1997.

[19] J. E. Rice, M. Greenwald, I. H. Hutchinson, E. S. Marmar, Y. Takase, S. M. Wolfe, and F. Bombarda. Observations of central toroidal rotation in ICRF heated Alcator C-Mod plasmas. *Nuclear Fusion*, 38(1):75–85, 1998.

[20] T. S. Taylor, E. J. Strait, L. L. Lao, M. Mauel, A. D. Turnbull, K. H. Burrell, M. S. Chu, J. R. Ferron, R. J. Groebner, R. J. La Haye, B. W. Rice, R. T. Snider, S. J. Thompson, D. Wroblewski, and D. J. Lightly. Wall stabilization of high beta plasmas in DIII-D. *Physics of Plasmas*, 2(6):2390–2396, 1995.

[21] A. M. Garofalo, A. D. Turnbull, E. J. Strait, M. E. Austin, J. Bialek, M. S. Chu, E. Fredrickson, R. J. La Haye, G. A. Navratil, L. L. Lao, E. A. Lazarus, M. Okabayashi, B. W. Rice, S. A. Sabbagh, J. T. Scoville, T. S. Taylor, and M. L. Walker. Stabilization of the external kink and control of the resistive wall mode in tokamaks. *Physics of Plasmas*, 6(5):1893–1898, 1999.

[22] M. Takechi, G. Matsunaga, N. Aiba, T. Fujita, T. Ozeki, Y. Koide, Y. Sakamoto, G. Kurita, A. Isayama, and Y. Kamada. Identification of a low plasma-rotation threshold for stabilization of the resistive-wall mode. *Physical Review Letters*, 98(5):055002, 2007.

[23] E. Frieman and M. Rotenberg. On hydromagnetic stability of stationary equilibria. *Review of Modern Physics*, 32(4):898–902, 1960.

[24] I. B. Bernstein, E. A. Frieman, M. D. Kruskal, and R. M. Kulsrud. An energy principle for hydromagnetic stability problems. *Proceedings of the Royal Society of London. Series A, Mathematical and Physical Sciences*, 244(1236):17–40, 1958.

[25] E. Hameiri. Variational principles for equilibrium states with plasma flow. *Physics of Plasmas*, 5(9):3270–3281, 1998.

[26] D. D. Holm, J. E. Marsden, T. Ratiu, and A. Weinstein. Nonlinear stability of fluid and plasma equilibria. *Physics Reports (Review Section of Physics Letters)*, 123(1,2):1–116, 1985.

[27] J. Frank, A. King, and D. Raine. *Accretion power in astrophysics*. Cambridge University Press, Cambridge, third edition, 2002.

[28] N. I. Shakura and R. A. Sunyaev. Black holes in binary systems. Observational appearance. *Astronomy and Astrophysics*, 24:337–355, 1973.

[29] L. Rayleigh. On the dynamics of revolving fluids. *Proceedings of the Royal Society of London. Series A, Mathematical and Physical Sciences*, 93(648):148–154, 1917.

[30] S. A. Balbus. Spinning discs in the lab. *Nature*, 444:281–283, 2006.

[31] Nonlinear stability, hydrodynamical turbulence, and transport in disks. *Astrophysical Journal*, 467:76–86, 1996.

[32] J. F. Hawley, S. A. Balbus, and W. F. Winters. Local hydrodynamic stability of accretion disks. *Astrophysical Journal*, 518(1):394–404, 1999.

[33] H. Ji, M. Burin, E. Schartman, and J. Goodman. Hydrodynamic turbulence cannot transport angular momentum effectively in astrophysical disks. *Nature*, 444:343–346, 2006.

[34] S. A. Balbus and J. F. Hawley. A powerful local shear instability in weakly magnetized disks. I. Linear analysis. *Astrophysical Journal*, 376:214–222, 1991.

[35] E. P. Velikhov. Stability of an ideally conducting liquid flowing between cylinders rotating in a magnetic field. *Soviet Physics – Journal of Experimental and Theoretical Physics*, 9:995–998, 1959.

[36] S. Chandrasekhar. The stability of non-dissipative Couette flow in hydromagnetics. *Proceedings of the National Academy of Sciences of the USA*, 46(2):253–257, 1960.

[37] G. Rüdiger and R. Hollerbach. *The magnetic universe. Geophysical and astrophysical dynamo theory*. Weinheim: Wiley-VCH, 2004.

[38] S. A. Balbus and J. F. Hawley. Instability, turbulence, and enhanced transport in accretion disks. *Review of Modern Physics*, 70(1):1–53, 1998.

[39] S. A. Balbus. Enhanced angular momentum transport in accretion disks. *Annual Review of Astronomy and Astrophysics*, 41:555–597, 2003.

[40] J. F. Hawley and J. M. Stone. Nonlinear evolution of the magnetorotational instability in ion-neutral disks. *Astrophysical Journal*, 501:758–771, 1998.

[41] T. P. Fleming, J. M. Stone, and J. F. Hawley. The effect of resistivity on the nonlinear stage of the magnetorotational instability in accretion disks. *Astrophysical Journal*, 530:464–477, 2000.

[42] R. Arlt and G. Rudiger. Global accretion disk simulations of magnetorotational instability. *Astronomy and Astrophysics*, 374:1035–1048, 2001.

[43] P. C. Fragile, O. M. Blaes, P. Anninos, and J. D. Salmonson. Nonlinear evolution of the magnetorotational instability in ion-neutral disks. *Astrophysical Journal*, 668:417–429, 2007.

[44] D. R. Sisan, N. Mujica, W. A. Tillotson, Y.-M. Huang, W. Dorland, A. B. Hassam, T. M. Antonsen, and D. P. Lathrop. Experimental observation and characterization of the magnetorotational instability. *Physical Review Letters*, 93(11):114502, 2004.

[45] K. Noguchi, V. I. Pariev, S. A. Colgate, H. F. Beckley, and J. Nordhaus. Magnetorotational instability in liquid metal Couette flow. *Astrophysical Journal*, 575:1151–1162, 2002.

[46] H. Ji, J. Goodman, A. Kageyama, M. Burin, E. Schartman, and W. Liu. Magnetorotational instability in a short Couette flow of liquid gallium. *AIP Conference Proceedings*, 733:21–34, 2004.

[47] F. Stefani, T. Gundrum, G. Gerbeth, G. Rüdiger, M. Schultz, J. Szklarski, and R. Hollerbach. Experimental evidence for magnetorotational instability in a Taylor-Couette flow under the influence of a helical magnetic field. *Physical Review Letters*, 97(18):184502, 2006.

[48] K. Noguchi and V. Pariev. Magnetorotational instability in a Couette flow of plasma. *AIP Conference Proceedings*, 692:285–292, 2003.

[49] E. P. Velikhov, A. A. Ivanov, S. V. Zakharov, V. S. Zakharov, A. O. Livadny, and K. S. Serebrennikov. Equilibrium of current driven rotating liquid metal. *Physics Letters A*, 358(3):216–221, 2006.

[50] H. Ji, J. Goodman, and A. Kageyama. Magnetorotational instability in a rotating liquid metal annulus. *Monthly Notices of the Royal Astronomical Society*, 325(2):L1–L5, 2001.

[51] J. Goodman and H. Ji. Magnetorotational instability of dissipative Couette flow. *Journal of Fluid Mechanics*, 462:365–382, 2002.

[52] A. Kageyama, H. Ji, J. Goodman, F. Chen, and E. Shoshan. Numerical and experimental investigation of circulation in short cylinders. *Journal of the Physical Society of Japan*, 73(9):2424–2437, 2004.

[53] G. Rüdiger and Y. Zhang. MHD instability in differentially-rotating cylindric flows. *Asronomy and Astrophysics*, 378:302–308, 2001.

[54] D. Shalybkov, G. Rüdiger, and M. Schultz. Nonaxisymmetric patterns in the linear theory of MHD Taylor-Couette instability. *Astronomy and Astrophysics*, 395:339–343, 2002.

[55] G. Rüdiger, M. Schultz, and D. Shalybkov. Linear magnetohydrodynamic Taylor-Couette instability for liquid sodium. *Physical Review E*, 67:046312, 2003.

[56] G. Rüdiger, R. Hollerbach, M. Schultz, and D. Shalybkov. The stability of MHD Taylor-Couette flow with current-free spiral magnetic fields between conducting cylinders. *Astronomische Nachrichten*, 326(6):409–413, 2005.

[57] R. Hollerbach and G. Rüdiger. New type of magnetorotational instability in cylindrical Taylor-Couette flow. *Physical Review Letters*, 95(12):124501, 2005.

[58] W. Liu, J. Goodman, and H. Ji. Traveling waves in a magnetized Taylor-Couette flow. *Physical Review E*, 76:016310, 2007.

[59] J. A. Baylis and J. C. R. Hunt. MHD flow in an annular channel: theory and experiment. *Journal of Fluid Mechanics*, 48:423–428, 1971.

[60] R. M. Kulsrud. *MHD description of plasma*, volume 1 of *Basic plasma physics*, pages 115–145. Amsterdam: North-Holland, 1983.

[61] S. I. Braginskii. Magnetohydrodynamics of weakly conducting liquids. *Soviet Physics – Journal of Experimental and Theoretical Physics*, 10:1005–1014, 1960.

[62] J. C. R. Hunt. Magnetohydrodynamic flow in rectangular ducts. *Journal of Fluid Mechanics*, 21:577–590, 1965.

[63] J. C. R. Hunt and K. Stewartson. Magnetohydrodynamic flow in a rectangular duct. II. *Journal of Fluid Mechanics*, 23:563–581, 1965.

[64] T. Z. Fahidy. On magnetohydrodynamic flow in rectangular ducts: an extension of the Hunt-Stewartson approach. *Journal of Fluid Mechanics*, 42:245–248, 1970.

[65] A. Pothérat, J. Sommeria, and R. Moreau. An effective two-dimensional model for MHD flows with transverse magnetic feld. *Journal of Fluid Mechanics*, 424:75–100, 2000.

[66] Verardi S. L. L., Cardoso J. R., and Motta C. C. A solution of two-dimensional magnetohydrodynamic flow using the finite element method. *Transactions on Magnetics*, 34(5):3134–3137, 1998.

[67] M. Hughes, K. A. Pericleous, and M. Cross. The numerical modelling of DC electromagnetic pump and brake flow. *Applied Mathematical Modelling*, 19(12):713–723, 1995.

[68] L. Leboucher. Monotone scheme and boundary conditions for finite volume simulation of magnetohydrodynamic internal flows at high Hartmann number. *Journal of Computational Physics*, 150(1):181–198, 1999.

[69] M. Tezer-Sezgin. Solution of magnetohydrodynamic flow in a rectangular duct by differential quadrature method. *Computers and Fluids*, 33(4):533–547, 2004.

[70] I. V. Khalzov and A. I. Smolyakov. On the calculation of steady-state magnetohydrodynamic flows of liquid metals in circular ducts of a rectangular cross section. *Technical Physics*, 51(1):26–33, 2006.

[71] W. H. Press, B. P. Flannery, S. A. Teukolsky, and W. Vettering. *Numerical recipes in C: the art of scientific computing*. Cambrige Univ. Press, Cambridge, second edition, 1992.

[72] A. M. Lyapunov. *General problem of the stability of motion*. Taylor & Francis Books Ltd, 1992.

[73] J. M. Ball and J. E. Marsden. Quasiconvexity at the boundary, positivity of the second variation and elastic stability. *Archive for Rational Mechanics and Analysis*, 86:251–277, 1984.

[74] A. B. Mikhailovskii. *Electromagnetic instabilities in an inhomogeneous plasma*. Taylor & Francis, 1992.

[75] A. B. Mikhailovskii. *Instabilities in a confined plasma*. Taylor & Francis, 1998.

[76] G. Bateman. *MHD instabilities*. Cambridge, Mass.: MIT Press, 1978.

[77] B. B. Kadomtsev. *Hydromagnetic stability of a plasma*, volume 2 of *Reviews of plasma physics*, pages 153–199. New York, Consultants Bureau, 196.

[78] G. Laval, C. Mercier, and R. Pellat. Necessity of the energy principles for magnetostatic stability. *Nuclear Fusion*, 5(2):156–158, 1965.

[79] K. I. Ilin and V. A. Vladimirov. Energy principle for magnetohydrodynamic flows and Bogoyavlenskij's transformation. *Physics of Plasmas*, 11(7):3586–3594, 2004.

[80] V. I. Arnold. Conditions for nonlinear stability of stationary plane curvilinear flows of an ideal fluid. *Doklady Mathematics*, 6:773–776, 1965.

[81] V. I. Arnold. Variational principle for three-dimensional steady-state flows of an ideal fluid. *Journal of Applied Mathematics and Mechanics*, 29(5):1002–1008, 1965.

[82] V. I. Arnold. On an a priori estimate in the theory of hydrodynamical stability. *American Mathematical Society Translations: Series 2*, 79:267–269, 1969.

[83] H. C. Corben and P. Stehle. *Classical mechanics*. Courier Dover Publications, second edition, 1994.

[84] P. J. Morrison and J. M. Greene. Noncanonical Hamiltonian density formulation of hydrodynamics and ideal magnetohydrodynamics. *Physical Review Letters*, 45(10):790–794, 1980.

[85] P. J. Morrison and S. Eliezer. Spontaneous symmetry breaking and neutral stability in the noncanonical Hamiltonian formalism. *Physical Review A*, 33(6):4205–4214, 1986.

[86] J. M. Finn and G.-Z. Sun. Nonlinear stability and the energy-Casimir method. *Comments on Plasma Physics and Controlled Fusion*, 11(2):7–25, 1987.

[87] V. A. Vladimirov, H. K. Moffatt, and K. I. Ilin. On general transformations and variational principles for the magnetohydrodynamics of ideal fluids. Part 2. Stability criteria, for two-dimensional flows. *Journal of fluid mechanics*, 329:187–205, 1996.

[88] V. I. Ilgisonis and V. P. Pastukhov. MHD stability of steady-state flows in a toroidal magnetized plasma. *Plasma Physics Reports*, 22(3):208–218, 1996.

[89] E. Hameiri. Dynamically accessible perturbations and magnetohydrodynamic stability. *Physics of Plasmas*, 10(7):2643–2648, 2003.

[90] V. I. Ilgisonis and I. V. Khalzov. Formal stability of three-dimensional flows of an ideal conducting fluid. *JETP Letters*, 82(9):570–574, 2005.

[91] L. D. Landau E. M. Lifshitz. *Fluid mechanics*. Butterworth-Heinemann, second edition, 1987.

[92] J. K. Kevorkian and J. D. Cole. *Multiple scale and singular perturbation methods*, volume 114 of *Applied Mathematical Sciences*. Springer, first edition, 1996.

[93] Flow regimes in a circular Couette system with independently rotating cylinders. *Journal of Fluid Mechanics*, 164:155–183, 1986.

[94] R. Hollerbach and A. Fournier. End-effects in rapidly rotating cylindrical Taylor-Couette flow. *AIP Conference Proceedings*, 733:114–121, 2004.

[95] J. Szklarski and G. Rüdiger. The Ekman-Hartmann layer in MHD Taylor-Couette flow. *arXiv:0710.5600*, 2007.

[96] S. A. Balbus and J. F. Hawley. A powerful local shear instability in weakly magnetized disks. IV. Nonaxisymmetric perturbations. *Astrophysical Journal*, 400:610–621, 1992.

[97] R. Matsumoto and T. Tajima. Magnetic viscosity by localized shear flow instability in magnetized accretion disks. *Astrophysical Journal*, 445:767–779, 1995.

[98] W.-T. Kim and E. C. Ostriker. Magnetohydrodynamic instabilities in shearing, rotating, stratified winds and disks. *Astrophysical Journal*, 540:372–403, 2000.

[99] K. Noguchi, T. Tajima, and R. Matsumoto. Robustly unstable eigenmodes of the magnetoshearing instability in accretion disks. *Astrophysical Journal*, 541:802–810, 2000.

[100] C. Curry, R. E. Pudritz, and P. G. Sutherland. On the global stability of magnetized accretion disks – I. Axisymmetric modes. *Astrophysical Journal*, 434:206–220, 1994.

[101] C. Curry and R. E. Pudritz. On the global stability of magnetized accretion disks – II. Vertical and azimuthal magnetic fields. *Astrophysical Journal*, 453:697–714, 1995.

[102] C. Curry and R. E. Pudritz. On the global stability of magnetized accretion disks – III. Non-axisymmetric modes. *Monthly Notices of the Royal Astronomical Society*, 281(1):119–136, 1996.

[103] I. V. Khalzov, V. I. Ilgisonis, A. I. Smolyakov, and E. P. Velikhov. Magnetorotational instability in electrically driven flow of liquid metal: spectral analysis of global modes. *Physics of Fluids*, 18(12):124107, 2006.

[104] G. I. Ogilvie and J. E. Pringle. The non-axisymmetric instability of a cylindrical shear flow containing an azimuthal magnetic field. *Monthly Notices of the Royal Astronomical Society*, 279:152–164, 1996.

[105] R. Keppens, F. Casse, and J. P. Goedbloed. Waves and instabilities in accretion disks: magnetohydrodynamic spectroscopic analysis. *Astrophysical Journal*, 569:L121–L126, 2002.

[106] A. L. Fabrikant and Yu. A. Stepanyants. *Propagation of waves in shear flows*, volume 18 of *Nonlinear science, Series A*. World Scientific, 1998.

[107] I. V. Khalzov, A. I. Smolyakov, and V. I. Ilgisonis. Energy of eigen-modes in magnetohydrodynamic flows of ideal fluids. *arXiv:0712.1839, submitted to Physics of Plasmas*, 2007.

[108] C. N. Lashmore-Davies. Negative energy waves. *Journal of Plasma Physics*, 71:101–109, 2005.

[109] I. V. Khalzov, A. I. Smolyakov, and V. I. Ilgisonis. Magnetorotational instability in electrically driven fluids. *arXiv:0711.2818, submitted to Physical Review Letters*, 2007.

[110] P. Moresco and T. Alboussière. Experimental study of the instability of the Hartmann layer. *Journal of Fluid Mechanics*, 504:167–181, 2004.

[111] E. Knobloch. On the stability of magnetized accretion discs. *Monthly Notices of the Royal Astronomical Society*, 255:25–28, 1992.

[112] R. C. Lock. The stability of the flow of an electrically conducting fluid between parallel planes under a transverse magnetic field. *Proceedings of the Royal Society of London. Series A, Mathematical and Physical Sciences*, 233(1192):105–125, 1955.

[113] D. S. Krasnov, E. A. Zienicke, O. Zikanov, T. Boeck, and A. Thess. Numerical study of the instability of the Hartmann layer. *Journal of Fluid Mechanics*, 504:183–211, 2004.

[114] E. A. Zienicke and D. S. Krasnov. Parametric study of streak breakdown mechanism in Hartmann flow. *Physics of Fluids*, 17:114101, 2005.

[115] I. Herron and J. Goodman. The small magnetic Prandtl number approximation suppresses magnetorotational instability. *Zeitschrift für angewandte Mathematik und Physik*, 57:615–622, 2006.

[116] B. Coppi and P. S. Coppi. Importance of finite thermal energy density and singular modes for the transport of angular momentum in accretion disks. *Annals of Physics*, 291(1):134–165, 2001.

[117] T. L. Vincent and E. M. Cliff. Maximum-minimum sufficiency and lagrange multipliers. *AIAA Journal*, 8:171–173, 1970.

[118] R. Ansorge. *Mathematical models of fluiddynamics: modelling, theory, basic numerical facts. – An introduction.* Wiley-VCH, 2006.

[119] V. S. Vladimirov. *Equations of mathematical physics.* Nonlinear science, Series A. Mir, 1984.

Appendix A

Stability of the numerical scheme

Consider the stability of the finite-difference scheme (2.30) for simplified system (2.44), (2.45), describing the flow faraway from the side walls of the channel. We have

$$\frac{u_j^{n+1}-u_j^n}{\tau} = \frac{u_{j+1}^n+u_{j-1}^n-2u_j^{n+1}}{s^2}+\mathrm{Ha}\frac{h_{j+1}^n-h_{j-1}^n}{2s}, \tag{A.1}$$

$$\frac{h_j^{n+1}-u_j^n}{\tau} = \frac{h_{j+1}^n+h_{j-1}^n-2h_j^{n+1}}{s^2}+\mathrm{Ha}\frac{u_{j+1}^n-u_{j-1}^n}{2s}, \tag{A.2}$$

where τ is a time step and s is a grid spacing in the z direction. We look for a solution to this system in the form

$$u_j^n = q^n u_0 \mathrm{e}^{ikz_j}, \tag{A.3}$$

$$h_j^n = q^n h_0 \mathrm{e}^{ikz_j}, \tag{A.4}$$

where i is the imaginary unit, u_0 and h_0 are amplitude factors. Substituting these expressions into (A.1), (A.2) we arrive at

$$\begin{pmatrix} \dfrac{1-q}{\tau}+\dfrac{2(\cos\zeta-q)}{s^2} & i\mathrm{Ha}\dfrac{\sin\zeta}{s} \\ i\mathrm{Ha}\dfrac{\sin\zeta}{s} & \dfrac{1-q}{\tau}+\dfrac{2(\cos\zeta-q)}{s^2} \end{pmatrix} \begin{pmatrix} u_0 \\ h_0 \end{pmatrix} = \begin{pmatrix} 0 \\ 0 \end{pmatrix}, \tag{A.5}$$

where $\zeta = ks$ for brevity. For this system to have nontrivial solution, its determinant must vanish, i. e.,

$$\left(\frac{1-q}{\tau}+\frac{2(\cos\zeta-q)}{s^2}\right)^2+\mathrm{Ha}^2\frac{\sin^2\zeta}{s^2}=0. \tag{A.6}$$

This equation should be considered as the equation for the parameter q. According to the von Neumann criterion (see, for example, [118]), the finite difference scheme is stable if

$$\max_{\zeta,\ \tau,\ s} |\, q(\zeta,\ \tau,\ s)\,| \le 1+O(\tau). \tag{A.7}$$

Let us verify this condition in our case. Equation (A.6) yields:

$$q=\frac{\dfrac{1}{\tau}+\dfrac{2\cos\zeta}{s^2}\pm i\mathrm{Ha}\dfrac{\sin\zeta}{s}}{\dfrac{1}{\tau}+\dfrac{2}{s^2}}. \tag{A.8}$$

The von Neumann criterion (A.7) is satisfied if $|\,q|^2\le 1$, i. e.,

$$\left(\frac{1}{\tau}+\frac{2\cos\zeta}{s^2}\right)^2+\mathrm{Ha}^2\frac{(1-\cos^2\zeta)}{s^2}\le\left(\frac{1}{\tau}+\frac{2}{s^2}\right)^2. \tag{A.9}$$

The terms in this inequality can be regrouped to give

$$(1-\cos\zeta)\left[\frac{4}{\tau}+\frac{4}{s^2}(1+\cos\zeta)-\mathrm{Ha}^2(1+\cos\zeta)\right]\geq 0. \tag{A.10}$$

It is easy to see that (A.10) is satisfied if

$$\frac{2}{\tau}+\frac{4}{s^2}\geq \mathrm{Ha}^2. \tag{A.11}$$

This is the stability condition of numerical scheme (A.1), (A.2).

Appendix B

Fredholm theorem for Hermitian operators

Let L be a linear operator acting on Hilbert space $\mathcal{H}$ – a complete normed space under the norm defined by a scalar product $(\cdot, \cdot)$. We use the following definitions and theorems known from functional analysis [119].

Definition B.1 (Kernel of linear operator) *The kernel of a linear operator L is the set of all elements u such that*

$$Lu = 0.$$

The kernel forms a subspace in $\mathcal{H}$; it is denoted as $\ker L$.

Definition B.2 (Hermitian operator) *Linear operator L: $\mathcal{H} \to \mathcal{H}$ is called a Hermitian (self-adjoint) operator if for any u and v from $\mathcal{H}$*

$$(v,\ Lu) = (u,\ Lv).$$

For Hermitian operators the following theorems hold.

Theorem B.3 *If the linear operator L is Hermitian, then all its eigen-values $\{\lambda_i\}$ are real and its eigen-functions, corresponding to different eigen-values, are orthogonal.*

Theorem B.4 *If a set of eigen-functions $\{u_i\}$ of a Hermitian operator L is countable, then it can be represented as orthonormal:*

$$(Lu_i, u_j) = \lambda_i (u_i, u_j) = \lambda_i \delta_{ij},$$

where δ_{ij} is the Kronecker delta.

Now we are able to prove the Fredholm theorem for Hermitian operators.

Theorem B.5 (Fredholm) *The equation*

$$Lu = f, \quad f \in \mathcal{H}, \tag{B.1}$$

where L is a Hermitian operator, can be solved for u if and only if the function f is orthogonal to the kernel of the operator L (in other words, if for all v : $v \in \ker L \longrightarrow (f, v) = 0$).

Proof *Necessity.* If equation (B.1) has a solution u, and $v \in \ker L$ (i.e., $Lv = 0$), then

$$(f,\ v) = (Lu,\ v) = (u,\ Lv) = 0,$$

and necessity is proved.

Sufficiency. Suppose $(f, v) = 0$ for all $v \in \ker L$. According to Theorem B.4, we can introduce in the space $\mathcal{H}$ orthonormal basis $\{u_k, v_l\}$, where $\{u_k\}$ are the eigen-functions corresponding to non-zero eigen-values $\lambda_k \neq 0$ and $\{v_l\}$ are eigen-functions with zero eigen-values, i.e., $Lv_l = 0$. It is obvious, that the kernel of operator L is a linear span of eigen-functions $\{v_l\}$, i. e., any element $v \in \ker L$ can be represented as a linear combination of $\{v_l\}$. Therefore, in order to satisfy the condition $(f,\ v) = 0$ for all $v \in \ker L$, the function f must have the following form:

$$f = \sum_k \gamma_k u_k. \tag{B.2}$$

The unknown function u is represented in general as

$$u = \sum_k \alpha_k u_k + \sum_l \beta_l v_l. \tag{B.3}$$

Substitution of expressions (B.2) and (B.3) into equation (B.1) yields

$$\sum_k \alpha_k \lambda_k u_k = \sum_k \gamma_k u_k.$$

Since the eigen-functions $\{u_k\}$ are orthogonal (Theorem B.3), we have

$$\alpha_k = \frac{\gamma_k}{\lambda_k}. \tag{B.4}$$

Taking in (B.3) coefficients α_k given by (B.4) and arbitrary β_l, we find the solution to problem (B.1). So, the sufficiency has been proved.

In the case considered in Chapter 5, the operator

$$\mathbf{L}[\boldsymbol{\xi}] = \frac{\mathbf{F}[\boldsymbol{\xi}]}{\rho_e} \tag{B.5}$$

is Hermitian (self-adjoint) in terms of scalar product

$$(\boldsymbol{\xi},\ \boldsymbol{\eta}) = \int \rho_e \boldsymbol{\xi} \cdot \boldsymbol{\eta}\, d^3\mathbf{R};$$

it follows immediately from property (5.19). The neutral displacements $\boldsymbol{\xi}_N$ (5.24) are nothing else but the kernel of operator $\mathbf{L}$ (B.5). Applying the Fredholm theorem to operator $\mathbf{L}$, we obtain equation (5.31).